Local Modifications of Interfaces and Electronic Properties on the Molecular Scale with Scanning Probe Microscopy

By
© 2021
Jennifer L. Doolin

B.S., University of Kansas, 2014

Submitted to the graduate degree program in Chemistry and the Graduate Faculty of the University of Kansas in partial fulfillment of the requirements for the degree of Doctor of Philosophy.

Chair: Cindy L. Berrie

Christopher G. Elles

Marco Caricato

Timothy A. Jackson

Susan M. Stagg-Williams

Date Defended: 11 December 2020

The dissertation committee for Jennifer L. Doolin certifies that this is the approved version of the following dissertation:

Local Modifications of Surfaces and Electronic Properties at the Molecular Scale with Scanning Probe Microscopy

Chair: Cindy L. Berrie

Date Approved: 7 February 2021

Abstract

The nanoscience field is shifting focus from characterizing and synthesizing novel nanomaterials, to incorporating nanomaterials into functional devices for photovoltaic, energy, and sensing applications. Furthermore, developing greener materials could reduce the use of expensive, toxic metals in many of these applications while potentially increasing their efficiency. Developing greener fabrication methods could reduce manufacturing costs, save time, and limit resource use. Nanoscale understanding, and control, of how materials interact is critical to rapidly engineer new devices. The research presented in this dissertation is dedicated to measuring local changes in electronic properties and fabricating nanoscale structures using scanning probe microscopy techniques.

The first two chapters provide introductory information relevant for this dissertation. Chapter 1 includes pertinent information about the nanoscience field, as well as materials and applications that are related to research in this dissertation. Chapter 1 discusses graphene's unique properties and its potential use in a wide variety of applications. Graphene's electronic properties are typically modified through doping to tailor it to a specific application. Current literature demonstrates extensive examples of this doping phenomenon, but most are bulk measurements. This dissertation aims to locally map how dopants affect graphene's electronic properties at the molecular scale. To do this, we use atomic force microscopy (AFM) techniques due to their versatility and ability to probe features on the nanoscale. Chapter 2 presents the theory and implementation of AFM-based techniques to map local surface topography. Kelvin probe force microscopy (KPFM) is used to spatially map local surface potential changes on samples.

In Chapters 3 and 4, we proposed using azulene as a novel, tunable dopant for graphene. Azulene is a planar, conjugated ring system with complementary frontier molecular orbital density. Therefore, the energy of either azulene's highest occupied molecular orbital or lowest unoccupied

molecular orbital can be selectively tuned based on the location and type of substituent placed around the azulene backbone. This provides a framework for which to study how manipulating a physisorbed dopant's energy level alignment with the substrate's Fermi level affects local surface potential. In our experiments, we used highly ordered pyrolytic graphite (HOPG) as a model for how these molecules would interact with graphene. HOPG and graphene have similar chemical and electronic properties, but graphite substrates are more consistent and reproducible. Using graphite substrates allowed for reliable comparisons of molecules' behavior across multiple samples.

The beginning of Chapter 3 focuses on optimizing deposition techniques for azulene-based molecules on graphite. Vapor deposition proved to be the simplest and cleanest deposition method. This technique was subsequently applied to other substituted azulenes in Chapter 4. Noncontact atomic force microscopy (NCAFM) and Kelvin probe microscopy (KPFM) were conducted simultaneously on samples to obtain local maps of topography and surface potential. The remainder of Chapter 3 focuses on analysis for azulene and naphthalene on graphite, while Chapter 4 expands these techniques to other substituted azulenes. We were able to identify single molecules adsorbed to graphite's terraces using topographical cross-sections, as well as resolve changes in the relative local contact potential differences with KPFM when different molecules were adsorbed on graphite. These distinct differences suggest that there is a critical relationship between the dopant's molecular structure and the doping effect. However, this relationship is not straightforward. We found this doping effect to be localized to where the dopant is adsorbed on the substrate.

While Chapters 3 and 4 center around probing the arrangement and properties of dopants on the molecular scale, Chapter 5 focuses on growing metal nanostructures with a defined size, shape, and orientation on a surface. Chapter 5 aims to develop a novel resist layer to increase the versatility of bottom-up metal nanostructure growth. Having control over the size, shape, and placement of metallic nanostructures on surfaces is integral for plasmonic sensors. Typical organic

resist layers used in bottom-up metal nanostructure fabrication can only be used on certain substrates, require harsh reagents to remove from the surface, and cannot withstand the high temperatures required for certain metal deposition techniques. A thin layer of sodium chloride (NaCl) could behave as a versatile, robust resist layer that can withstand the high temperatures required for thermal evaporation or atomic layer deposition (ALD). Such a resist layer could easily be removed using water, instead of harsh reagents. We demonstrated that small NaCl nanoparticles could be manipulated with scanning probe lithography on a Si(111) surface to create recognizable patterns that could withstand gold-coating via thermal evaporation. Any NaCl nanoparticles not completely encased in gold were able to be removed, leaving a recognizable imprint in the deposited gold metal. A method for depositing a uniform NaCl layer needs to be pursued, but this proof of concept experiment has demonstrated its use as a versatile resist layer for bottom-up metal nanostructure fabrication.

Chapter 6 summarizes key conclusions from this research and proposes future directions to expand what we've learned. Locally probing and controlling nanoscale interactions is crucial to understanding how heterostructures behave as nanomaterials are incorporated into more complicated devices. Increasing the flexibility of fabrication methods is important for scaling up nanodevice manufacturing. The research in this dissertation advances knowledge required for using nanomaterials for practical applications.

Acknowledgements

First, I want to thank my advisor, Dr. Cindy Berrie, for her invaluable support and expertise. From my first undergraduate honors general chemistry course to my final doctoral dissertation, thank you for pushing me to be inquisitive and challenge my knowledge. I truly appreciate your dedication to your students, both in research and in the classroom. Thank you for taking the time to answer all my questions, no matter how silly or small. Your unwavering support and understanding reassured me that I could face any challenge that research, or life, presented. I truly enjoyed working with you as a graduate research and teaching assistant and am honored to have been one of your students.

Thank you to my fellow Berrie group members for being fantastic colleagues! To Dr. Monisola Okeowo, Dr. Sasanka Ulapane, and Dr. Nilan Kamathewatta, thank you for your knowledge and friendship. You all made working in the lab fun! I will fondly remember our coffee/hot chocolate sessions where we would ponder questions related to research, classes, and life. Many thanks to our current graduate students: Yasmine Farhat, Xavier Ortiz, and Wadha Alqahtani. I also appreciate our many undergraduate and REU students. Thank you for being great colleagues, asking questions, and listening to my "work in progress" practice talks. I had so much fun working with you all, and I look forward to following your future accomplishments!

I have had the pleasure of working with many Department of Chemistry faculty members throughout my undergraduate and graduate careers. Thank you for being excellent teachers and mentors – I have learned so much from you! Thank you to my committee members, Dr. Christopher Elles, Dr. Marco Caricato, Dr. Tim Jackson, and Dr. Susan Stagg-Williams. I truly appreciate your time and feedback.

This research would not have been possible if not for the support from our collaborators. Thank you to Dr. Misha Barybin and his research group for supplying the azulene molecules used in

my work. Many thanks to Dr. Travis Witte for allowing us to use some of the teaching lab's instrumentation. Thank you to Dr. Judy Wu, in the Department of Physics and Astronomy, for your expertise and collaboration. Thank you to Alan Hase, of the Physics Machine Shop, for manufacturing support pieces for our UHV SPM instrument. Your assistance with moving the UHV SPM instrument and the attached deposition chambers from Malott to ISB was invaluable. Thank you to Jeff Worth for repairing wires on our UHV SPM scan head.

I am fortunate to have a strong support network outside of the University of Kansas as well. To my parents, Rich and Laura Totleben, thank you for your endless love and support. Thank you for raising me to be curious and encouraging me to chase my dreams. Graduate school was difficult at times, and your support made it easier. To my brother, Richard Totleben, I am grateful for your words of encouragement! I enjoyed spending time at KU with you, especially for our weekly lunches. Thank you for your support! I love you all.

To Emily, Alec, Kristin, Blaine, Annessa, Logan, Brad, and Emma, thank you for your friendship! I look forward to the time when we can gather to watch sporting events and play board games in person again. Thank you to my in-laws, John and Diane Doolin, for your support! Your care packages and emergency dinners were life savers.

Finally, I want to thank my loving husband, Neal Doolin. The hardest things are worth doing when you have the right person by your side - thank you for being my right person. I am incredibly grateful for your love, support, and friendship. Thank you for always believing in me. I look forward to our future adventures together. My love to you, always.

Table of Contents

Chapter 1: Introduction

1.1 Nanoscience Background & Motivation

Nanoscience, a relatively new field of research, has developed rapidly within the last few decades. Until the 1930s, it was impossible to see nanoscale features because optical microscopes were the best tools for magnifying surfaces. Then, electron microscopies such as transmission electron microscopy (TEM)[1] and scanning electron microscopy (SEM)[2] were designed to image surfaces using high-energy electrons. Such techniques could theoretically identify features on the angstrom scale, surpassing the resolution of traditional optical microscopes.[2] Richard Feynman delivered a lecture titled "There's Plenty of Room at the Bottom" on December 29, 1959 at the annual American Physical Society meeting.[3, 4] This address is considered to be the first nanotechnology lecture, although Feynman never used that phrase directly. In his speech, Feynman hypothesized about the uses of miniaturized devices, and even offered $1000 to whomever could miniaturize a single book page to be 1/25,000 of its original size.[4] Still, nanoscience would not become a popular research field until the 1980s. Not only were electron microscopes commercially available, but new scanning probe microscopies[5, 6] were also developed and capable of atomic resolution. Once imaging techniques were in place to observe nanomaterials, the focus shifted towards characterizing and optimizing the growth of isolated nanomaterials.

Much of the nanoscience research between the 1980s and early 2010s was devoted to identifying nanomaterials, characterizing their unique properties, and optimizing their growth. Nanomaterials are fascinating because their properties change at small dimensions compared to their bulk analogs. Metal nanoparticles can absorb different wavelengths of light depending on their size and shape.[7-9] Metal nanoparticles had been unknowingly used by humans for hundreds of years to give vibrant colors in ceramics and stained glass windows.[3] Gold[10] and silver[11] can have antimicrobial properties on the nanoscale. Changes in a material's nanoscale structure can result in different

reactivity and catalytic-activity.[12-14] New carbon allotropes such as fullerenes (also known as buckyballs)[15], carbon nanotubes (CNTs)[16], and graphene[17] were discovered.

These nanomaterials were the focus of significant scientific interest across the globe. In 2000, the United States federal government created the National Nanotechnology Initiative (NNI) to organize US-based nanoscience research efforts.[3, 18] As of 2016, the NNI had distributed over $22 billion of funding for nanotechnology research.[18] In the 2000s, publishers created new, peer-reviewed scientific journals dedicated to nanoscience. In the mid-2010s, the nanoscience field matured from one focused on discovering and synthesizing new nanomaterials to one that is working to integrate nanomaterials into functional devices for a wide variety of applications.

Currently, there is a large demand for smaller, more powerful, and versatile electronic devices. So far the development of computer processors has followed Gordon Moore's 1965 prediction that the number of transistors on circuit chips should double every two years.[19] Experts suggest that we are at, or rapidly approaching, a fundamental limit because we are unable to further shrink electronic components using current manufacturing techniques.[19, 20] Current research is dedicated to miniaturizing electronic components by developing molecular electronics[21, 22] and quantum computers[23-25]. On the other hand, small, flexible electronics[26, 27] are being engineered for wearable sensors.[27]

Developing "green" materials can reduce, or ultimately replace, the use of expensive metals in devices. Materials can also be engineered to improve a device's efficiency. Lithium-ion batteries are found in almost every modern portable electronic device. While they are beneficial because they are rechargeable, lithium-ion batteries are made with transition metals. These transition metals are expensive, have limited natural abundance, and there are significant social and environmental issues related to mining these metals, particularly cobalt.[28, 29] Significant work is devoted to developing more sustainable battery materials[30] from biomass[31], polymers[32, 33], and two-dimensional materials.[34]

Photovoltaic cells, or solar cells, are renewable energy devices that harvest energy from sunlight as an alternative to burning fossil fuels. There are efforts being made to improve the efficiency and reduce the cost of traditional bulk semiconductor solar cells. Quantum dots are nanostructures that absorb visible light due to quantum confinement; their color and absorbance can be tuned by changing their size. Semiconductor quantum dots (CdS, PbS, CdSe) are being pursued for use in solar cells.[35-37] Incorporating quantum dots could increase the photovoltaic device's efficiency due to increased absorption of the sun's incident radiation and enhanced charge transfer within the solar cell.[35, 36] In addition, sustainable materials for flexible electronics are being pursued.[38] Self-healing materials[39] are an attractive class of materials that could prolong the lifetime of electronic devices.

Nanoscience is critical for sensing applications as well. "Lab on a chip" (LOC) sensors are miniature microfluidic devices that are being developed for point-of-care diagnostics for acute diseases or monitoring glucose levels in diabetes patients.[40, 41] The goal is for an LOC device to provide the same diagnostic information as a medical lab test without utilizing the significant instrumentation and amount of resources typically required. At the time of this document's preparation, efforts are underway here at the University of Kansas in Dr. Steven Soper's lab to develop a LOC test for COVID-19.[42]

In addition, metallic nanostructures are integral for the development of plasmonic sensing devices. Plasmons are quantized oscillations of free electrons in metals; these oscillations are often resonant with visible to near-IR electromagnetic radiation.[43, 44] The plasmonic resonance can be tuned by manipulating the nanoparticles' size and shape.[44, 45] Any adsorbed material could shift this resonance, so plasmonic nanostructures are useful for biological[7, 46-48] and gas[48, 49] sensing applications.

Not only does the composition, size, and shape of nanoparticles affect their properties, so does their organization when adhered to a surface. The spacing of metal nanoparticles on a surface is known to affect their plasmonic resonance[50] and electric field enhancement[51]. The spacing of features on a surface is especially important to multivalently bind proteins.[52] For use in devices, nanomaterials must be in contact, or incorporated, with other materials which could alter the nanomaterials' behavior. Understanding how their properties change, at the nanoscale, due to their surface organization and interactions is essential to the development of practical nanodevices.

The remainder of this chapter discusses background information related to graphene and plasmonics, which are two materials considered for use in many different applications. The work in this dissertation focuses on locally probing and controlling dopant interactions with a graphene substrate, as well as increasing the versatility of fabrication methods for nanoscale metal features. Such work is important for bringing viable, manufacturable devices incorporating graphene or plasmonics to market.

1.2 Graphene Background Information

Graphene is a planar, single-layer of sp^2-hybridized carbon atoms arranged in a hexagonal lattice; this structure is shown in Figure 1.1. Until the early 2000s, it was thought that curved carbon structures such as carbon nanotubes (CNTs) were the most stable form of atomically-thin carbon.[17] In 2004, Andre Geim and Konstantin Novoselov were the first to isolate clean single layers of graphene from graphite using Scotch tape.[17] They were awarded the 2010 Novel Prize in Physics for their work isolating and characterizing graphene.[53] Geim and Novoselov's work sparked a massive research effort in understanding graphene and its unique

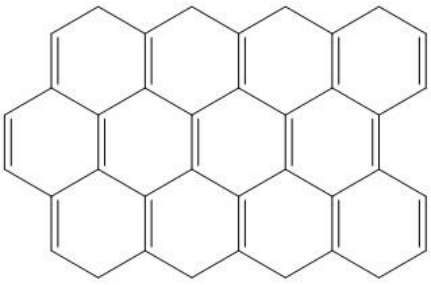

Figure 1.1: Planar, hexagonal graphene lattice.

properties. Graphene is being considered for use in photovoltaics[54, 55], catalysis[56, 57], energy storage[58-60], and sensing[60-63] applications.

1.2.1 Graphene Preparation Methods

Several methods exist to synthesize or isolate graphene sheets; the most common methods are discussed in this section. Mechanical exfoliation, or the "scotch tape" method, was the top-down approach for isolating graphene used by Andre Geim and Konstantin Novoselov in 2004.[17] Graphite is composed of stacked graphene layers that are held together by weak van der Waals interactions.[64, 65] Scotch tape can be used to cleave several layers off a graphite surface. This technique is routinely used in our research lab to expose a clean graphite surface. Once removed from the bulk substrate, the multilayers stuck to the tape were cleaved again then rubbed onto a desired substrate. Mostly multilayered graphene sheets were present on surfaces using this method, but single layers were identified.[17] Mechanical exfoliation in this manner is unsuitable for mass production and produces very small graphene films no larger than 10 μm in length and width.[17]

Chemical vapor deposition (CVD) is a bottom-up approach for synthesizing graphene that was first demonstrated in 2009 by Rodney Ruoff's research group.[66] A metal film is heated to very high temperatures inside a vacuum chamber to anneal the surface, flatten the metal grains, and eliminate surface contamination.[67] The vacuum environment also reduces surface oxidation of the synthesized graphene films.[67] Hydrocarbon gas (typically methane) is introduced into the vacuum chamber where it reacts to form an active complex. Then, the active complex adsorbs to the hot metal substrate where it decomposes. Reaction byproducts desorb and the graphene grains nucleate on the surface. This continues until the entire metal surface is covered with a graphene film.[67] CVD is thought to be the most promising method for scaling up graphene production in industry. Single-grain graphene sheets with centimeter dimensions have been grown, but growing larger sheets introduce grain boundaries and defects.[68] CVD growth is also limited to certain metal substrates.

Copper[66] is the most common substrate, but nickel and cobalt[67] have also been used in CVD growth of graphene. Furthermore, a complicated procedure is necessary to transfer the graphene film to the desired substrate; the "wet transfer" method is most common.[69] A polymer layer is deposited on top of the graphene film as a protective layer. Then, the entire polymer-graphene-copper sample is submerged in a solution that etches away the metal support. The polymer-graphene sheet floats to the solution's surface and the desired substrate can catch the film from below. Finally, the polymer resist is removed. This wet transfer method is complicated and presents challenges. The polymer residue often introduces contamination onto the graphene that is difficult to remove. Polymethylmethacrylate (PMMA) is the polymer most commonly used in this wet transfer method but it cannot be dissolved by organic solvents.[67] Graphene samples are normally thermally annealed to remove the polymer, but contamination often persists after this process.[67] A summary of the graphene growth mechanisms and strategies to improve CVD synthesis are discussed in recent review articles.[67, 70]

Exfoliation of graphite in solvent has also been demonstrated to isolate single graphene sheets.[71, 72] In brief, graphite is submerged in solvent and subjected to sonication that disrupts the weak interlayer van der Waals interactions. This technique allows one to produce graphene sheets dispersed in solvent, but the sheets are not very large. Liquid exfoliation produces graphene sheets with lateral dimensions between 100 nm – 100 μm.[71] In principle, one could deposit the graphene sheets on any desired substrate but there is no way to control the orientation of the sheets on the surface with this method. Other methods for producing graphene such as electrochemical synthesis, unzipping carbon nanotubes, irradiation of highly ordered pyrolytic graphite (HOPG), epitaxial growth on silicon carbide (SiC), and the chemical reduction of graphene oxide (rGO) are summarized in recent reviews.[73, 74]

Each graphene preparation method has its drawbacks. At this time, we are unable to produce large, defect-free graphene sheets in a manner than can be used for mass production. This is limiting graphene's widespread implementation, but research is being done to improve graphene growth.

1.2.2 Graphene's Native Properties & Electronic Band Structure

Graphene has unique properties for such a thin, carbon-based material. First, it is conductive. The out-of-plane $2p_z$ atomic orbitals, that are not involved in the sp^2 hybridization, overlap in a side-on fashion allowing delocalized π-electrons to flow across the sheet.[75] Graphene has a high charge carrier mobility that is measured to be between 10,000 – 200,000 $cm^2/(Vs)$ at room temperature.[17, 76] Because it is only a single-atom thick, it is mostly optically transparent. Graphene was found to absorb only 2.3% of incident white light.[77] Graphene is also remarkably strong and flexible for an atomically thin sheet. It was measured to have a Young's modulus of 1.0 TPa and a tensile strength of 130 GPa.[78] For reference, Kevlar (a material used for bulletproof vests) has a tensile modulus of 70,500 MPa (0.0705 TPa) and a tensile strength of 3,600 MPa (3.6 GPa).[79] Furthermore, graphene is made out of carbon – an abundant, nontoxic material.

Graphene also has a unique electronic band structure. At the Dirac points, the valence and conduction bands meet but do not overlap in energy.[75, 80] Therefore, graphene is known as a "zero bandgap semiconductor". Graphene's band structure makes it very sensitive to dopants. P-type doping the graphene (withdrawing electron density) would deplete graphene's valence band, create a bandgap, causing semiconductor-like behavior. On the other hand, adding n-type dopants (donating electron density) would populate the conduction band and cause metallic behavior. This behavior is illustrated in Figure 1.2.

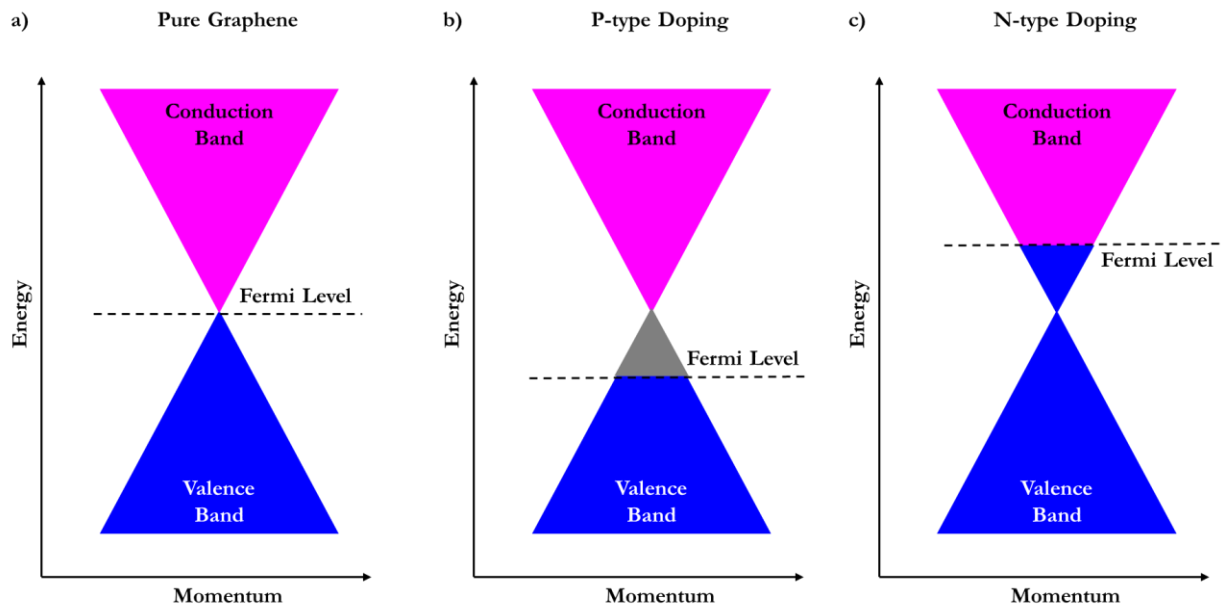

Figure 1.2: Two-dimensional picture of graphene's band structure at Dirac point. (a) Pure graphene. (b) P-type doping depletes electron density in valence band, opening a bandgap resulting in semiconductor-like behavior. (c) N-type doping adds electron density the conduction band, resulting in metallic-like behavior.

Despite synthesis challenges, graphene's unique properties make it attractive for a wide variety of applications that are summarized in recent review articles.[57, 59, 60, 63, 81-83] Some specific examples are listed here. First, graphene is of interest to energy-based applications. Indium tin oxide (ITO) is a material commonly used in dye-sensitized solar cells and transparent electrodes.[59, 63, 81, 84] Indium is a rare metal, therefore ITO is an expensive material. Transparent, flexible, and conductive graphene is an attractive alternative to costly, brittle ITO.[54, 55] Graphene has also been engineered for use as a capacitor or electrode in batteries to improve energy storage capabilities.[58, 59, 81, 85] Graphene could serve as an inexpensive alternative catalyst for oxygen reduction reactions (ORR)[56, 60] and hydrogen evolution reactions (HER)[63, 86]; this is particularly useful for fuel-cell development.

Graphene is also being developed for sensor applications.[60, 63, 82] Some specific examples include graphene-based sensors used to study pathogenic interactions[87], detect H_2S gas (toxic to humans)[88], protein binding studies[89], and electrochemical detection of targeted biomolecules.[61]

Again, a fundamental understanding of graphene's behavior and tailored manipulation of its properties is needed to improve device efficiency. For most of these applications, graphene's native properties must be modified to improve its performance. Specifically, doping of the graphene is necessary to modify its electronic properties.

1.2.3 Previous Studies Regarding Graphene Doping

The work function (Φ) of a material is defined as the amount of energy required to completely remove an electron from a solid. Pure graphene is estimated to have a work function of about 4.4 eV.[90] As stated previously, graphene's unique electronic band structure makes it very sensitive to doping. P-type dopants remove electron density, thereby increasing the work function and shifting the Fermi level to higher energy. N-type dopants increase electron density, thereby decreasing the work function and shifting the Fermi level to lower energy. In principle, graphene could be tailored to behave as either a semiconductor or metal with the proper dopants. Much research has been devoted to graphene doping and is summarized in recent review articles.[83, 91-96] Typical techniques used to characterize graphene dopants and their effect on the work function such as Raman spectroscopy[97-101], electrochemical sensors[102], field effect transistors (FETs)[103-107], IV curves[108], and photoelectron spectroscopy[109-111] are bulk measurements. These bulk measurements look at the doping effect over the entire graphene sheet, instead of at the dopant site. Little of this work is spatially resolved at the nanoscale.

Permanent modification to the graphene lattice can induce work function changes. For example, chemisorbed dopants can covalently functionalize graphene's surface.[112, 113] Structural changes induced by ion irradiation[114], UV irradiation[103], or nanolithography[108] can also modify graphene's work function. These methods induce permanent structural damage to the graphene lattice. Covalent functionalization typically reduces graphene's conductivity due to changing the carbon's hybridization from sp^2 to sp^3, which disrupts the conjugation of the π-system.[96]

We are primarily interested in studying dopants that do not permanently alter the graphene lattice. Physisorbed molecules are known to modify graphene's work function without damaging the lattice itself. Adsorbed molecules adhere through weak van der Waals interactions, but the strength of adsorption can be increased by using molecules that can π-stack against the graphene lattice.[83, 96, 97] Examples of π-stacking adsorbants that have been investigated on graphene or graphite are anthracene- and naphthalene-based molecules[98], the azobenzene methyl-orange dye[99], and ruthenium metal complexes with pyrene anchors.[115] Even material trapped between a graphene sheet and its substrate can cause work function modification. Existing evidence supports that water intercalated between the graphene sheet and its support affects its work function.[114, 116]

The doping methods mentioned here generally shift the work function up or down in energy by hundreds of milli-electron volts. Doping of graphene has been extensively demonstrated, but more work needs to be done in order to systematically control its magnitude and direction. For covalent and structural modification, the direction of the work function change is thought to be due to the nature of molecules covalently bound to defect sites. Several factors can influence the direction and magnitude of doping with noncovalent functionalization and these are described in more detail below.

As stated earlier, the work function (Φ) is traditionally defined as the amount of energy required to pull an electron completely away from a solid. This can be related to the material's chemical potential (μ) and surface dipole (D),[109, 110] as shown in Equation 1:

$$\Phi \propto \mu + D \tag{1}$$

The surface dipole exists because the surface atom's nuclei are fixed at the surface while electron density extends a bit beyond the nuclei's position.[110] The chemical potential is a bulk quantity that is not affected by surface modifications, but surface adsorbants can modify the surface dipole thereby

locally modifying the metal's work function.[110] For weakly bound physisorbed molecules on metals, there are three possible ways to modify the work function:[109-111]

1. Push-back or pillow effect: The surface dipole is reduced due to Pauli repulsion between electrons in the adsorbate and substrate.
2. Integer Charge Transfer: Electrons can tunnel between the adsorbate and substrate. The direction of tunneling depends on energy level alignment. This is shown in detail in Figure 1.3.
3. Additional modification of surface dipole.

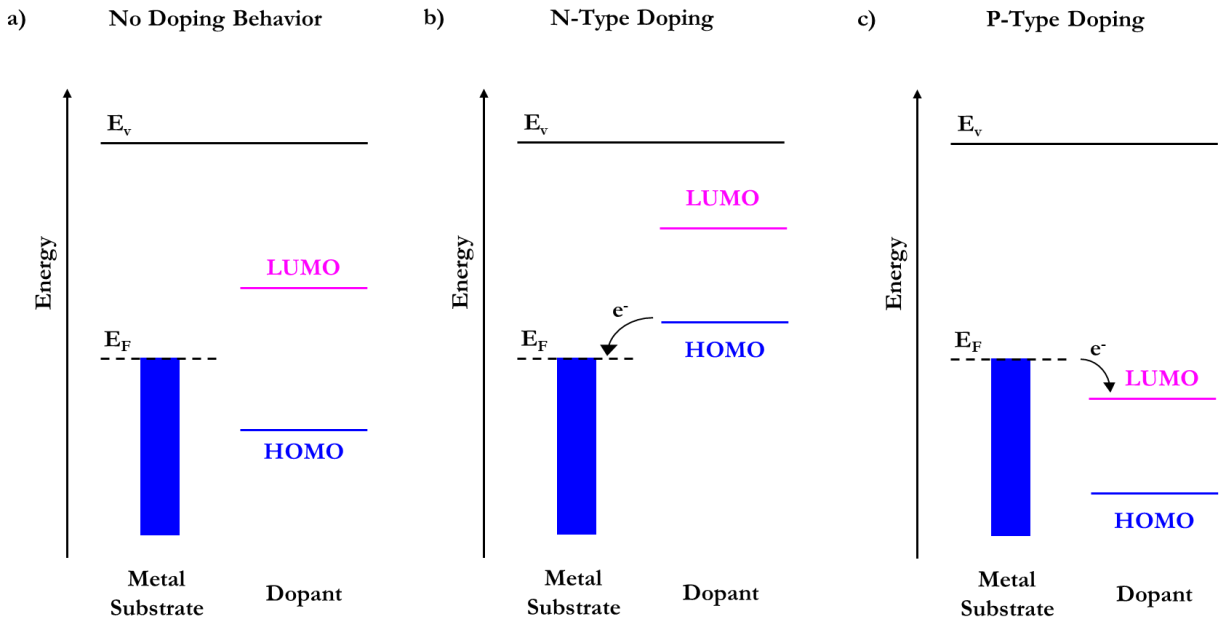

Figure 1.3: Energy level alignment between dopant and metal substrate for integer charge transfer model. E_F indicates the metal's Fermi level. E_v is vacuum. (a) No doping behavior. (b) N-type doping behavior. (c) P-type doping behavior.

In the integer charge transfer model, energy level alignment between the substrate and adsorbate are critical. If the metal's Fermi level is in between the dopant's frontier molecular orbitals' (FMOs) energies (Figure 1.3(a)), then no charge transfer occurs assuming that there is not enough thermally available energy to excite electrons. If the dopant's highest occupied molecular orbital (HOMO) is above the metal's Fermi level (Figure 1.3(b)), electron transfer from the dopant to the metal can

occur (n-type). If the dopant's lowest unoccupied molecular orbital (LUMO) is lower than the metal's Fermi level (Figure 1.3(c)), electron transfer from the metal to the dopant can occur (p-type).

It is difficult to extract which of these mechanisms is most important in current literature. Investigated physisorbed dopants are difficult to modify to systematically tune their interaction with graphene. Furthermore, most techniques used to characterize graphene dopants and their effect on the work function are bulk measurements. Most studies report doping occurs but exclude explanation for their observed doping magnitude and direction. Studies of dopant-graphene interactions on the molecular scale are needed to further probe how these dopants locally modify graphene's electronic properties in order to control the modification.

1.3 Overall Goals

This work focuses on understanding and manipulating nanoscale interactions in order to bring efficient nanodevices to market using versatile fabrication methods. Chapters 3 and 4 describe work related to locally probing tunable, physisorbed dopants for graphene. Chapter 5 focuses on designing a patternable salt-based resist layer that can withstand high temperature metal deposition.

Azulene is a unique conjugated organic molecule that has complimentary frontier molecular orbital (FMO) density. By placing substituents at strategic locations around the azulene framework, the energy of the highest occupied molecular orbital (HOMO) or lowest unoccupied molecular orbital (LUMO) can be independently tuned. We proposed using such molecules as a tunable dopant for graphene that could physisorb to the substrate without decreasing its native conductivity. Azulene-based molecules provide a systematic method for studying how shifting the dopant's frontier energy levels could locally modify the substrate's work function. In all experiments presented in this dissertation, highly ordered pyrolytic graphite (HOPG) was used instead of graphene. HOPG is an ideal substitute for graphene because they are chemically identical, have

similar electronic properties, and HOPG substrates are more consistent than graphene. A more detailed comparison of the two substrates is included in the beginning of Chapter 3.

Chapter 3 summarizes efforts to optimize deposition conditions of azulene and its structural isomer, naphthalene, onto graphite in addition to characterizing their interaction with the substrate using scanning probe microscopy. Noncontact atomic force microscopy (NCAFM) is used to provide local topographical images of these molecules adsorbed to graphite. We were interested in observing the surface coverage of these molecules and identifying how isolated adsorbates interact with the surface. Kelvin probe force microscopy (KPFM) was done simultaneously with NCAFM to map the relative, local effect of the adsorbed molecules on graphite's local work function as well as to determine the lateral dimensions of the doping effect. In Chapter 4, we repeated these experiments using substituted azulenes. This work provides local information about how an isolated, physisorbed dopant modifies surface properties that is currently lacking in literature. Furthermore, using azulene-based molecules could potentially provide a level of control over the magnitude and direction of the local doping effect that has not been fully explored. This work investigates whether we observe a change in the local doping effect by adsorbing different substituted azulenes onto a graphite surface. Having control over how a dopant modifies a substrate's electronic properties allows us to engineer a material's behavior for a desired application.

While Chapters 3 and 4 focus on studying the arrangement and properties of dopants on the molecular level, Chapter 5 is related to controlling the specific orientation of metal nanostructures on a surface. The work in Chapter 5 aims to increase the versatility of metallic nanostructure growth for plasmonic applications. Plasmonic sensing devices require precise control over the size, placement, and orientation of metallic nanostructures on a substrate. Common lithographic techniques utilize patternable organic resist layers for bottom-up metal nanostructure fabrication. However, these organic resist layers sometimes require specific substrates, are difficult to remove,

and decompose under high-heat conditions. We conducted a proof of concept experiment using NaCl as a novel resist layer that could, in principle, physisorb to any substrate, potentially withstand high-heat metal deposition conditions, and be easily removed with a water rinse. We tested if such a layer was patternable using scanning probe lithography, thereby allowing us to control the dimensions and placement of metal nanostructures grown on the surface. And finally, we tested if an NaCl resist layer could withstand high temperature metal deposition conditions and create defined metal features on a substrate. Using such a versatile resist layer would increase the viability of manufacturing metal nanostructures on a large scale, bringing us closer to having profitable plasmonic sensing devices in market.

The purpose of the research presented in this dissertation is to understand, and control, local nanoscale modifications at interfaces. By mapping the effects of single molecules physisorbed to a surface, we aimed to explain how a dopant's structure dictates its effect on the local work function. We also developed a novel resist layer that increases the versatility of bottom-up metal nanostructure fabrication. Understanding and controlling nanomaterial's behavior as they are incorporated into more complicated devices is essential to rapidly bring practical implementations of nanomaterials to market.

1.4 References

1. Franken, L. E.; Grünewald, K.; Boekema, E. J.; Stuart, M. C. A., A Technical Introduction to Transmission Electron Microscopy for Soft-Matter: Imaging, Possibilities, Choices, and Technical Developments. *Small* **2020,** *16* (14), 1906198.

2. Bogner, A.; Jouneau, P. H.; Thollet, G.; Basset, D.; Gauthier, C., A history of scanning electron microscopy developments: Towards "wet-STEM" imaging. *Micron* **2007,** *38* (4), 390-401.

3. Nanotechnology Timeline. https://www.nano.gov/timeline (accessed January 14, 2021).

4. Feynman, R. P., There's plenty of room at the bottom. *Resonance* **2011,** *16* (9), 890.

5. Binnig, G.; Rohrer, H.; Gerber, C.; Weibel, E., Tunneling through a controllable vacuum gap. *Applied Physics Letters* **1981,** *40* (2), 178-180.

6. Binnig, G.; Quate, C. F.; Gerber, C., Atomic Force Microscope. *Physical Review Letters* **1986,** *56* (9), 930-933.

7. Anker, J. N.; Hall, W. P.; Lyandres, O.; Shah, N. C.; Zhao, J.; Van Duyne, R. P., Biosensing with plasmonic nanosensors. *Nature Materials* **2008,** *7* (6), 442-453.

8. Roh, J.; Yi, J.; Kim, Y., Rapid, Reversible Preparation of Size-Controllable Silver Nanoplates by Chemical Redox. *Langmuir* **2010,** *26* (14), 11621-11623.

9. Requejo, K. I.; Liopo, A. V.; Derry, P. J.; Zubarev, E. R., Accelerating Gold Nanorod Synthesis with Nanomolar Concentrations of Poly(vinylpyrrolidone). *Langmuir* **2017,** *33* (44), 12681-12688.

10. Zheng, K.; Setyawati, M. I.; Leong, D. T.; Xie, J., Antimicrobial Gold Nanoclusters. *ACS Nano* **2017,** *11* (7), 6904-6910.

11. Medici, S.; Peana, M.; Nurchi, V. M.; Zoroddu, M. A., Medical Uses of Silver: History, Myths, and Scientific Evidence. *Journal of Medicinal Chemistry* **2019,** *62* (13), 5923-5943.

12. Cuenya, B. R., Synthesis and catalytic properties of metal nanoparticles: Size, shape, support, composition, and oxidation state effects. *Thin Solid Films* **2010,** *518* (12), 3127-3150.

13. Cao, Y.; Yang, Y.; Shan, Y.; Huang, Z., One-Pot and Facile Fabrication of Hierarchical Branched Pt–Cu Nanoparticles as Excellent Electrocatalysts for Direct Methanol Fuel Cells. *ACS Applied Materials & Interfaces* **2016,** *8* (9), 5998-6003.

14. Hong, C.; Jin, X.; Totleben, J.; Lohrman, J.; Harak, E.; Subramaniam, B.; Chaudhari, R. V.; Ren, S., Graphene oxide stabilized Cu2O for shape selective nanocatalysis. *Journal of Materials Chemistry A* **2014,** *2* (20), 7147-7151.

15. Kroto, H. W.; Heath, J. R.; O'Brien, S. C.; Curl, R. F.; Smalley, R. E., C60: Buckminsterfullerene. *Nature* **1985,** *318* (6042), 162-163.

16. Iijima, S., Helical microtubules of graphitic carbon. *Nature* **1991,** *354* (6348), 56-58.

17. Novoselov, K. S.; Geim, A. K.; Morozov, S. V.; Jiang, D.; Zhang, Y.; Dubonos, S. V.; Grigorieva, I. V.; Firsov, A. A., Electric Field Effect in Atomically Thin Carbon Films. *Science* **2004,** *306* (5696), 666-669.

18. Cheng, H. N.; Doemeny, L. J.; Geraci, C. L.; Grob Schmidt, D., Nanotechnology Overview: Opportunities and Challenges. In *Nanotechnology: Delivering on the Promise Volume 1*, American Chemical Society: 2016; Vol. 1220, pp 1-12.

19. Bentley, P. The end of Moore's Law: what happens next? *Science Focus* [Online], 2018. https://www.sciencefocus.com/future-technology/when-the-chips-are-down/ (accessed November 17, 2020).

20. Rotman, D. We're not prepared for the end of Moore's Law *MIT Technology Review* [Online], 2020. https://www.technologyreview.com/2020/02/24/905789/were-not-prepared-for-the-end-of-moores-law/ (accessed November 17, 2020).

21. Vilan, A.; Aswal, D.; Cahen, D., Large-Area, Ensemble Molecular Electronics: Motivation and Challenges. *Chemical Reviews* **2017,** *117* (5), 4248-4286.

22. Nichols, R. J.; Higgins, S. J., Single-Molecule Electronics: Chemical and Analytical Perspectives. *Annual Review of Analytical Chemistry* **2015,** *8* (1), 389-417.

23. Ladd, T. D.; Jelezko, F.; Laflamme, R.; Nakamura, Y.; Monroe, C.; O'Brien, J. L., Quantum computers. *Nature* **2010,** *464* (7285), 45-53.

24. Cao, Y.; Romero, J.; Olson, J. P.; Degroote, M.; Johnson, P. D.; Kieferová, M.; Kivlichan, I. D.; Menke, T.; Peropadre, B.; Sawaya, N. P. D.; Sim, S.; Veis, L.; Aspuru-Guzik, A., Quantum Chemistry in the Age of Quantum Computing. *Chemical Reviews* **2019,** *119* (19), 10856-10915.

25. Bauer, B.; Bravyi, S.; Motta, M.; Kin-Lic Chan, G., Quantum Algorithms for Quantum Chemistry and Quantum Materials Science. *Chemical Reviews* **2020**.

26. Liu, X.; Long, Y.-Z.; Liao, L.; Duan, X.; Fan, Z., Large-Scale Integration of Semiconductor Nanowires for High-Performance Flexible Electronics. *ACS Nano* **2012,** *6* (3), 1888-1900.

27. Liu, Y.; He, K.; Chen, G.; Leow, W. R.; Chen, X., Nature-Inspired Structural Materials for Flexible Electronic Devices. *Chemical Reviews* **2017,** *117* (20), 12893-12941.

28. . The toll of the cobalt mining industry on health and the environment *CBS News* [Online], 2018. https://www.cbsnews.com/news/the-toll-of-the-cobalt-mining-industry-congo/ (accessed November 17, 2020).

29. Mucha, L. F., Todd C. Sadof, Karly Domb. The hidden costs of cobalt mining *The Washington Post* [Online], 2018. https://www.washingtonpost.com/news/in-sight/wp/2018/02/28/the-cost-of-cobalt/ (accessed November 17, 2020).

30. Sharma, S. S.; Manthiram, A., Towards more environmentally and socially responsible batteries. *Energy & Environmental Science* **2020,** *13* (11), 4087-4097.

31. Liedel, C., Sustainable Battery Materials from Biomass. *ChemSusChem* **2020,** *13* (9), 2110-2141.

32. Miroshnikov, M.; Divya, K. P.; Babu, G.; Meiyazhagan, A.; Reddy Arava, L. M.; Ajayan, P. M.; John, G., Power from nature: designing green battery materials from electroactive quinone derivatives and organic polymers. *Journal of Materials Chemistry A* **2016,** *4* (32), 12370-12386.

33. Jia, X.; Ge, Y.; Shao, L.; Wang, C.; Wallace, G. G., Tunable Conducting Polymers: Toward Sustainable and Versatile Batteries. *ACS Sustainable Chemistry & Engineering* **2019,** *7* (17), 14321-14340.

34. Rojaee, R.; Shahbazian-Yassar, R., Two-Dimensional Materials to Address the Lithium Battery Challenges. *ACS Nano* **2020,** *14* (3), 2628-2658.

35. Kamat, P. V., Quantum Dot Solar Cells. Semiconductor Nanocrystals as Light Harvesters. *The Journal of Physical Chemistry C* **2008,** *112* (48), 18737-18753.

36. Kamat, P. V., Quantum Dot Solar Cells. The Next Big Thing in Photovoltaics. *The Journal of Physical Chemistry Letters* **2013,** *4* (6), 908-918.

37. Scott, R.; Kirkeminde, A.; Gong, M.; Totleben, J.; Ren, S.; Tuinenga, C.; Lewis, C.; Luo, H.; Higgins, D.; Chikan, V., (Invited) Impact of Indiumand Gallium Doping on the Photovoltaic Performance of CdSe Quantum Dot Hybrid Solar Cells. *ECS Transactions* **2015,** *66* (15), 1-8.

38. Fu, Q.; Chen, Y.; Sorieul, M., Wood-Based Flexible Electronics. *ACS Nano* **2020,** *14* (3), 3528-3538.

39. Tan, Y. J.; Wu, J.; Li, H.; Tee, B. C. K., Self-Healing Electronic Materials for a Smart and Sustainable Future. *ACS Applied Materials & Interfaces* **2018,** *10* (18), 15331-15345.

40. Azizipour, N.; Avazpour, R.; Rosenzweig, D. H.; Sawan, M.; Ajji, A., Evolution of Biochip Technology: A Review from Lab-on-a-Chip to Organ-on-a-Chip. *Micromachines (Basel)* **2020,** *11* (6), 599.

41. Wongkaew, N.; Simsek, M.; Griesche, C.; Baeumner, A. J., Functional Nanomaterials and Nanostructures Enhancing Electrochemical Biosensors and Lab-on-a-Chip Performances: Recent Progress, Applications, and Future Perspective. *Chemical Reviews* **2019,** *119* (1), 120-194.

42. Howard, C. KU Researchers Developing Quick-Turnaround COVID-19 Test. 2020. https://today.ku.edu/ku-researchers-developing-quick-turnaround-covid-19-test (accessed November 17, 2020).

43. Khlebtsov, B. N.; Khanadeev, V. A.; Burov, A. M.; Le Ru, E. C.; Khlebtsov, N. G., Reexamination of Surface-Enhanced Raman Scattering from Gold Nanorods as a Function of Aspect Ratio and Shape. *The Journal of Physical Chemistry C* **2020,** *124* (19), 10647-10658.

44. El-Sayed, M. A., Some Interesting Properties of Metals Confined in Time and Nanometer Space of Different Shapes. *Accounts of Chemical Research* **2001,** *34* (4), 257-264.

45. Khan, A. U.; Zhao, S.; Liu, G., Key Parameter Controlling the Sensitivity of Plasmonic Metal Nanoparticles: Aspect Ratio. *The Journal of Physical Chemistry C* **2016,** *120* (34), 19353-19364.

46. Lee, S. Y.; Kim, S.-H.; Jang, S. G.; Heo, C.-J.; Shim, J. W.; Yang, S.-M., High-Fidelity Optofluidic On-Chip Sensors Using Well-Defined Gold Nanowell Crystals. *Analytical Chemistry* **2011,** *83* (23), 9174-9180.

47. Deng, W.; Goldys, E. M., Plasmonic Approach to Enhanced Fluorescence for Applications in Biotechnology and the Life Sciences. *Langmuir* **2012,** *28* (27), 10152-10163.

48. Päivänranta, B.; Merbold, H.; Giannini, R.; Büchi, L.; Gorelick, S.; David, C.; Löffler, J. F.; Feurer, T.; Ekinci, Y., High Aspect Ratio Plasmonic Nanostructures for Sensing Applications. *ACS Nano* **2011,** *5* (8), 6374-6382.

49. Chong, X.; Zhang, Y.; Li, E.; Kim, K.-J.; Ohodnicki, P. R.; Chang, C.-h.; Wang, A. X., Surface-Enhanced Infrared Absorption: Pushing the Frontier for On-Chip Gas Sensing. *ACS Sensors* **2018,** *3* (1), 230-238.

50. Vazquez-Mena, O.; Sannomiya, T.; Villanueva, L. G.; Voros, J.; Brugger, J., Metallic Nanodot Arrays by Stencil Lithography for Plasmonic Biosensing Applications. *ACS Nano* **2011,** *5* (2), 844-853.

51. Zou, S.; Schatz, G. C., Silver nanoparticle array structures that produce giant enhancements in electromagnetic fields. *Chemical Physics Letters* **2005,** *403* (1), 62-67.

52. Rinker, S.; Ke, Y.; Liu, Y.; Chhabra, R.; Yan, H., Self-assembled DNA nanostructures for distance-dependent multivalent ligand–protein binding. *Nature Nanotechnology* **2008,** *3* (7), 418-422.

53. The Nobel Prize in Physics 2010 Press Release. https://www.nobelprize.org/prizes/physics/2010/press-release/ (accessed November 17, 2020).

54. Wu, J.; Becerril, H. A.; Bao, Z.; Liu, Z.; Chen, Y.; Peumans, P., Organic solar cells with solution-processed graphene transparent electrodes. *Applied Physics Letters* **2008,** *92* (26), 263302.

55. Gomez De Arco, L.; Zhang, Y.; Schlenker, C. W.; Ryu, K.; Thompson, M. E.; Zhou, C., Continuous, Highly Flexible, and Transparent Graphene Films by Chemical Vapor Deposition for Organic Photovoltaics. *ACS Nano* **2010,** *4* (5), 2865-2873.

56. Lin, Z.; Song, M.-k.; Ding, Y.; Liu, Y.; Liu, M.; Wong, C.-p., Facile preparation of nitrogen-doped graphene as a metal-free catalyst for oxygen reduction reaction. *Physical Chemistry Chemical Physics* **2012,** *14* (10), 3381-3387.

57. Navalon, S.; Dhakshinamoorthy, A.; Alvaro, M.; Garcia, H., Carbocatalysis by Graphene-Based Materials. *Chemical Reviews* **2014,** *114* (12), 6179-6212.

58. Wang, D.; Wang, X., Self-Assembled Graphene/Azo Polyelectrolyte Multilayer Film and Its Application in Electrochemical Energy Storage Device. *Langmuir* **2011,** *27* (5), 2007-2013.

59. Huang, X.; Zeng, Z.; Fan, Z.; Liu, J.; Zhang, H., Graphene-Based Electrodes. *Advanced Materials* **2012,** *24* (45), 5979-6004.

60. Rao, C. N. R.; Gopalakrishnan, K.; Maitra, U., Comparative Study of Potential Applications of Graphene, MoS2, and Other Two-Dimensional Materials in Energy Devices, Sensors, and Related Areas. *ACS Applied Materials & Interfaces* **2015,** *7* (15), 7809-7832.

61. Wang, L.; Xu, M.; Han, L.; Zhou, M.; Zhu, C.; Dong, S., Graphene Enhanced Electron Transfer at Aptamer Modified Electrode and Its Application in Biosensing. *Analytical Chemistry* **2012,** *84* (17), 7301-7307.

62. Lee, S.; Kumar, P.; Hu, Y.; Cheng, G. J.; Irudayaraj, J., Graphene laminated gold bipyramids as sensitive detection platforms for antibiotic molecules. *Chemical Communications* **2015,** *51* (85), 15494-15497.

63. Rezapour, M. R.; Myung, C. W.; Yun, J.; Ghassami, A.; Li, N.; Yu, S. U.; Hajibabaei, A.; Park, Y.; Kim, K. S., Graphene and Graphene Analogs toward Optical, Electronic, Spintronic, Green-Chemical, Energy-Material, Sensing, and Medical Applications. *ACS Applied Materials & Interfaces* **2017,** *9* (29), 24393-24406.

64. Chung, D. D. L., Review Graphite. *Journal of Materials Science* **2002,** *37* (8), 1475-1489.

65. McCreery, R. L., Advanced Carbon Electrode Materials for Molecular Electrochemistry. *Chemical Reviews* **2008,** *108* (7), 2646-2687.

66. Li, X.; Cai, W.; An, J.; Kim, S.; Nah, J.; Yang, D.; Piner, R.; Velamakanni, A.; Jung, I.; Tutuc, E.; Banerjee, S. K.; Colombo, L.; Ruoff, R. S., Large-Area Synthesis of High-Quality and Uniform Graphene Films on Copper Foils. *Science* **2009,** *324* (5932), 1312-1314.

67. Lin, L.; Deng, B.; Sun, J.; Peng, H.; Liu, Z., Bridging the Gap between Reality and Ideal in Chemical Vapor Deposition Growth of Graphene. *Chemical Reviews* **2018,** *118* (18), 9281-9343.

68. Nguyen, V. L.; Lee, Y. H., Towards Wafer-Scale Monocrystalline Graphene Growth and Characterization. *Small* **2015,** *11* (29), 3512-3528.

69. Lin, Y.-C.; Lu, C.-C.; Yeh, C.-H.; Jin, C.; Suenaga, K.; Chiu, P.-W., Graphene Annealing: How Clean Can It Be? *Nano Letters* **2012,** *12* (1), 414-419.

70. Sun, J.; Chen, Y.; Priydarshi, M. K.; Chen, Z.; Bachmatiuk, A.; Zou, Z.; Chen, Z.; Song, X.; Gao, Y.; Rümmeli, M. H.; Zhang, Y.; Liu, Z., Direct Chemical Vapor Deposition-Derived Graphene Glasses Targeting Wide Ranged Applications. *Nano Letters* **2015,** *15* (9), 5846-5854.

71. Backes, C.; Higgins, T. M.; Kelly, A.; Boland, C.; Harvey, A.; Hanlon, D.; Coleman, J. N., Guidelines for Exfoliation, Characterization and Processing of Layered Materials Produced by Liquid Exfoliation. *Chemistry of Materials* **2017,** *29* (1), 243-255.

72. Lavin-Lopez, M. P.; Valverde, J. L.; Sanchez-Silva, L.; Romero, A., Solvent-Based Exfoliation via Sonication of Graphitic Materials for Graphene Manufacture. *Industrial & Engineering Chemistry Research* **2016,** *55* (4), 845-855.

73. Lee, H. C.; Liu, W.-W.; Chai, S.-P.; Mohamed, A. R.; Aziz, A.; Khe, C.-S.; Hidayah, N. M. S.; Hashim, U., Review of the synthesis, transfer, characterization and growth mechanisms of single and multilayer graphene. *RSC Advances* **2017,** *7* (26), 15644-15693.

74. Guo, S.; Dong, S., Graphene nanosheet: synthesis, molecular engineering, thin film, hybrids, and energy and analytical applications. *Chemical Society Reviews* **2011,** *40* (5), 2644-2672.

75. Yang, G.; Li, L.; Lee, W. B.; Ng, M. C., Structure of graphene and its disorders: a review. *Sci Technol Adv Mater* **2018,** *19* (1), 613-648.

76. Bolotin, K. I.; Sikes, K. J.; Jiang, Z.; Klima, M.; Fudenberg, G.; Hone, J.; Kim, P.; Stormer, H. L., Ultrahigh electron mobility in suspended graphene. *Solid State Communications* **2008,** *146* (9), 351-355.

77. Nair, R. R.; Blake, P.; Grigorenko, A. N.; Novoselov, K. S.; Booth, T. J.; Stauber, T.; Peres, N. M. R.; Geim, A. K., Fine Structure Constant Defines Visual Tranparency of Graphene. *Science* **2008,** *320* (5881), 1308-1308.

78. Lee, C.; Wei, X.; Kysar, J. W.; Hone, J., Measurement of the Elastic Properties and Intrinsic Strength of Monolayer Graphene. *Science* **2008,** *321* (5887), 385-388.

79. Dupont Kevlar Aramid Fiber Technical Guide. https://www.dupont.com/content/dam/dupont/amer/us/en/safety/public/documents/en/Kevlar_Technical_Guide_0319.pdf (accessed November 17, 2020).

80. Lonkar, S. P.; Deshmukh, Y. S.; Abdala, A. A., Recent advances in chemical modifications of graphene. *Nano Research* **2015,** *8* (4), 1039-1074.

81. Yang, Z.; Ren, J.; Zhang, Z.; Chen, X.; Guan, G.; Qiu, L.; Zhang, Y.; Peng, H., Recent Advancement of Nanostructured Carbon for Energy Applications. *Chemical Reviews* **2015,** *115* (11), 5159-5223.

82. Singh, E.; Meyyappan, M.; Nalwa, H. S., Flexible Graphene-Based Wearable Gas and Chemical Sensors. *ACS Applied Materials & Interfaces* **2017,** *9* (40), 34544-34586.

83. Georgakilas, V.; Tiwari, J. N.; Kemp, K. C.; Perman, J. A.; Bourlinos, A. B.; Kim, K. S.; Zboril, R., Noncovalent Functionalization of Graphene and Graphene Oxide for Energy Materials, Biosensing, Catalytic, and Biomedical Applications. *Chemical Reviews* **2016,** *116* (9), 5464-5519.

84. Wassei, J. K.; Kaner, R. B., Graphene, a promising transparent conductor. *Materials Today* **2010,** *13* (3), 52-59.

85. Zhang, X.; Marschewski, E.; Penner, P.; Weimann, T.; Hinze, P.; Beyer, A.; Gölzhäuser, A., Large-Area All-Carbon Nanocapacitors from Graphene and Carbon Nanomembranes. *ACS Nano* **2018,** *12* (10), 10301-10309.

86. Xie, A.; Xuan, N.; Ba, K.; Sun, Z., Pristine Graphene Electrode in Hydrogen Evolution Reaction. *ACS Applied Materials & Interfaces* **2017,** *9* (5), 4643-4648.

87. Fardin, G. M.; Daniel, L.; Kai, L.; Julian, S.; Benjamin, Z.; Nikolai, S.; Christoph, B.; P., R. J.; Andreas, H.; Mohsen, A.; Rainer, H., Functionalized Graphene as Extracellular Matrix Mimics: Toward Well-Defined 2D Nanomaterials for Multivalent Virus Interactions. *Advanced Functional Materials* **2017,** *27* (15), 1606477.

88. Mohammadi-Manesh, E.; Vaezzadeh, M.; Saeidi, M., Cu- and CuO-decorated graphene as a nanosensor for H2S detection at room temperature. *Surface Science* **2015,** *636*, 36-41.

89. Alava, T.; Mann, J. A.; Théodore, C.; Benitez, J. J.; Dichtel, W. R.; Parpia, J. M.; Craighead, H. G., Control of the Graphene–Protein Interface Is Required To Preserve Adsorbed Protein Function. *Analytical Chemistry* **2013,** *85* (5), 2754-2759.

90. Czerw, R.; Foley, B.; Tekleab, D.; Rubio, A.; Ajayan, P. M.; Carroll, D. L., Substrate-interface interactions between carbon nanotubes and the supporting substrate. *Physical Review B* **2002,** *66* (3), 033408.

91. Xue, Y.; Wu, B.; Bao, Q.; Liu, Y., Controllable Synthesis of Doped Graphene and Its Applications. *Small* **2014,** *10* (15), 2975-2991.

92. Pinto, H.; Markevich, A., Electronic and electrochemical doping of graphene by surface adsorbates. *Beilstein Journal of Nanotechnology* **2014,** *5*, 1842-1848.

93. Garg, R.; Dutta, N. K.; Choudhury, N. R., Work Function Engineering of Graphene. *nanomaterials* **2014,** *4*, 267-300.

94. Guo, B.; Fang, L.; Zhang, B.; Gong, J. R., Graphene Doping: A Review. *Insciences Journal* **2011,** *1* (2), 80-89.

95. Wei, W.; Qu, X., Extraordinary Physical Properties of Functionalized Graphene. *Small* **2012,** *8* (14), 2138-2151.

96. Zhang, Z.; Huang, H.; Yang, X.; Zang, L., Tailoring Electronic Properties of Graphene by π–π Stacking with Aromatic Molecules. *The Journal of Physical Chemistry Letters* **2011,** *2* (22), 2897-2905.

97. Deka, M. J.; Chowdhury, D., Tuning Electrical Properties of Graphene with Different P-Stacking Organic Molecules. *Journal of Physical Chemistry C* **2016,** *120*, 4121-4129.

98. Xiaochen, D.; Dongliang, F.; Wenjing, F.; Yumeng, S.; Peng, C.; Lain-Jong, L., Doping Single-Layer Graphene with Aromatic Molecules. *Small* **2009,** *5* (12), 1422-1426.

99. Peimyoo, N.; Yu, T.; Shang, J.; Cong, C.; Yang, H., Thickness-dependent azobenzene doping in mono- and few-layer graphene. *Carbon* **2012,** *50* (1), 201-208.

100. Wang, R.; Wang, S.; Zhang, D.; Li, Z.; Fang, Y.; Qiu, X., Control of Carrier Type and Density in Exfoliated Graphene by Interface Engineering. *ACS Nano* **2011,** *5* (1), 408-412.

101. Hinnemo, M.; Zhao, J.; Ahlberg, P.; Hägglund, C.; Djurberg, V.; Scheicher, R. H.; Zhang, S.-L.; Zhang, Z.-B., On Monolayer Formation of Pyrenebutyric Acid on Graphene. *Langmuir* **2017,** *33* (15), 3588-3593.

102. Kulkarni, G. S.; Reddy, K.; Zang, W.; Lee, K.; Fan, X.; Zhong, Z., Electrical Probing and Tuning of Molecular Physisorption on Graphene. *Nano Letters* **2016,** *16* (1), 695-700.

103. Luo, Z.; Pinto, N. J.; Davila, Y.; Johnson, A. T. C., Controlled doping of graphene using ultraviolet irradiation. *Applied Physics Letters* **2012,** *100* (25), 253108.

104. Gu, G.; Xie, Z., Modulation doping of graphene: An approach toward manufacturable devices. *Applied Physics Letters* **2011,** *98* (8), 083502.

105. Wang, Z.; Liu, J.; Hao, X.; Wang, Y.; Chen, Y.; Li, P.; Dong, M., Investigating the stability of molecule doped graphene field effect transistors. *New Journal of Chemistry* **2019,** *43* (38), 15275-15279.

106. Yuan, H.; Chang, S.; Bargatin, I.; Wang, N. C.; Riley, D. C.; Wang, H.; Schwede, J. W.; Provine, J.; Pop, E.; Shen, Z.-X.; Pianetta, P. A.; Melosh, N. A.; Howe, R. T., Engineering Ultra-Low Work Function of Graphene. *Nano Letters* **2015,** *15* (10), 6475-6480.

107. Farmer, D. B.; Golizadeh-Mojarad, R.; Perebeinos, V.; Lin, Y.-M.; Tulevski, G. S.; Tsang, J. C.; Avouris, P., Chemical Doping and Electron−Hole Conduction Asymmetry in Graphene Devices. *Nano Letters* **2009,** *9* (1), 388-392.

108. Liu, J.; Xu, G.; Rochford, C.; Lu, R.; Wu, J.; Edwards, C. M.; Berrie, C. L.; Chen, Z.; Maroni, V. A., Doped Graphene Nanohole Arrays for Flexible Transparent Conductors. *Applied Physics Letters* **2011,** *99*.

109. Otero, R.; Vázquez de Parga, A. L.; Gallego, J. M., Electronic, structural and chemical effects of charge-transfer at organic/inorganic interfaces. *Surface Science Reports* **2017,** *72* (3), 105-145.

110. Braun, S.; Salaneck, W. R.; Fahlman, M., Energy-Level Alignment at Organic/Metal and Organic/Organic Interfaces. *Advanced Materials* **2009,** *21* (14-15), 1450-1472.

111. Franco-Cañellas, A.; Duhm, S.; Gerlach, A.; Schreiber, F., Binding and electronic level alignment of π-conjugated systems on metals. *Reports on Progress in Physics* **2020,** *83* (6), 066501.

112. Wang, X.; Li, X.; Zhang, L.; Yoon, Y.; Weber, P. K.; Wang, H.; Guo, J.; Dai, H., N-Doping of Graphene through Electrothermal Reactions with Ammonia. *Science* **2009,** *324* (5928), 768-771.

113. Choi, J.; Kim, K.-j.; Kim, B.; Lee, H.; Kim, S., Covalent Functionalization of Epitaxial Graphene by Azidotrimethylsilane. *The Journal of Physical Chemistry C* **2009,** *113* (22), 9433-9435.

114. Ochedowski, O.; Bussmann, B. K.; d'Etat, B. B.; Lebius, H.; Schleberger, M., Manipulation of the graphene surface potential by ion irradiation. *Applied Physics Letters* **2013,** *102* (15), 153103.

115. Ozawa, H.; Katori, N.; Kita, T.; Oka, S.; Haga, M.-a., Controlling the Molecular Direction of Dinuclear Ruthenium Complexes on HOPG Surface through Noncovalent Bonding. *Langmuir* **2017,** *33* (43), 11901-11910.

116. Ochedowski, O.; Bussmann, B. K.; Schleberger, M., Graphene on Mica - Intercalated Water Trapped for Life. *Scientific Reports* **2014,** *4*, 6003.

Chapter 2: Methods & Instrumentation

2.1 Summary

This chapter provides a brief overview of the theory and implementation of versatile atomic force microscopy (AFM) techniques relevant to this work. Contact- and tapping-mode AFM were used to map samples' topography in ambient conditions. Contact AFM was also used as a nanolithography tool to create nanoscale patterns on surfaces. In an ultrahigh vacuum environment, noncontact AFM (NCAFM) was operated simultaneously with Kelvin probe force microscopy (KPFM) to obtain topography and surface potential maps of molecules adsorbed to graphite. Previously published literature has used KPFM to map surface potential changes from relatively large features or domains of densely packed molecules. We have shown that KPFM can also be used to map local surface potential modifications from small, isolated, physisorbed organic molecules at the molecular scale.

2.2 Overview & Development of Scanning Probe Microscopy

This chapter describes the theory and implementation of scanning probe microscopy (SPM) techniques integral to the research presented in this dissertation. Scanning tunneling microscopy (STM), the first scanning probe technique, was developed in 1982 by Gerd Binnig and Heinrich Rohrer at IBM.[1] STM allowed researchers to clearly map features with nanoscale, or even atomic, dimensions. Now, STM is as essential tool in surface science and nano-related research.

STM utilizes electron's quantum behavior to obtain better resolution than traditional optical microscopy. A sharp, conductive probe tip, typically made from tungsten (W) or a platinum-iridium (PtIr) alloy, is lowered close to a conductive surface without making contact. A voltage is applied between the tip and sample, forcing electrons to tunnel between them, thereby generating a current. This tunneling current is exponentially dependent on the distance between the tip and sample. As

the tip is scanned laterally over the surface, the tunneling current is used as a feedback loop to maintain the tip's distance above the sample. A piezoelectric motor adjusts the height of the tip relative to the surface to maintain the tunneling current, generating a topographical map of the surface. Soon after the first STM-related publication[1], atomic resolution was achieved on an annealed Si(111) 7x7 surface.[2] Extremely sharp STM tips are capable of atomic resolution because only electrons at the tip's apex are involved in tunneling. Binnig and Rohrer were awarded the 1986 Nobel Prize in Physics for their work with STM.[3, 4]

Even though STM is now widely used in surface science research labs,[5-8] this technique does have some limitations. Only conductive samples can be studied using STM. It is difficult to decouple the change in current due to topography from that due to local variations in electronic properties. Therefore, we opted to use atomic force microscopy (AFM)-based techniques for research presented in this dissertation.

2.3 Atomic Force Microscopy – Imaging Surface Topography

2.3.1 Contact Mode AFM

Atomic force microscopy (AFM) was developed as an analog to STM that could image nanoscale features on nonconductive surfaces. It was first developed in 1986 by Gerd Binnig and Calvin F. Quate.[9] Figure 2.1 shows a schematic of how contact mode AFM operates. A sharp probe tip extends beneath a flexible cantilever attached to a silicon chip. A laser is focused on the end of the cantilever, above the tip's position, and reflects onto a position sensitive photodetector (PSD). The sample is mounted on the scan stage. Then, unlike STM, the probe tip is brought into contact with the surface. As the tip is forced onto the surface, the cantilever bends and moves the laser's position on the PSD. The laser's deflection is used as the feedback loop to track the surface's topography. A piezoelectric scanner moves the sample laterally underneath the tip. A Z-piezoelectric

motor moves the tip up or down depending on the cantilever's deflection thereby generating a picture of the surface's topography. For data in this dissertation, contact AFM images were collected using a Digital Instruments Atomic Force Microscope with a Nanoscope J scanner.

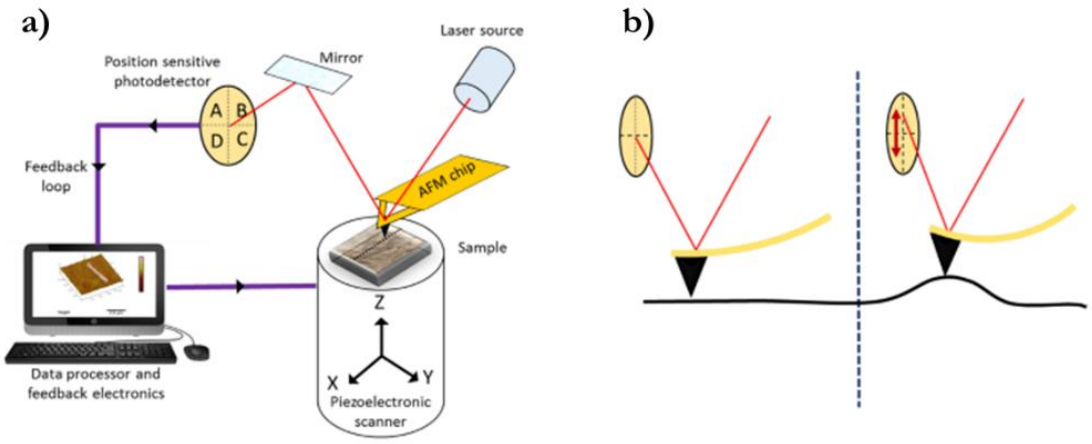

Figure 2.1: Tracking topography with contact mode AFM. (a) Overall layout of the system. Laser is focused onto the end of a flexible cantilever that is reflected onto a position sensitive photodetector (PSD). The sample is moved underneath the AFM tip by the piezoelectric scanner. (b) The topography is mapped by changes in the laser's position on the PSD. This image was originally created by Dr. Sasanka Ulapane[10] and is used with his permission.

The amount of force applied underneath the tip depends on the cantilever's force constant (stiffness) and its deflection. Silicon nitride tips (NP-S) from Bruker were used for contact mode imaging in this work. These cantilevers have a force constant (k) of 0.06 N/m; they are very flexible and unlikely to damage a robust surface. Using stiffer probes such as diamond-like carbon (DLC) tips (k ~40 N/m) can exert enough force to damage a surface. Nanolithography uses stiff AFM probes to intentionally create features on surfaces. This is done routinely in our research lab to selectively pattern areas of self-assembled monolayers.[11, 12] Nanolithography was used for the work presented in Chapter 5 that focuses on patterning salt-based resist layers for metal nanostructure growth.

2.3.2 Tapping Mode AFM

Another way to track surface topography is to use tapping mode AFM, also known as intermittent contact AFM.[6, 7, 13] This technique is useful for imaging soft samples, samples with

weakly adsorbed compounds, or a surface that can be damaged with contact AFM.[14] For this work, tapping AFM images were collected on a Digital Instruments Multimode AFM with a Nanoscope IIIa controller. As with contact AFM, a laser is focused onto the back of a cantilever. A tip extends towards the surface underneath the cantilever. When the probe is far away from the surface, it is oscillated just below its natural resonance frequency. Stiffer cantilevers, compared to those used in contact AFM, are typically used for their relatively large resonance frequencies (> 1 kHz). A higher resonance frequency ensures that a particular location is sampled well before the tip laterally moves to another spot on the surface. For this work, Tap300DLC tips from BudgetSensors were used; these tips have a 300 kHz resonance frequency and a force constant (k) of 40 N/m.

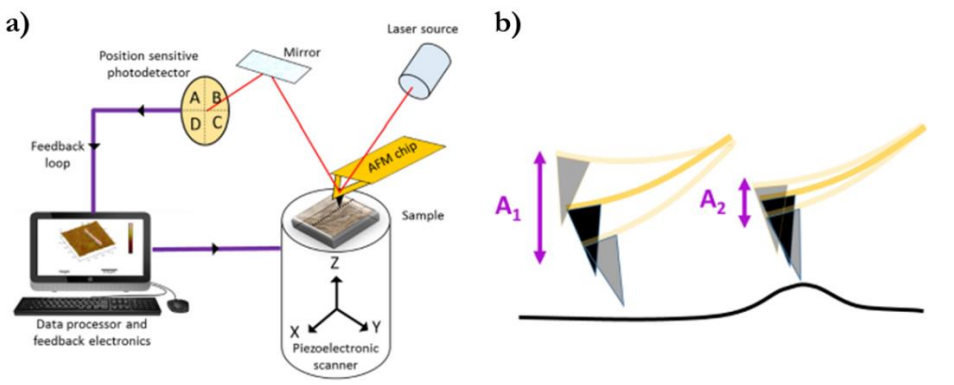

Figure 2.2: Tracking topography with tapping mode AFM. (a) Overall layout of the system. Laser is focused onto the end of a flexible cantilever that is reflected onto a position sensitive photodetector (PSD). The sample is moved underneath the AFM tip by the piezoelectric scanner. (b) The topography is mapped using changes in the tip's oscillation amplitude. The oscillation amplitude is dampened as it intermittently interacts with the surface. This image was originally created by Dr. Sasanka Ulapane[10] and is used with his permission.

Figure 2.2 shows AFM operation in tapping mode. When the tip is far away from the surface, the AFM controller measures the tip's oscillation amplitude at its natural resonance frequency As the tip approaches the surface, its oscillation amplitude is dampened as it begins to feel long-range interactions with the sample. The tip is lowered until it intermittently contacts the surface as it oscillates. The lowering of the tip's oscillation amplitude is used as the feedback loop to monitor surface topography. As with contact mode imaging, the sample is moved laterally underneath the tip and a Z-piezoelectric motor adjusts the tip's height to maintain the feedback

loop. In this work, tapping AFM was used to try to capture images of weakly physisorbed adsorbants on graphite.

2.3.3 Noncontact Atomic Force Microscopy

Noncontact atomic force microscopy (NCAFM)[15] is similar to tapping AFM, except the tip tracks surface topography without ever touching the surface. NCAFM is useful for imaging sensitive samples that are damaged with contact or tapping AFM. In this work, all NCAFM images were collected using a UHV350 AFM/STM with an R9 controller from RHK Technology.[16] This beetle-style microscope, shown in Figure 2.3, was contained within an ultrahigh vacuum (UHV chamber) kept at pressures on the order of 10^{-10} torr. The scan head is lowered to rest on a sample stage, and three piezo legs move the scan head to image the sample. Cantilevers with high resonance frequencies (> 75 kHz) are required for this technique. For this work, NCHPt tips from Nanoworld[17] (k: 40 N/m, f_0: 300 kHz) were used to collect all images. Detailed instructions for operation, maintenance, and troubleshooting this system are included in a separate user manual that is available in the lab.

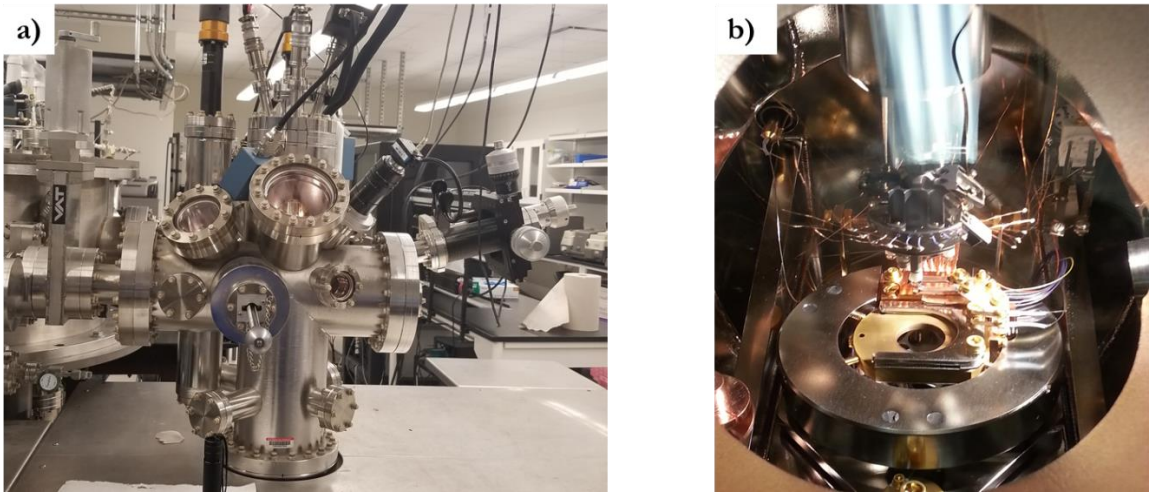

Figure 2.3: RHK UHV350 AFM/STM Instrumentation. (a) UHV chamber that contains scan head. (b) Internal view of sample stage and scan head inside the UHV chamber. The sample is loaded onto the stage and the beetle scan head is lowered onto the sample mount. In this picture, there is no sample loaded onto the stage and the scan head is locked in its storage position.

The tip is oscillated at its natural resonance frequency when far away from the sample. As with tapping AFM, the tip's oscillation is affected when it gets closer to the surface. However, the long-range interactions between the tip and sample are important to this technique as the tip is never brought into contact with the surface. There are two feedback loops that could be used to track surface topography in NCAFM. The microscope can use the amplitude dampening to track the surface topography while keeping the resonance frequency constant; this is known as amplitude modulation noncontact atomic force microscopy (AM-NCAFM). Or, the drop in resonance frequency (while keeping the oscillation amplitude constant) can be used to track the surface topography; this is known as frequency modulation noncontact atomic force microscopy (FM-NCAFM). Both feedback loops adjust the tip's position to maintain the predetermined setpoint from the user. Figure 2.4 illustrates how both feedback modes track surface topography.[18]

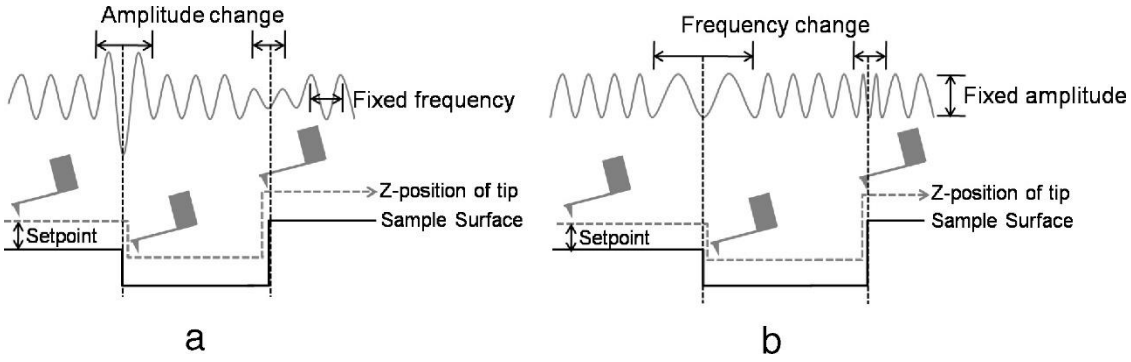

Figure 2.4: Depiction of noncontact atomic force microscopy (NCAFM) in (a) amplitude-modulation and (b) frequency modulation modes. Reprinted with permission from Reference 18. © 2011 Elsevier.

The resolution of this technique is related to the tip's quality factor (Q) during oscillation.[18] The quality factor (Q) is the ratio of the tip's natural resonance frequency (f_0) to the full-width-half-maximum of the resonance frequency's peak (Δf), as shown in Equation 1:

$$Q = \frac{f_0}{\Delta f} \tag{1}$$

While NCAFM can be done in ambient conditions, the quality factor is much higher in vacuum because the ambient air does not dampen the tip's oscillation. Standard, uncoated silicon NCAFM tips can routinely achieve quality factors of, or greater than, 50,000 in vacuum; this is about 500 times larger than their quality factor in air.[18] A larger quality factor essentially means that the resonance peak is sharper. Taking NCAFM images in vacuum increases the resolution and sensitivity due to the larger quality factor, and reduces the presence of surface contamination on the sample.[19] Figure 2.5 shows an example of two resonance peaks with different quality factors at the same resonance frequency.

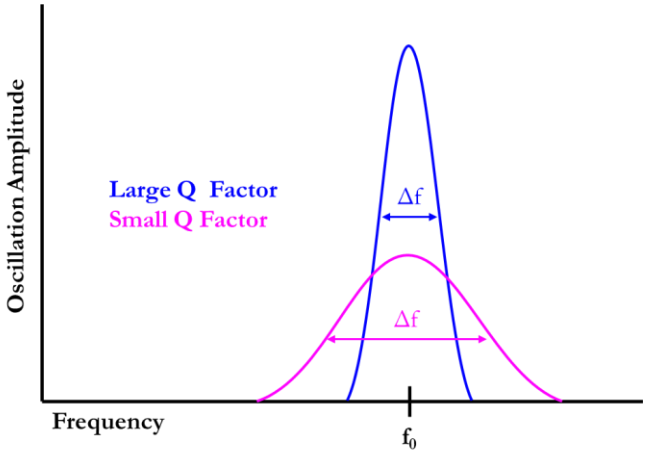

Figure 2.5: Two example resonances centered at the same resonance frequency (f_0). The full width at half maximum (Δf) is labeled for both peaks. The blue curve is like an AFM tip's resonance in vacuum, while the pink curve is similar to ambient conditions.

The microscope's response time for changes in the tip's oscillation amplitude and frequency are different.[18] Equation 2 shows the expression for the timescale of changes in amplitude (τ_{AM}) during AM-NCAFM and Equation 3 shows the equivalent expression for changes in frequency (τ_{FM}) during FM-NCAFM.

$$\tau_{AM} \approx \frac{2Q}{f_0} \tag{2}$$

$$\tau_{FM} \approx \frac{1}{f_0} \tag{3}$$

Both expressions depend on the tip's resonance frequency (f_0), but only τ_{AM} depends on the quality factor (Q). Responses in amplitude modulation become much slower in UHV conditions due to the high quality factor.[20] In UHV conditions, FM-NCAFM allows for higher resolution images taken with faster scan speeds. Therefore, FM-NCAFM was exclusively used in this work.

2.4 Mapping Local Surface Potential with Kelvin Probe Force Microscopy

Atomic force microscopy (AFM), originally used to map surface topography, has been expanded to study other surface properties. Examples of other AFM-based techniques include lateral force microscopy, magnetic force microscopy, and conductive atomic force microscopy. These techniques, and many others, are described in various textbooks.[6, 7, 13, 21] Kelvin probe force microscopy (KPFM), also known as scanning Kelvin probe microscopy (SKPM), is an AFM-based technique that spatially maps the sample's surface potential. KPFM was first used by M. Nonnenmacher in 1991.[22] This technique is integral to work presented in Chapters 3 and 4.

2.4.1 Theory Behind Kelvin Probe Force Microscopy Operation

In ambient conditions, KPFM operates in a "two-pass lift mode".[23] Topography is measured in the first pass over a scan area. Then, the scan head is lifted and traces the previously measured topography while measuring the surface potential.[23] On the other hand, using KPFM in vacuum allows for simultaneous collection of the topography (with NCAFM) and surface potential images in a single pass. Single-pass KPFM was exclusively used in this work. A conductive AFM probe is required for KPFM imaging, but the samples themselves do not need to be conductive. For our work, NCHPt tips from Nanoworld[17] were used. These tips are coated with a conductive PtIr alloy and have a natural resonance frequency around 300 kHz.

KPFM measures the contact potential difference (CPD), also known as the surface potential, between the tip and the sample.[24] The CPD (V_{CPD}) is directly related to a sample's work function[24] and is described by Equation 4:

$$V_{CPD} = \frac{\Phi_{sample} - \Phi_{tip}}{e} \quad (4)$$

Φ_{sample} and Φ_{tip} are work functions for the sample and tip, respectively, and e is the elementary charge of an electron. Scanning the tip over an area allows one to spatially map local changes in the

sample's surface potential which are directly attributed to local work function modifications, assuming the tip's work function remains constant throughout imaging.

As the tip is lowered towards the surface, it experiences a long-range electrostatic force.[18] To measure this electrostatic force (F_{el}), a second feedback loop operates simultaneously with the topography feedback loop (NCAFM). The electrostatic force (F_{el}) is described in Equation 5:

$$F_{el} = \frac{1}{2}\frac{\partial C}{\partial z}[(V_{CPD} - V_{DC}) + V_{AC}\sin(\omega t)]^2 \quad (5)$$

$\frac{\partial C}{\partial z}$ is the gradient of the capacitance as a function of tip-sample distance. An AC bias (V_{ac}) is modulated at frequency ω (separate from the tip's natural resonance frequency used to track topography). The electrostatic force is minimized when an applied DC bias (V_{DC}) is equal to the contact potential difference (V_{CPD}) between the tip and the surface. Applying this DC bias allows one to nullify, and therefore measure, V_{CPD}.

Like NCAFM, KPFM can be operated using amplitude modulation (AM-) or frequency modulation (FM-). AM-KPFM measures the electrostatic force (F_{el}) directly. AM-KPFM requires longer scanning times, as does AM-NCAFM. Furthermore, directly measuring the long-range electrostatic force can convolute tip-sample interactions with sample-cantilever interactions.[18, 25] On the other hand, FM-KPFM detects the gradient of the electrostatic force. This gradient changes the most at the tip's apex, so it eliminates the convolution of longer-range contributions to the electrostatic force.[18, 25] Faster scan times can be implemented with FM-KPFM as well. Our RHK microscope is designed to use "frequency modulation sideband" detection in KPFM.[25] Instead of demodulating the KFPM signal from the topography signal, the KPFM signal is detected on a sideband ($f_0 + \omega$) of the tip's natural resonance frequency (f_0) that is generated when the AC bias is applied (ω).[18]

2.4.2 Uses of Kelvin Probe Force Microscopy in Literature and Our Lab

Although KPFM is not a widespread technique in surface science labs yet, it has been used to spatially map work function variations on surfaces in published literature. Work functions of homogenous scan areas can be measured, so long as the tip's work function has been calibrated using another known material.[26] This KPFM calibration technique has been used to measure the local work functions of self-assembled monolayers (SAMs) chemisorbed to surfaces. Researchers are interested in how the dipole moment of the molecules within the SAM affect the surface's work function. The molecules' dipole moment can be varied by changing the terminal functionality.[27, 28] Michael Zharnikov's research group at Heidelberg University has published several articles using KPFM to track surface potential changes when the placement and orientation of polar functionalities within SAMs are modified.[28-30] Their work changes the terminal functionalities[28], or modifies the placement and orientation of polar pyridine groups within the SAM[29, 30], to change the molecules' dipole moment. The substrate, composition of the monolayer, and the constituent molecule's dipole moment all play a role in modifying the surface's work function. In one publication, Zharnikov's group changed the dipole moment of aromatic molecules that chemisorbed to indium tin oxide (ITO) through phosphonic acid anchoring groups; they were able to modify the surface's work function by as much as 0.5 eV.[29] In another publication, changing the dipole moment of thiol SAMs on gold were able to shift the surface's work function by as much as 1.0 eV.[30]

KPFM has also been applied to heterogeneous surfaces to provide relative information about the differences in surface potential of various features within one scan area. The topography and surface potential of incomplete domains of self-assembled monolayers, hundreds of nanometers in lateral dimensions, have been mapped with KPFM.[31-33] Molecules transition between different orientations (tilted, parallel, disordered) relative to the surface as they self-assemble into monolayers. Different relative KPFM contrast is observed when comparing ordered phases; this is attributed to

changes in the molecules' native dipole moment orientation relative to the surface.[32, 33] Consistent with other published work, the sign and magnitude of the relative KPFM contrast depends on the substrate, monolayer composition, and SAM orientation relative to the surface. Ordered domains of mercaptohexadecanoic acid on gold were measured to have local surface potentials 50 mV more positive than the bare gold substrate.[32] On the other hand, different phases of terphenylthiol monolayers on gold exhibited local surface potentials a few hundred mV different than the bare substrate; the local work function could be increased or decreased depending on the molecules' orientation relative to the surface.[33]

KPFM, in conjunction with topographical mapping, has been applied to correlate surface morphology to measured local work function differences. Topography and surface potential images of crystalline titanium dioxide (TiO_2) show areas of charged, subsurface defects; these charged regions repel adsorbed hydrogen adatoms.[34] Domain boundaries of organic semiconductor thin films, known to inhibit charge transport, show KPFM contrast.[35] KPFM helped identify two predominant domains that form during MgO thin film growth on a silver substrate; each domain exhibited a different relative surface potential contrast (± 50 mV) compared to bare silver. Single layer and bilayer graphene are measured to have different work functions with KPFM.[36]

Environmental effects on surfaces have also been mapped with KPFM. The relative surface potential between palladium nanoparticles (PdNPs) and bare graphite was shown to decrease by 0.5 V over the course of a week inside an ultrahigh vacuum chamber.[37] Because the nanoparticles' shape does not change over this time, the shift in work function is attributed to adsorbed contamination on the surface.[37] Preparing exfoliated graphene on mica in ambient, humid conditions traps water in between the graphene sheet and substrate.[38] Removing the intercalated water from the graphene flake's edges through heating was shown to locally decrease the work function by about 1.0 eV with

KPFM.[38] KPFM has also been used to map the effects of ambient, atmospheric contamination on graphite's local work function.[19]

KPFM has been used to track changes in materials' behavior when exposed to light. The local work function of dye-covered crystalline titanium dioxide (TiO_2) surfaces decreased by 0.14 eV when irradiated with light.[39] This change was attributed to photoinduced electron transfer from the dye to TiO_2 and a change in the dye's dipole moment upon exposure to light.[39] The surface potential of an InN substrate drops when exposed to UV light but recovers once the light is turned off.[40] The InN surface potential dropped between 15 mV – 300 mV, and experienced less of a decrease when exposed to higher intensity light.[40] The local surface potential of an array of gold nanodisks on silicon shifted when exposed to light; this phenomenon is thought to be due to changes in localized plasmons on the nanostructures.[41] KPFM has mapped local surface potentials of bulk organic heterojunctions, of interest for photovoltaics applications, before and after exposure to light.[42]

Because KPFM maps surface potential, it has been used to map charge distribution over relatively large features. Permanent and variable surface charges in domains of clay nanoparticles, often hundreds of nanometers wide, have been mapped with KPFM.[43] Permanent surface charges are attributed to cations from minerals within the clay, while variable charges are attributed to ambient conditions (exposure to water, pH).[43] The surface potential of isolated, bicomponent, p-n junction nanorods adsorbed on graphite has been imaged with KPFM.[44] The ends of these nanorods, 100 nm in total length, exhibited surface potential contrast that was correlated to composition differences within the nanostructure.[44] KPFM was utilized to attempt to map the charge distribution along single, isolated, avidin proteins (58 kDa) and DNA strands adsorbed to silicon.[45] The avidin protein had a surface potential that was 10 mV more positive than the bare silicon substrate, while the DNA strand had a -150 mV relative surface potential.[45] But, detailed

charge distribution within the molecular boundaries was unable to be resolved with KPFM even on these relatively large biomolecules.[45]

The work presented in Chapters 3 and 4 of this dissertation uses KPFM to track local surface potential changes of small, isolated azulene derivatives adsorbed on highly ordered pyrolytic graphite (HOPG). We take KPFM surface potential images, simultaneously with NCAFM topography images, in a single pass using our RHK UHV350 AFM/STM system. Figure 2.6 shows representative topography and surface potential images of freshly cleaved HOPG collected with our RHK microscope. We observe KPFM contrast that correspond to step edges in the topography image, which is consistent with other published KPFM images of graphite.[46] Graphite's external step edges, that are exposed to ambient conditions, are oxidized and chemically distinct from the surrounding terraces (as discussed in Chapter 3).

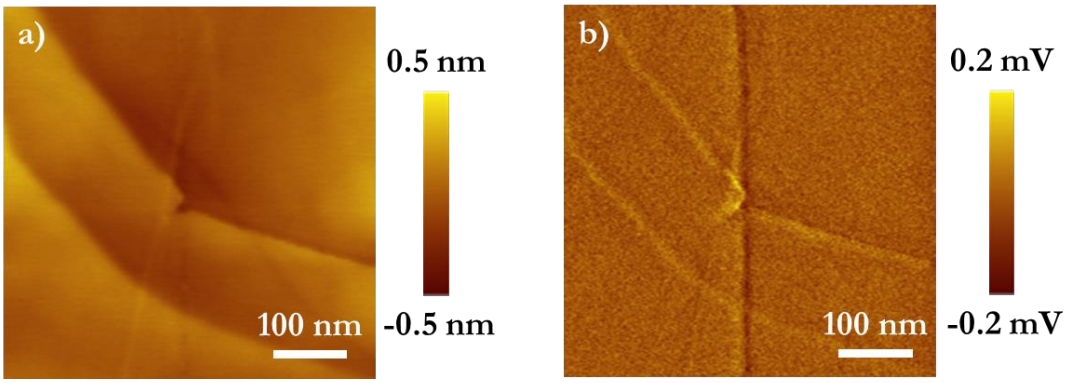

Figure 2.6: Representative images of freshly cleaved highly ordered pyrolytic graphite (HOPG) taken on the RHK UHV SPM system in our lab. (a) 500 nm x 500 nm NCAFM topography image, taken with a 500 nm/s scan rate, and (b) its corresponding surface potential image.

KPFM's utility has been demonstrated in published literature but has been applied to limited circumstances. Either complete, or incomplete domains with lateral dimensions on the order of or greater than 10 nm, of self-assembled monolayers have been mapped with KPFM. In either case, molecules are very densely packed and single molecule effects cannot be resolved. KPFM's use on isolated features has been restricted to relatively large metal nanoparticles (with lateral dimensions 10 – 100s nm) or bulky biomolecules. Furthermore, studies using KPFM to map effects of

systematically controlling the magnitude and direction of local surface potential modifications are limited to chemisorbed systems such as self-assembled monolayers.

The work presented in Chapters 3 and 4 utilized KPFM to locally map a novel dopant-substrate system. The topography and surface potential of isolated azulene-based molecules adsorbed to graphite are imaged. Azulene-based dopants potentially provide a systematic way to locally dope a carbon surface (graphene or graphite) simply through physisorption, rather than chemisorption. Typically, doping effects on carbon substrates (graphene or graphite) are measured with bulk techniques. Here, KPFM is used to locally map how single, isolated physisorbed molecules affect a surface's work function. KPFM provided information about the local doping-substrate interaction site that is currently lacking in literature.

2.5 References

1. Binnig, G.; Rohrer, H.; Gerber, C.; Weibel, E., Tunneling through a controllable vacuum gap. *Applied Physics Letters* **1981,** *40* (2), 178-180.

2. Binnig, G.; Rohrer, H.; Gerber, C.; Weibel, E., 7 x 7 Reconstruction on Si(111) Resolved in Real Space. *Physical Review Letters* **1983,** *50* (2), 120-123.

3. The Nobel Prize in Physics 1986 Press Release. https://www.nobelprize.org/prizes/physics/1986/summary/ (accessed November 19, 2020).

4. Baratoff, A., 1986 Nobel Prizes Development of Scanning Tunnelling Microscopy. *Europhys. News* **1986,** *17* (11-12), 141-144.

5. Chen, C. J., *Introduction to Scanning Tunneling Microscopy*. 2nd ed.; Oxford Science Publications: 2008.

6. Bonnell, D. A., *Scanning Probe Microscopy and Spectroscopy Theory, Techniques, and Applications*. 2nd ed.; Wiley-VCH: New York, 2001.

7. Wiesendanger, R., *Scanning Probe Microscopy and Spectroscopy: Methods and Applications*. Cambridge University Press: Cambridge, 1994.

8. Moore, A. M.; Weiss, P. S., Functional and Spectroscopic Measurements with Scanning Tunneling Microscopy. *Annual Review of Analytical Chemistry* **2008,** *1* (1), 857-882.

9. Binnig, G.; Quate, C. F.; Gerber, C., Atomic Force Microscope. *Physical Review Letters* **1986,** *56* (9), 930-933.

10. Ulapane, S. B. Harnessing the Control of Metallic Nanostructures on Interfaces Towards Biosensing, Plasmonics and More. Ph.D. Dissertation, University of Kansas, Lawrence, KS, 2019.

11. Headrick, J. E.; Armstrong, M.; Cratty, J.; Hammond, S.; Sheriff, B. A.; Berrie, C. L., Nanoscale Patterning of Alkyl Monolayers on Silicon Using the Atomic Force Microscope. *Langmuir* **2005,** *21* (9), 4117-4122.

12. Edwards, C. M.; Ulapane, S. B.; Kamathewatta, N. J. B.; Ashberry, H. M.; Berrie, C. L., Fabrication and Growth Control of Metal Nanostructures through Exploration of Atomic Force Microscopy-Based Patterning and Electroless Deposition Conditions. *The Journal of Physical Chemistry C* **2020**.

13. Eaton, P. W., Paul, *Atomic Force Microscopy*. Oxford University Press: New York, 2010.

14. Möller, C.; Allen, M.; Elings, V.; Engel, A.; Müller, D. J., Tapping-Mode Atomic Force Microscopy Produces Faithful High-Resolution Images of Protein Surfaces. *Biophysical Journal* **1999,** *77* (2), 1150-1158.

15. Morita, S.; Wiesendanger, R.; Meyer, E., *Noncontact Atomic Force Microscopy*. Springer: New York, 2002.

16. RHK Technology. https://www.rhk-tech.com/ (accessed November 19, 2020).

17. Nanoworld NCHPt AFM Tips. https://www.nanoworld.com/pointprobe-tapping-mode-platinum-coated-afm-tip-nchpt (accessed November 19, 2020).

18. Melitz, W.; Shen, J.; Kummel, A. C.; Lee, S., Kelvin probe force microscopy and its application. *Surface Science Reports* **2011,** *66* (1), 1-27.

19. Martinez-Martin, D.; Longuinhos, R.; Izquierdo, J. G.; Marele, A.; Alexandre, S. S.; Jaafar, M.; Gómez-Rodríguez, J. M.; Bañares, L.; Soler, J. M.; Gomez-Herrero, J., Atmospheric contaminants on graphitic surfaces. *Carbon* **2013,** *61*, 33-39.

20. Albrecht, T. R.; Grutter, P.; Horne, D.; Rugar, D., Frequency Modulation Detection Using High-Q Cantilevers for Enhanced Microscope Sensitivity. *Journal of Applied Physics* **1991,** *69* (2), 668-673.

21. Samori, P., *Scanning Probe Microscopies Beyond Imaging Manipulation of Molecules and Nanostructures*. Wiley-VCH: Weinheim, 2006.

22. Nonnenmacher, M.; O'Boyle, M. P.; Wickramasinghe, H. K., Kelvin probe force microscopy. *Applied Physics Letters* **1991,** *58* (25), 2921-2923.

23. Li, G.; Mao, B.; Lan, F.; Liu, L., Practical aspects of single-pass scan Kelvin probe force microscopy. *Review of Scientific Instruments* **2012,** *83* (11), 113701.

24. Glatzel, T.; Lux-Steiner, M. C.; Strassburg, E.; Boag, A.; Rosenwaks, Y., Principles of Kelvin Probe Force Microscopy. In *Scanning Probe Microscopy: Electrical and Electromechanical Phenomena at the Nanoscale*, Kalinin, S.; Gruverman, A., Eds. Springer New York: New York, NY, 2007; pp 113-131.

25. Milde, P.; Porthun, S., Kelvin Probe Force Microscopy with the RHK R9. RHK Technology Inc.: https://www.rhk-tech.com/applications/appnotes/, 2016.

26. Garrillo, P. A. F.; Grévin, B.; Chevalier, N.; Borowik, Ł., Calibrated work function mapping by Kelvin probe force microscopy. *Review of Scientific Instruments* **2018,** *89* (4), 043702.

27. Szwajca, A.; Wei, J.; Schukfeh, M. I.; Tornow, M., Self-assembled monolayers of alkyl-thiols on InAs: A Kelvin probe force microscopy study. *Surface Science* **2015,** *633*, 53-59.

28. Sauter, E.; Yildirim, C.; Terfort, A.; Zharnikov, M., Adjustment of the Work Function of Pyridine and Pyrimidine Substituted Aromatic Self-Assembled Monolayers by Electron Irradiation. *The Journal of Physical Chemistry C* **2017,** *121* (23), 12834-12841.

29. Asyuda, A.; Gärtner, M.; Wan, X.; Burkhart, I.; Saßmannshausen, T.; Terfort, A.; Zharnikov, M., Self-Assembled Monolayers with Embedded Dipole Moments for Work Function Engineering of Oxide Substrates. *The Journal of Physical Chemistry C* **2020,** *124* (16), 8775-8785.

30. Gärtner, M.; Sauter, E.; Nascimbeni, G.; Wiesner, A.; Kind, M.; Werner, P.; Schuch, C.; Abu-Husein, T.; Asyuda, A.; Bats, J. W.; Bolte, M.; Zojer, E.; Terfort, A.; Zharnikov, M., Self-Assembled Monolayers with Distributed Dipole Moments Originating from Bipyrimidine Units. *The Journal of Physical Chemistry C* **2020,** *124* (1), 504-519.

31. Zerweck, U.; Loppacher, C.; Otto, T.; Grafström, S.; Eng, L. M., Kelvin probe force microscopy of C60 on metal substrates: towards molecular resolution. *Nanotechnology* **2007,** *18* (8), 084006.

32. Campiglio, P.; Campione, M.; Sassella, A., Kelvin Probe Force Microscopy Characterization of Self-Assembled Monolayers on Metals Deposited with Dip-Pen Nanolithography. *The Journal of Physical Chemistry C* **2009,** *113* (19), 8329-8335.

33. Biere, N.; Koch, S.; Stohmann, P.; Walhorn, V.; Gölzhäuser, A.; Anselmetti, D., Resolving the 3D Orientation of Terphenylthiol Molecules on Noble Metals with Kelvin Probe Force Microscopy. *The Journal of Physical Chemistry C* **2019,** *123* (32), 19659-19667.

34. Onoda, J.; Pang, C. L.; Yurtsever, A.; Sugimoto, Y., Subsurface Charge Repulsion of Adsorbed H-Adatoms on TiO2(110). *The Journal of Physical Chemistry C* **2014,** *118* (25), 13674-13679.

35. Qian, C.; Sun, J.; Zhang, L.; Huang, H.; Yang, J.; Gao, Y., Crystal-Domain Orientation and Boundary in Highly Ordered Organic Semiconductor Thin Film. *The Journal of Physical Chemistry C* **2015,** *119* (27), 14965-14971.

36. Panchal, V.; Pearce, R.; Yakimova, R.; Tzalenchuk, A.; Kazakova, O., Standardization of surface potential measurements of graphene domains. *Scientific Reports* **2013,** *3*, 2597.

37. Palacios-Lidón, E.; Henry, C. R.; Barth, C., Kelvin Probe Force Microscopy in Surface Chemistry: Reactivity of Pd Nanoparticles on Highly Oriented Pirolytic Graphite. *ACS Catalysis* **2014,** *4* (6), 1838-1844.

38. Ochedowski, O.; Bussmann, B. K.; Schleberger, M., Graphene on Mica - Intercalated Water Trapped for Life. *Scientific Reports* **2014,** *4*, 6003.

39. Ikeda, M.; Koide, N.; Han, L.; Sasahara, A.; Onishi, H., Work Function on Dye-Adsorbed TiO_2 Surfaces Measured by Using a Kelvin Probe Force Microscope. *Journal of Physical Chemistry C* **2008,** *112* (17), 6961-6967.

40. Sun, X.; Wei, J.; Wang, X.; Wang, P.; Li, S.; Waag, A.; Li, M.; Zhang, J.; Ge, W.; Shen, B., Anomalous surface potential behavior observed in InN by photoassisted Kelvin probe force microscopy. *Applied Physics Letters* **2017,** *110* (22), 222103.

41. Ezaki, T.; Matsutani, A.; Nishioka, K.; Shoji, D.; Sato, M.; Okamoto, T.; Isobe, T.; Nakajima, A.; Matsushita, S., Surface potential on gold nanodisc arrays fabricated on silicon under light irradiation. *Surface Science* **2018,** *672-673*, 62-67.

42. Spadafora, E. J.; Demadrille, R.; Ratier, B.; Grévin, B., Imaging the Carrier Photogeneration in Nanoscale Phase Segregated Organic Heterojunctions by Kelvin Probe Force Microscopy. *Nano Letters* **2010,** *10* (9), 3337-3342.

43. Liu, J.; Gaikwad, R.; Hande, A.; Das, S.; Thundat, T., Mapping and Quantifying Surface Charges on Clay Nanoparticles. *Langmuir* **2015,** *31* (38), 10469-10476.

44. Nanayakkara, S. U.; Cohen, G.; Jiang, C.-S.; Romero, M. J.; Maturova, K.; Al-Jassim, M.; van de Lagemaat, J.; Rosenwaks, Y.; Luther, J. M., Built-in Potential and Charge Distribution within Single Heterostructured Nanorods Measured by Scanning Kelvin Probe Microscopy. *Nano Letters* **2013,** *13* (3), 1278-1284.

45. Leung, C.; Kinns, H.; Hoogenboom, B. W.; Howorka, S.; Mesquida, P., Imaging Surface Charges of Individual Biomolecules. *Nano Letters* **2009,** *9* (7), 2769-2773.

46. Lee, H.; Lee, H.-B.-R.; Kwon, S.; Salmeron, M.; Park, J. Y., Internal and External Atomic Steps in Graphite Exhibit Dramatically Different Physical and Chemical Properties. *ACS Nano* **2015,** *9* (4), 3814-3819.

Chapter 3: The Effect of Azulene on the Local Work Function of Graphite – Baseline Behavior for a Novel, Tunable Dopant

3.1 Abstract

Graphene is the subject of a large research initiative to develop it for applications in photovoltaics, batteries, catalysis, and sensors. In most cases, graphene's electronic properties need to be modified to fit a particular application. Although doping of graphene is widely known to occur, most doping studies are bulk measurements. In order to tailor adsorbants to control the local doping effect, a more local, fundamental understanding of how doping occurs at the interaction site is required. We propose using azulene-based molecules as dopants for graphene because azulene is a planar, conjugated molecule that can π-stack with the graphene lattice and it has independently tunable frontier molecular orbitals. This chapter focuses on optimizing deposition conditions for such molecules and obtaining a baseline knowledge of azulene's behavior on the surface. For all experiments, highly ordered pyrolytic graphite (HOPG) was used as a substitute for graphene. Graphene and graphite have similar chemical and electronic properties, but graphite substrates are more consistent and reproducible. Using graphite allowed for reliable comparisons of molecules' behavior between different samples. Noncontact atomic force microscopy (NCAFM) and Kelvin probe force microscopy (KPFM) were used simultaneously to map topography and surface potential distributions of azulene and naphthalene on graphite.

Solvent deposition proved to be unsuitable for coating graphite in azulene because it promoted azulene diffusion across the surface, so molecules primarily adsorbed to graphite's step edges. The graphite substrates also sustained damage after extended exposure to the dichloromethane solvent. This method also carried a higher risk of depositing contamination on the surface. Therefore, we used vapor deposition to coat graphite substrates in azulene molecules. While molecules still preferentially adsorbed to the step edges, more isolated molecules were found on the

terraces. Topography cross-sectional analysis found that single molecules had heights consistent with graphite's interlayer spacing, suggesting that azulene and naphthalene π-stack flat against the graphite lattice. The measured lateral dimensions of single molecules were an order of magnitude larger than their true size, due to convolution with the broad AFM tip.

For isolated molecules on graphite's terraces, p-type doping behavior was observed for both azulene and naphthalene; azulene had a greater p-type effect on the local surface potential than naphthalene. While the integer charge transfer model predicts this p-type doping behavior for azulene, it is inconsistent with naphthalene's observed effect on the surface potential. This suggests that charge transfer might not be the only way azulene dopes graphite. The local doping effect on graphite did not extend beyond where the dopant was adsorbed on the surface.

Clusters containing multiple molecules were also found on the surface. Their topography varied from cluster to cluster, but their effect on the surface potential was consistent with the single molecules. Further work is needed to expand our understanding of this doping behavior. This work is continued in Chapter 4, where substituted azulenes deposited on graphite are imaged with NCAFM and KPFM.

3.2 Introduction

3.2.1 Comparisons Between Graphite and Graphene

Ultimately, we are interested in quantifying the effect that isolated, physisorbed organic molecules have on graphene's local work function. Graphene samples are time-consuming to prepare while having reproducibility issues, as discussed in Chapter 1. Highly ordered pyrolytic graphite (HOPG) was used instead of graphene for studies presented in this work. HOPG and graphene have very similar properties. Furthermore, HOPG substrates are easily regenerated by mechanical cleaving and their surfaces are more consistent than graphene samples. HOPG

substrates were used to efficiently optimize deposition methods for these organic molecules while also providing a consistent substrate to compare adsorbants' behavior on the surface. Only HOPG was used in these experiments, therefore the terms "graphite" and HOPG are used interchangeably in this dissertation. This section compares graphene and graphite's properties.

HOPG is an ordered, layered material composed of stacked graphene sheets. Each layer is a planar, two-dimensional sheet of sp^2 hybridized carbon atoms arranged in an hexagonal pattern.[1, 2] Figure 3.1 illustrates the intra- and inter-layer structures of sheets in HOPG. Intralayer carbon atoms are covalently bound with a carbon-carbon bond distance of 1.42 Å.[1] Layers stack on top of each other in an AB pattern and are held together with relatively weak van der Waals interactions.[1] The interlayer spacing in HOPG is 0.34 nm.[1] The literature convention for axis labeling in HOPG is also shown in Figure 3.1. The "a" and "b" axes are within the plane of a single sheet, while the "c" axis is oriented perpendicular to the plane.[1, 2]

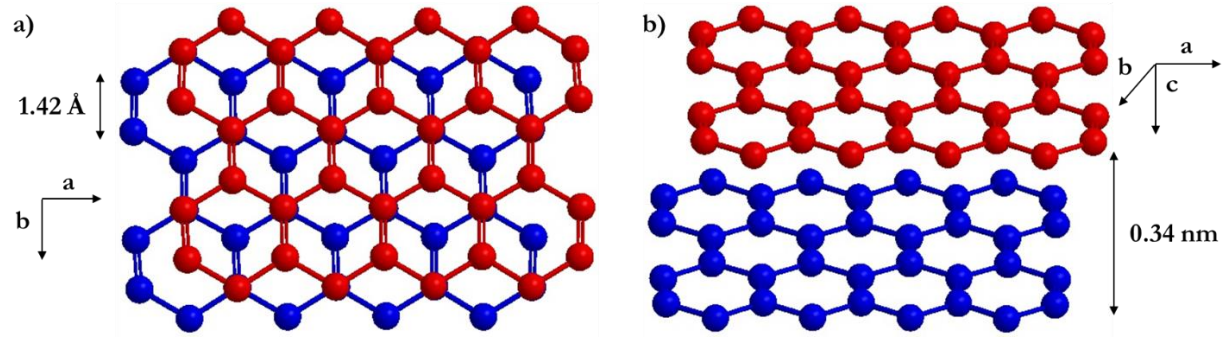

Figure 3.1: Relative positions of stacked layers in HOPG with axes orientations. (a) Top-down view of AB stacking pattern. The intralayer carbon-carbon bond distance is labeled. (b) Side view of sheets, with the interlayer distance labeled.

HOPG is a synthetic material that is formed by decomposing hydrocarbon gas at 2000 °C, then annealed by hot pressing the substrate at a temperature between 2800 – 3000 °C using an applied pressure between 300 – 500 kg/cm^2.[1] The resulting HOPG sample is very ordered. Individual grains along the "a" axis can be greater than or equal to 10,000 Å in length in HOPG, which is much more ordered than naturally-occurring graphite.[2] The quality of HOPG samples is

determined by their mosaic spread, also known as mosaic angle.[3] The mosaic angle is defined as the full width at half maximum (FWHM) angular dispersion of the c-axis; this describes how parallel the sheets are to each other.[3, 4] This value generally ranges from 0.3 – 5.0°, with higher quality samples having lower mosaic angles.[4, 5] HOPG substrates with lower mosaic angles have larger surface grains with fewer defect sites and step edges. HOPG samples are commercially available in a wide range of lateral dimensions and thicknesses, depending on the user's requirements. Square samples typically have areas between 7 x 7 mm^2 – 2 x 2 cm^2; circular samples are also available for purchase.[5, 6] The thickness of HOPG substrates ranges from 0.7 – 2 mm, so a single sample can be cleaved and used for many experiments.[5, 6]

Within a layer, each carbon atom has a $2p_z$ atomic orbital that is not involved in intralayer bonding.[1] These atomic orbitals overlap in a side-on fashion, allowing delocalized π-electrons to flow across the layer. Monolayer graphene has a low resistivity, although there are discrepancies on the exact value. Some sources report a resistivity between 1.0 x 10^{-6} – 3.0 x 10^{-6} (Ω·cm) for graphene supported on a silicon substrate with a native oxide layer (SiO_2).[7, 8] A different source quotes graphene's resistivity to be on the order of 10^{-4} (Ω·cm).[9] One must be careful to consider that the supporting substrate, environmental conditions, and preparation method can have a significant effect on experimental results for this atomically thin material.[7, 8] Graphite is also conductive, although its conductivity is different depending on the reference axis. The resistivity of HOPG across the carbon plane is very low (along a- or b-axis), 4 x 10^{-5} Ω cm.[2] The poor interplanar orbital overlap in graphite results in much lower conductivity and higher resistivity perpendicular to the carbon sheets (along c-axis), 0.17 Ω cm.[2] Along the carbon plane, both graphite and graphene are considered conductive.

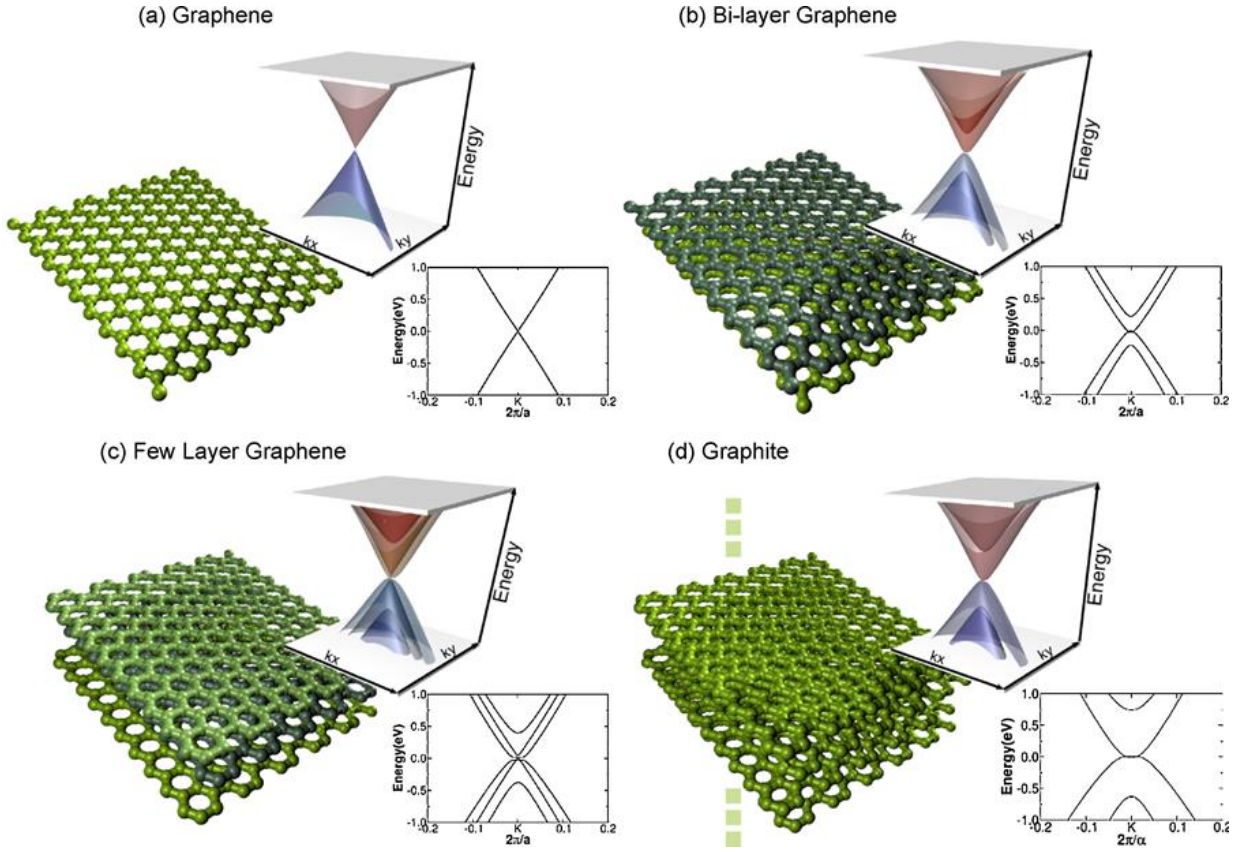

Figure 3.2: Density functional theory (DFT) evolution of electronic band structure at Dirac point from (a) graphene to (d) bulk graphite, as more graphene layers are stacked. The Fermi level has been set at zero in all diagrams. Reprinted with permission from Reference 10. © 2010 Elsevier.

Graphene and graphite also have very similar electronic band structures. Figure 3.2 shows the evolution of the electronic band structure around the Dirac point of graphene to bulk graphite, as more layers are stacked, obtained from theoretical DFT calculations.[10] Two-dimensional cross sections of graphene's valence and conduction bands are shaped like sharp "V"s.[10] As discussed in Chapter 1, graphene is known as a "zero bandgap" semiconductor because the valence and conduction bands meet but do not overlap in energy at the Dirac point.[10-12] The electronic bands' shape becomes more parabolic as more layers are stacked.[10] In bulk graphite, the valence and conduction band have a very small overlap between 0.03 – 0.04 eV.[1, 13] Therefore, graphite is considered a semimetal. The work function of this material also slightly changes as more carbon layers are stacked. While there is spread in reported literature values, graphite's work function (4.6 –

4.8 eV)[14-17] is generally reported to be somewhat larger than graphene's work function (4.5 - 4.6 eV)[17-21]. As mentioned earlier, one must exercise caution when comparing experimental results for graphene because it is such a thin material. The supporting substrate[22] or additional metal contacts for conductivity studies[23] can modify graphene's work function. Graphene and bulk graphite have similar electronic properties, but graphite substrates are more reliable and consistent.

The weak interlayer interaction means that graphite layers can be easily separated with mechanical force. Graphite is commonly used in pencils where layers slough off during writing, leaving markings on paper. Graphite is also a common commercial lubricant used to loosen locks because the weakly interacting carbon layers can slip past each other. HOPG can be cleanly cleaved using scotch tape to peel away an old, exposed surface.[24] Andre Geim and Konstantin Novoselov were the first to use this technique to isolate graphene from a bulk graphite substrate. They were awarded the 2010 Nobel Prize in Physics for their work isolating and characterizing graphene.[25] Figure 3.3(a) shows a representative noncontact atomic force microscopy (NCAFM) image of a freshly cleaved HOPG surface.

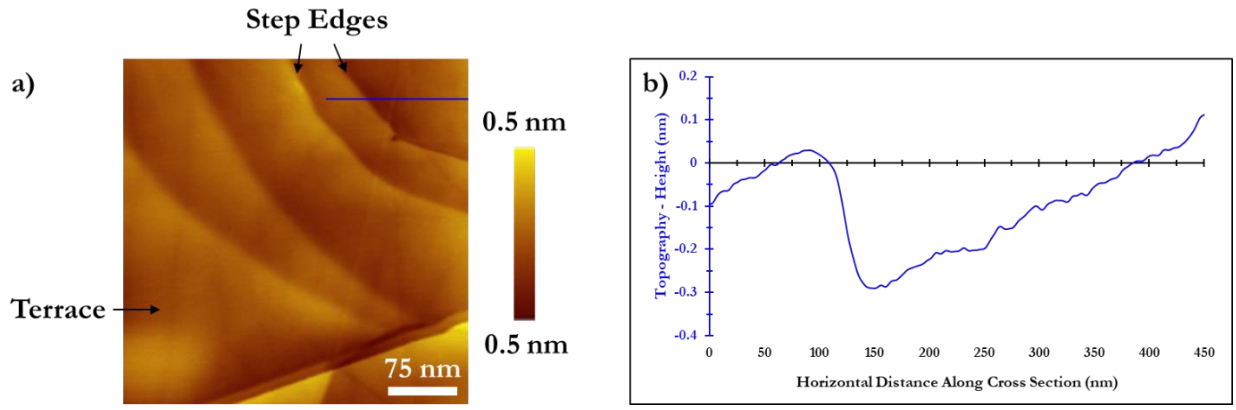

Figure 3.3: Representative NCAFM topography image of HOPG. (a) 1.0 µm x 1.0 µm image, taken with a 1.0 µm/s scan rate. (b) Cross section through the blue line in (a).

The surface is predominantly flat and pristine. These flat areas are graphite's basal planes[2], also known as terraces. The terraces are chemically inert. It should be noted that the graphite does not cleave evenly; multiple layers cleave off at once and tear during the process. These defects, known as

step edges, are visible in Figure 3.3(a). The spacing between two terraces, using Figure 3.3(b)'s cross section over a step edge, was measured to be 0.34 nm. Our result is consistent with literature values for graphite's interlayer spacing.[1, 2] It is not uncommon to see step edges larger than 0.34 nm, if multiple layers are cleaved at a particular location.

Graphite's external (exposed to ambient conditions) step edges are considered defect sites. Breaking the covalent carbon-carbon bonds at the step edges leaves dangling bonds that are free to react with water[26] and oxygen in the atmosphere, forming carbonyl[2, 27-29], carboxylic, hydroxyl[30, 31], and alkyl functionalities. Atmospheric contaminants have also been shown to interfere with graphite surface potential experiments conducted in ambient conditions.[32] Internal step edges are grain boundaries formed during HOPG manufacturing. Because they are not exposed to atmosphere, internal step edges are chemically identical to the graphite terraces.[33] By conducting experiments in ultrahigh vacuum (UHV), it is assumed that any lightly bound material from the ambient environment desorbs off the surface. Although the chemically modified, external graphite step edges would still be oxidized.

HOPG is commercially available, relatively inexpensive, and a more consistent substrate than graphene. Graphite is composed of stacked graphene layers, and its terraces are chemically identical to graphene. The edges of a graphene sheet, when exposed to air, will also be oxidized like graphite's step edges. Graphite's surface can be easily and cleanly regenerated by cleaving with scotch tape. On the other hand, growing graphene samples is time-consuming and increases the contamination risk from sample preparation and transfer. Graphite and graphene share similar electronic properties, but graphene's properties are susceptible to influence from the supporting substrate because it is an atomically thin material. Graphite always has a uniform support underneath the topmost layers. Therefore, we opted to use HOPG as a model for studying azulene's interactions

with graphene in this work. Using HOPG allowed us to consistently and reproducibly compare different dopants' behavior on the surface.

3.2.2 Azulene and Naphthalene

As discussed in Chapter 1, we are interested in studying dopants that can physisorb to the graphene (or graphite) lattice. Such molecules can interact with the substrate without breaking its native conductivity. Azulene-based compounds are a unique family of molecules that could π-stack with the graphene (or graphite), while providing some control over the interaction. Figure 3.4 shows the structure, highest occupied molecular orbital (HOMO), and lowest unoccupied molecular orbital (LUMO) for azulene and its structural isomer, naphthalene.

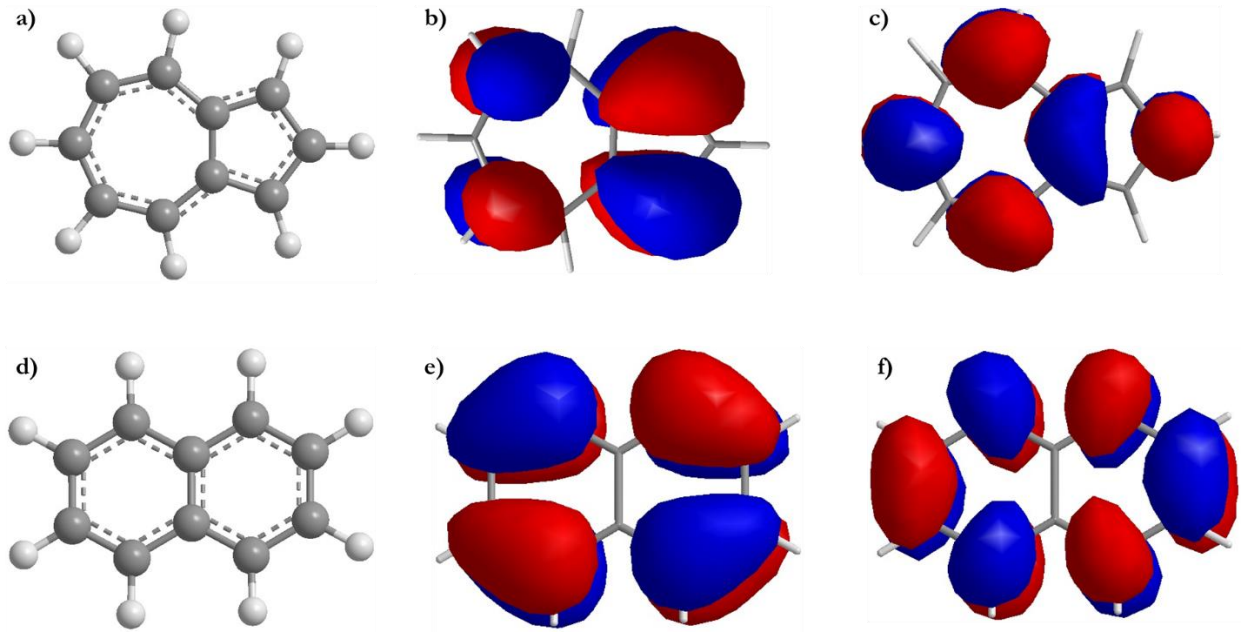

Figure 3.4: Structure and frontier molecular orbitals of structural isomers. Azulene's (a) structure, (b) HOMO, and (c) LUMO. Naphthalene's (d) structure, (e) HOMO, and (f) LUMO.

Both azulene and naphthalene have the chemical formula $C_{10}H_8$, so they are structural isomers. Their atom arrangement causes some drastic differences in molecular properties. Naphthalene is a completely symmetric, nonpolar molecule. Azulene is a fused 5- and 7-membered ring system that has a native dipole moment of about 1.0 Debye.[34] The frontier molecular orbitals of

azulene, as shown in Figures 3.4(b) and (c), are complimentary to each other. Because these orbitals don't occupy the same space along the carbon backbone there is less repulsion between them; this results in a relatively small energy gap between the HOMO and LUMO. Azulene is a blue compound and absorbs in the visible region of the electromagnetic spectrum.[35] Naphthalene's frontier molecular orbitals, however, occupy the same space along its carbon backbone and experience more repulsion. This forces naphthalene's frontier orbitals farther apart in energy than azulene[35]; naphthalene is a white compound that absorbs in the ultraviolet region of the electromagnetic spectrum.[36]

Both azulene and naphthalene are conjugated, planar molecules that could π-stack to the graphene (or graphite) lattice. Azulene-based derivatives are of particular interest because azulene's HOMO-LUMO gap can be independently tuned based upon the location and type of substituent on the azulene ring.[37] Therefore, one could potentially tune the interaction with the graphene (or graphite) lattice. This is investigated more in Chapter 4. Naphthalene's carbon backbone matches the graphene (or graphite) lattice, so it is a good control molecule for comparison with azulene.

3.2.3 Objectives

This chapter focuses on analyzing azulene and naphthalene adsorbed on an HOPG substrate. First, the deposition method for depositing azulene was optimized. Noncontact atomic force microscopy (NCAFM) was performed in an ultrahigh vacuum chamber to map the topography and surface coverage of these molecules. Do the molecules adsorb on a preferential location on the surface? Are we able to resolve the orientation of the adsorbed molecules relative to the surface? Do they π-stack against the graphite lattice, or in some other configuration? Topographical cross sections were used to identify isolated molecules. Kelvin probe force microscopy (KPFM) was performed simultaneously with NCAFM to map the relative effects of these isolated molecules on graphite's local surface potential. Cross-sectional analysis was used to

quantify the local, relative effect on the surface potential, as well as to determine the lateral dimensions of the doping effect. Do we observe a contrast change in the local surface potential where molecules are adsorbed? If so, is this doping effect confined to, or extend beyond, the domains of the adsorbate? Are we able to conclude anything about the mechanism by which these molecules dope graphite?

3.3 Materials and Methods

3.3.1 Materials

A 7 x 7 mm^2 piece of single-sided highly ordered pyrolytic graphite (HOPG) was used as a substrate throughout all experiments (ZYB Grade, from K-Tek Nanotechnology). The HOPG surface was cleanly cleaved before each experiment using the Scotch tape method[24]. Large, upturned graphite flakes were peeled off the surface with tweezers. Sparsely cleaved substrates were not used in order to minimize unwanted surface contamination from the tape or previous experiments.

Azulene was synthesized and provided by the Barybin research group[38] here at the University of Kansas. Naphthalene was also provided from the Barybin group. The Barybin group verified the compounds' purity with nuclear magnetic resonance (NMR) analysis.

3.3.2 Dropcasting Azulene from Solution onto Graphite Surface

Two solvents were used to deposit azulene onto a graphite surface: hexanes and dichloromethane (methylene chloride). Both solvents were purchased from Fisher Scientific and used without further purification. Only clean glass utensils were used with dichloromethane to avoid introducing organic contamination from plastics.

A 0.5 mM solution of azulene in dichloromethane and a 3.0 mM solution of azulene in hexanes were prepared. A 50 μL glass syringe was used to deposit a few drops of the azulene solution onto the freshly cleaved graphite surface; enough solution was deposited to cover the entire

HOPG surface without spilling over the edges (a few μL). A gentle stream of $N_2(g)$ was used to speed up the solvent's evaporation. Samples were immediately transferred into an ultrahigh vacuum (UHV) chamber.

3.3.3 Vapor Deposition of Azulene and Naphthalene onto Graphite Surface

A clean graphite substrate was placed inside a round bottom vacuum flask, along with crystals of the molecule of interest. A picture of this setup is shown in Figure 3.5. A house vacuum line pumped on the flask for 5 – 10 minutes. Then, the flask was sealed and the vacuum line disconnected. An area of the flask that had crystals was locally heated using a heat gun, causing the molecules to sublime. In the case of azulene, a dark blue solid, a blue vapor filled the flask. The inside of the flask appeared slightly cloudy as naphthalene sublimed, because naphthalene is a white compound. As the vapor cooled, crystals would coat the inside of the flask including the HOPG substrate. The flask cooled to room temperature, and then was gently opened to atmospheric pressure. Samples were immediately transferred into an ultrahigh vacuum (UHV) chamber.

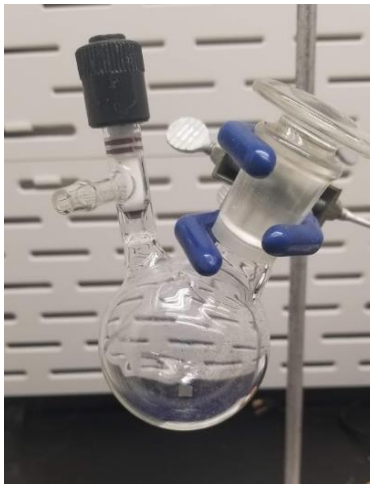

Figure 3.5: Round bottom vacuum flask used for vapor deposition. Dark blue azulene crystals coat the inside of the flask, while the graphite substrate is visible at the bottom.

3.3.4 Noncontact Atomic Force Microscopy (NCAFM) and Kelvin Probe Force Microscopy (KFPM)

A UHV350 AFM/STM with an R9 controller from RHK Technology[39] was used to simultaneously collect NCAFM topography and KPFM surface potential images. The microscope was contained within an ultra-high vacuum (UHV) chamber at a pressure on the order of 10^{-10} torr. NCHPt tips from NanoWorld[40] were used to collect all images. These tips have a 300 kHz

resonance frequency and are coated with a conductive PtIr alloy. The same tip was not used to collect all images. Images were collected at room temperature (~ 22.5 °C).

NCAFM, operating in frequency modulation mode, was used to collect topography images. The shift in resonance frequency (dF) was used as the feedback loop to track the surface's topography. A dF setpoint of -10.0 Hz was generally used throughout all experiments. Scan rates varied from image to image, but were generally in the range of 0.25 – 1.0 μm/s. While the same NCHPt tip was not used to collect all images, the tips' oscillation amplitude was generally set to 50 mV across all experiments.

KPFM, operating in frequency modulation sideband mode[41], was used to collect surface potential images. The KPFM signal was detected 20.0 kHz away from the tip's natural resonance frequency with an applied bias modulation amplitude of 0.5 V.

Generally, all images for a sample were collected over a 48-hour period after the sample was first transferred into the UHV chamber. Samples were not imaged more than one week past their preparation date. Multiple samples were prepared and imaged for each dopant molecule. At least three locations were imaged on each sample. Results from images that had isolated adsorbants were combined into the collective data presented in the next section. All raw topography and surface potential images were x-slope corrected, background zeroed, and smoothed after collection. Cross-sectional analysis of surface features was not corrected for tip convolution.

3.4 Results and Discussion

3.4.1 Surface Distribution of Azulene Molecules from Solvent Deposition

Figure 3.6 shows representative NCAFM topography images of azulene on a graphite surface, where the azulene was deposited by solution dropcasting. Bright yellow dots in the images

indicate the presence of azulene particles. These particles could either be single molecules or clusters, depending on their dimensions.

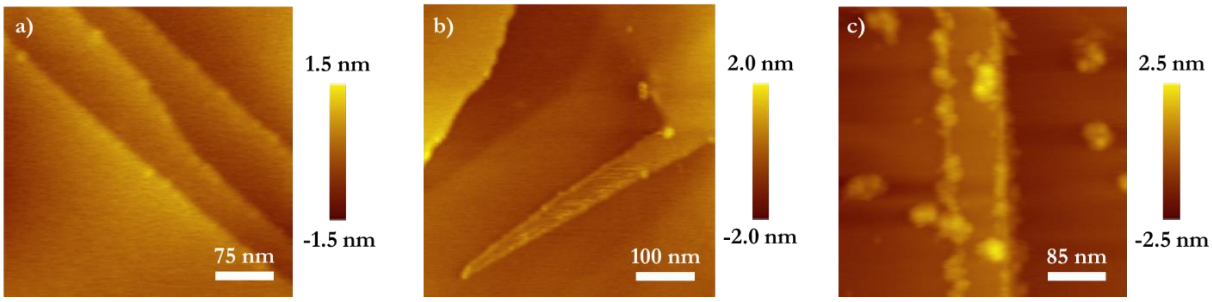

Figure 3.6: Representative NCAFM topography images of azulene on graphite, prepared via solution dropcasting. (a) 375 nm x 375 nm image, taken with a scan rate of 0.63 μm/s, dropcast from a 3.0 mM solution of azulene in hexanes. (b) 500 nm x 500 nm image, taken with a scan rate of 0.67 μm/s, and (c) 425 nm x 425 nm image, taken with a scan rate of 0.57 μm/s. Both samples shown in (b) and (c) were prepared from a 0.5 mM solution of azulene in dichloromethane.

The surface coverage of azulene varies greatly from location to location. Figure 3.6(a) shows low azulene surface coverage. Isolated particles are located along the graphite step edges, but the terraces are completely clean. Figure 3.6(b) has a medium amount of azulene coverage. Some larger clusters are visible, with a couple of isolated particles present on the terraces. Figure 3.6(c) has a relatively high azulene coverage. The graphite step edges are completely coated in azulene. There are several large clusters, along with some isolated particles, on the terraces.

In each image, azulene primarily adsorbs to the graphite step edges. This is typical of other adsorbates on graphite because the particles are energetically stabilized at the step edges. Other researchers have shown that gold[42] and titanium dioxide (TiO_2)[43] nanoparticles prefer to adsorb to graphite step edges. As the solvent evaporates, azulene can diffuse across the graphite surface until it adsorbs at the ideal location. Across tens of similar experiments, very few isolated azulene particles were found on graphite terraces.

Attempts to increase the presence of azulene particles on graphite terraces, to more closely mimic azulene's interaction with graphene, were difficult with solvent deposition. A more concentrated azulene solution did not guarantee a higher surface coverage, as shown in Figure 3.6.

The solution used to prepare the sample in Figure 3.6(a) was six times as concentrated as that used for the samples in Figures 3.6(b) and 3.6(c), yet there was much less azulene surface coverage. Even the surface coverage between Figures 3.6(b) and 3.6(c) were quite different, even though the same concentration and amount of solution was used to dose the graphite surface. In many cases, we were unable to find azulene molecules on the surface after preparing a sample. We attempted to double-dose the graphite surface with additional azulene solution, but that greatly increased the risk of surface contamination.

Furthermore, dichloromethane itself presented a problem for the graphite surface. While dichloromethane was originally used as a solvent because it could dissolve the most substituted azulenes that we would eventually study, we observed evidence that dichloromethane could damage the graphite surface. An example of this damage is shown in Figure 3.7. If dichloromethane was present on the graphite surface for longer than 10 seconds, etch pits would form primarily along the step edges. This was especially problematic when using more concentrated azulene solutions (> 5.0 mM), as the dichloromethane would take longer to evaporate. Hexanes was not pursued further as a solvent, because it did not dissolve many other azulene derivatives. Toluene, another solvent that could dissolve many azulene-based compounds, was not used because it adsorbs well to the graphite surface[44]. Any extra adsorbants could interfere with surface potential mapping.

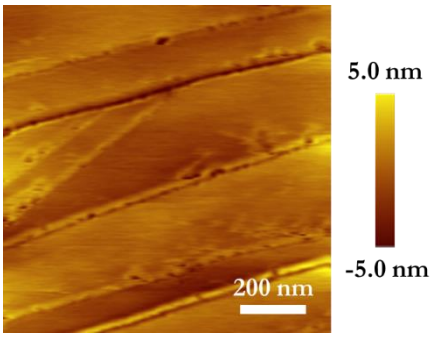

Figure 3.7: A graphite surface damaged by excess exposure to dichloromethane. This is a 1.0 μm x 1.0 μm image, taken at a scan rate of 1.0 μm/s.

Ultimately, the solvent deposition method was not ideal because it resulted in an inconsistent distribution of molecules on the surface. Solvent-facilitated diffusion allowed molecules to mostly adsorb to the graphite step edges when we wanted to see more molecules on the terraces.

Dichloromethane also could damage the graphite surface. We moved to a vapor deposition method that eliminated the need for solvent and would hopefully result in more azulene surface coverage.

3.4.2 Vapor Deposition of Azulene and Naphthalene – Analysis of Molecular Dimensions

Figure 3.8 shows a representative set of NCAFM topography images for vapor-deposited azulene and naphthalene on graphite. Particles still primarily adsorb to the step edges, even in the absence of solvent. Although, isolated particles on the terraces were much easier to locate.

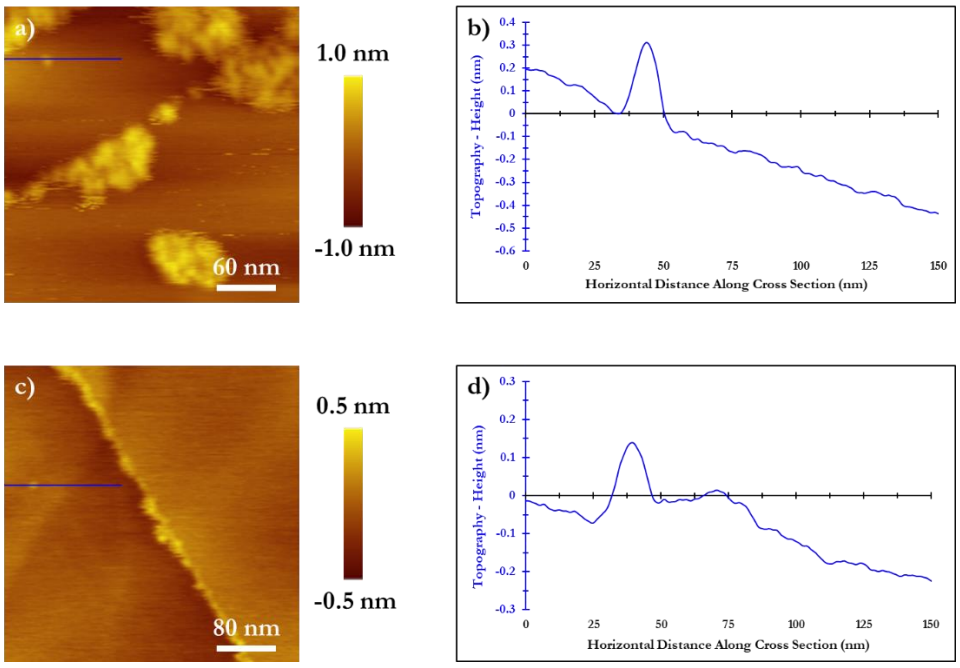

Figure 3.8: Representative NCAFM topography images of vapor-deposited molecules on graphite. (a) 300 nm x 300 nm image of azulene on graphite, taken at a scan rate of 300 nm/s. (b) Cross section through blue line in (a). (c) 400 nm x 400 nm image of naphthalene on graphite, taken at a scan rate of 333 nm/s. (d) Cross section through blue line in (c).

Topography cross-sectional analysis was used to quantify the length, width, and height of isolated particles. Examples of cross sections for azulene and naphthalene are shown in Figures 3.8(b) and 3.8(d), respectively. The length and width were measured using two perpendicular cross sections and quantified as the full width at half maximum (FWHM) of the peaks. The length was automatically designated as the longer distance. The height was defined as the relative difference between the peak's maximum and the background baseline. A summary of results for both

dropcasted and vapor-deposited azulene, and vapor-deposited naphthalene samples is included in Table 3.1.

Molecule	Deposition Method	Location On Surface	# Particles Analyzed	Length (nm)	Width (nm)	Height (nm)
Azulene	Dropcast (DCM*)	Step Edge	17	11.0 ± 0.9	9.3 ± 0.6	0.51 ± 0.09
		Terrace	8	11.7 ± 2.0	8.9 ± 1.6	0.36 ± 0.08
	Dropcast (H**)	Step Edge	32	11.4 ± 0.8	9.4 ± 0.7	0.34 ± 0.04
	Vapor Deposition	Step Edge	4	12.1 ± 5.7	10.2 ± 4.3	0.31 ± 0.15
		Terrace	32	15.3 ± 1.4	11.9 ± 1.3	0.47 ± 0.07
Naphthalene	Vapor Deposition	Step Edge	6	11.2 ± 2.0	9.3 ± 2.6	0.23 ± 0.08
		Terrace	15	11.3 ± 1.3	9.8 ± 1.6	0.20 ± 0.04

Table 3.1: Summary of topographical cross-sectional analysis of isolated particles on graphite. DCM*: dichloromethane solution. H**: hexanes solution. Averages are reported with 95% confidence intervals.

For samples that were prepared via solution dropcasting, particles were much more likely to be found on the graphite step edges rather than the terraces due to solvent-facilitated diffusion. In the case of dropcasting from a hexanes solution, no isolated azulene particles were found on terraces after several experiments. When using vapor deposition, isolated particles were more likely to be found on the terraces. Fewer particles were analyzed on the step edges in the vapor deposition samples because the step edges were normally coated with molecules; it was difficult to find isolated particles on the step edges with the vapor deposition method.

The measured lengths of these molecules range from 11 – 15 nm, while the widths range from 9 – 12 nm. We are not able to distinguish the length from the width, or azulene from naphthalene, using NCAFM because the lateral dimensions are too similar within error. Figure 3.9 shows the expected lateral dimensions of azulene and naphthalene calculated with Chem3D. The measured length and width for both molecules is about an order of magnitude larger than expected because the lateral resolution of these AFM-based

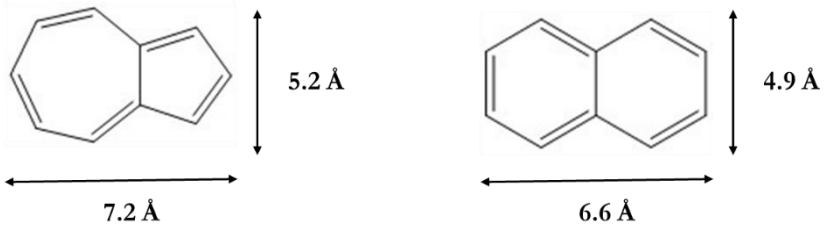

Figure 3.9: Expected lateral dimensions of azulene and naphthalene obtained from Chem3D. The energy of the molecule was minimized with MM2 before calculating the distances.

measurements is limited by the radius of the tip. The NCHPt tips have an average radius of 25 nm due to the conductive coating[40]. Therefore, any small features imaged on the surface will have measured lateral dimensions in the tens of nanometers.

Azulene's particle height ranges from 0.3 – 0.5 nm for all deposition methods, while naphthalene's particle height is about 0.2 nm. There is no statistical difference between some of the measurements when error is considered. Given that the interlayer spacing of graphite sheets is 0.34 nm,[1] these measured heights suggest that azulene and naphthalene lay flat on the graphite surface and physisorb through π-stacking interactions. Measuring an azulene particle height slightly larger than 0.34 nm is not inconsistent with the previous statement because the azulene molecule does not exactly match the graphite lattice. Lattice mismatch can cause repulsion, resulting in a slightly larger distance between the graphite and azulene. Given that the naphthalene's carbon backbone matches the graphite lattice, it would be unexpected to see particle heights larger than 0.3 nm. Furthermore, azulene's interaction is also likely to be weaker than naphthalene's with graphite due to the lattice mismatch.

Based on the lateral and height dimensions we identify these particles as single molecules, not clusters. These same particles were used for surface potential cross-sectional analysis to quantify how individual molecules locally affect graphite's work function.

3.4.3 Quantifying Effect of Azulene and Naphthalene on Graphite's Work Function

Figure 3.10 shows a representative set of topography and surface potential images for vapor-deposited molecules on graphite. These images show examples of isolated azulene (Fig. 3.10(a)) and naphthalene (Fig. 3.10(d)) molecules adsorbed on terraces, with their corresponding surface potential images. In both examples, the surface potential shows negative contrast over locations with molecules compared to the clean graphite terrace. However, the KPFM contrast's magnitude qualitatively appears different in each image. The contrast appears to be confined to the boundaries

of the molecules. The surface potential images of vapor-deposited azulene are consistent with those of dropcasted azulene.

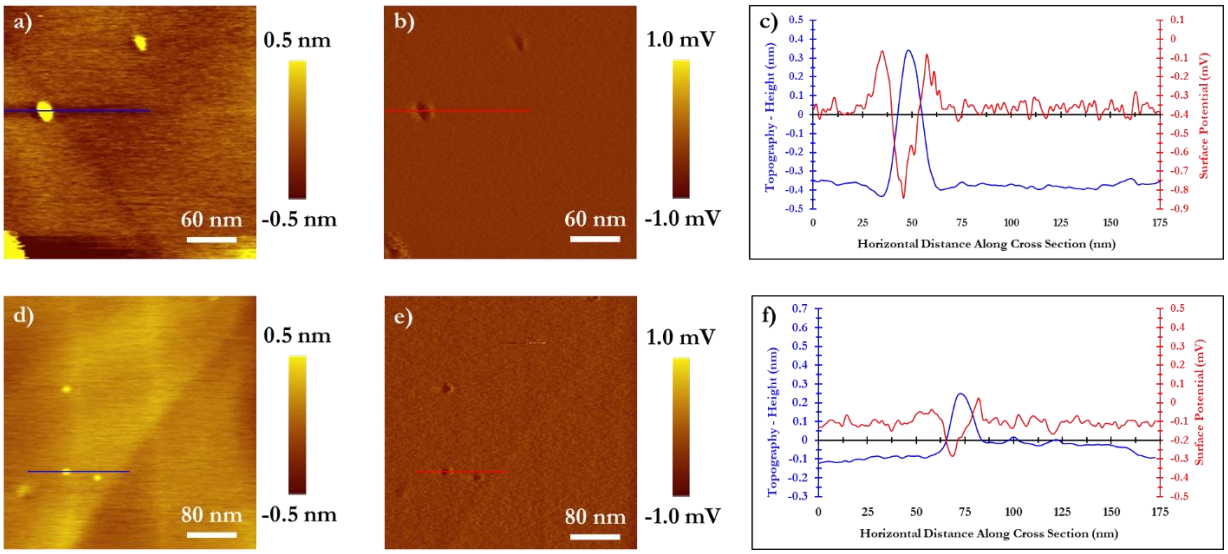

Figure 3.10: Representative topography and surface potential images of isolated molecules on graphite terraces. All samples were prepared using vapor deposition. (a) 300 nm x 300 nm topography image of azulene on graphite, taken at a scan rate of 200 nm/s, and (b) its corresponding surface potential image. (c) Cross sections through the blue line in (a) and red line in (b). (d) 400 nm x 400 nm topography image of naphthalene on graphite, taken at a scan rate of 333 nm/s, and (e) its corresponding surface potential. (f) Cross sections through the blue line in (d) and red line in (e).

Cross-sectional analysis was used, on the same set of molecules presented in Table 3.1, to quantify some parameters related to the surface potential. This data is presented in Table 3.2. The relative difference in surface potential, also known as the contact potential difference (CPD), between where molecules were adsorbed, and the clean graphite surface was measured. Using the surface potential cross section in Figure 3.10(f) as an example, the measured surface potential (or CPD) between the tip and clean graphite terrace is about 0.1 mV. The minimum of the CPD peak between the tip and area with the adsorbed naphthalene molecule is about -0.05 mV. Therefore, the relative CPD is about -0.15 mV between the area with adsorbed naphthalene and clean terrace. This is reported as the "Molecule-HOPG CPD" in Table 3.2. The width (FWHM) of the surface potential peaks was also measured.

Molecule	Deposition Method	Location On Surface	# Particles Analyzed	Molecule – HOPG CPD (mV)	CPD Peak Width (nm)
Azulene	Dropcast (DCM*)	Step Edge	17	-0.64 ± 0.08	7.2 ± 1.0
		Terrace	8	-0.47 ± 0.06	6.3 ± 1.2
	Dropcast (H**)	Step Edge	32	-0.37 ± 0.03	7.3 ± 0.7
	Vapor Deposition	Step Edge	4	-0.20 ± 0.13	7.0 ± 2.1
		Terrace	32	-0.27 ± 0.06	9.7 ± 1.0
Naphthalene	Vapor Deposition	Step Edge	6	-0.09 ± 0.08	---
		Terrace	15	-0.14 ± 0.03	---

Table 3.2: Summary of surface potential cross-sectional analysis of isolated particles on graphite. DCM*: dichloromethane solution. H**: hexanes solution. Averages are reported with 95% confidence intervals.

The width of the CPD peaks for azulene are the same as, or smaller than, the lateral dimensions reported in Table 3.1. This suggests that the local doping effect on the graphite substrate does not extend laterally beyond where the molecule is adsorbed. Averages for the CPD peak widths were not reported for naphthalene because some cross sections did not show CPD contrast. Therefore, some measurements had no CPD peak widths. Including these measurements drastically distorted naphthalene's average CPD peak width and standard deviation.

Comparing the azulene-HOPG contact potential differences between deposition methods, there is spread in the values especially for molecules on step edges. Within each deposition method, the molecule-HOPG CPD is statistically similar whether molecules are found on step edges or terraces. However, the azulene-HOPG CPD's for step edge molecules from a dichloromethane solution and vapor deposition are different. These surfaces were exposed to DCM for less than 10 seconds, so it assumed that the solvent is not chemically altering the graphite substrate or azulene molecules. There is no reason to expect that the azulene-HOPG CPD should depend on deposition method. This discrepancy could be partially attributed to the small number of molecules that were analyzed in each category. There is also inherent error when analyzing molecules that are adsorbed to the step edges. "Internal" and "external" step edges were not distinguished during analysis. If azulene is adsorbed to an external step edge that is chemically different from the surrounding graphite terrace, it could affect the measured CPD. Including a mixture of molecules adsorbed to "internal" and "external" step edges in this analysis could explain the discrepancies in some values.

We combined surface potential results from terrace molecules only and present this data in Table 3.3. Histograms of the molecule-HOPG contact potential differences are presented in Figure 3.11.

Molecule	# Particles Analyzed	Molecule-HOPG CPD (mV)	CPD Peak Width (nm)
Azulene	40	-0.31 ± 0.06	9.0 ± 1.0
Naphthalene	15	-0.14 ± 0.03	---

Table 3.3: Compiled surface potential data for molecules only adsorbed on graphite terraces**.** Averages are reported with 95% confidence intervals.

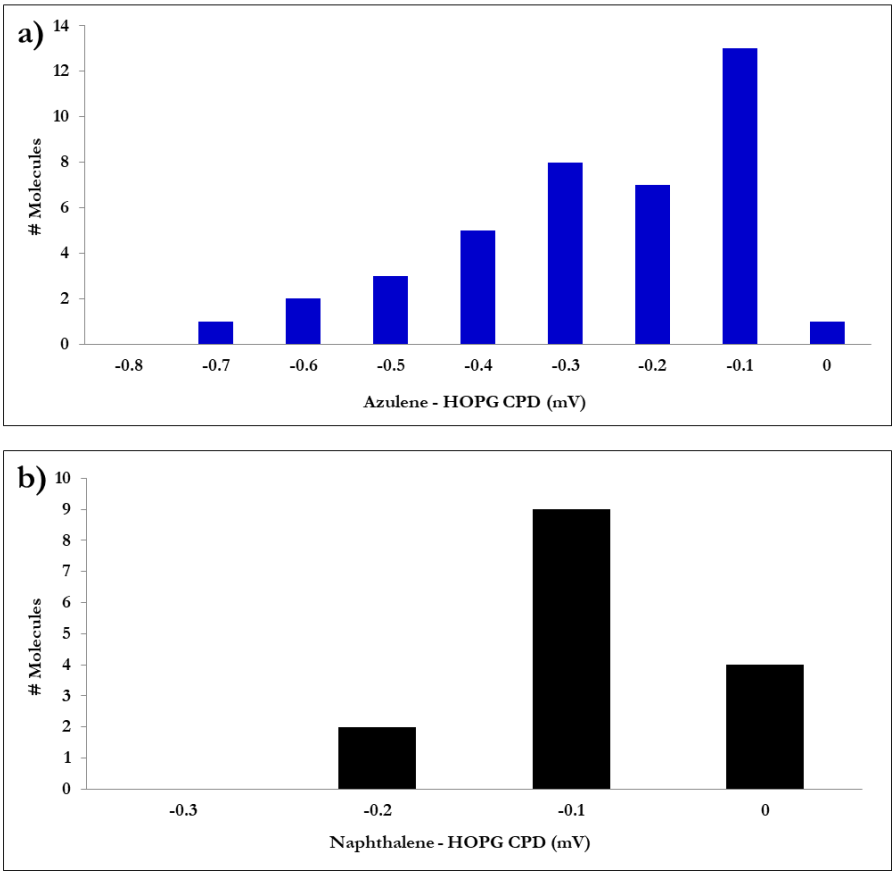

Figure 3.11: Histograms of the relative contact potential difference between (a) azulene and (b) naphthalene on graphite, respectively. Only molecules that were adsorbed on graphite terraces are included.

For both azulene and naphthalene, the relative molecule-HOPG contact potential difference is negative. This means that the local work function where a molecule is adsorbed is larger than clean graphite's work function. Both azulene and naphthalene act as p-type dopants on graphite. The naphthalene-HOPG CPD distribution shown in Figure 3.11(b) is very narrow, centered at -0.14 mV. There is much more spread in the azulene-HOPG CPD distribution shown in Figure 3.11(a),

but azulene generally has a larger p-type doping effect on graphite. This was expected considering that naphthalene's structure is very similar to graphite's, whereas azulene's structure is quite different.

Figure 3.12 shows the approximate relationship between graphite's Fermi level and the frontier molecular orbitals of azulene and naphthalene. This figure is adapted and modified from Greg Smith's dissertation[44], and can be used to explain azulene and naphthalene's relative doping effect. Graphite's work function is measured to be 4.6 – 4.8 eV,[14-16] so it is estimated to be 4.7 eV for the purpose of this figure. Azulene and naphthalene's ionization energies are measured as 7.4 eV and 8.1 eV, respectively.[45] Azulene, a dark blue compound, absorbs in the visible region of the electromagnetic spectrum; the energy difference between azulene's frontier molecular orbitals is 1.8 eV (700 nm).[34, 35] Naphthalene absorbs in the ultraviolet region at 285 nm,[36] so its frontier molecular orbital energy gap is 4.4 eV. Using the ionization energy as the energy required to remove an electron from the highest occupied molecular orbital (HOMO) with the relative energy spacing between the frontier molecular orbitals obtained from absorption spectra determined the level placement in Figure 3.12. The energy of these orbitals is displayed assuming that the molecule and substrate are far apart and not interacting. This approximation is used to infer which direction electrons would transfer between a dopant and the graphite substrate.

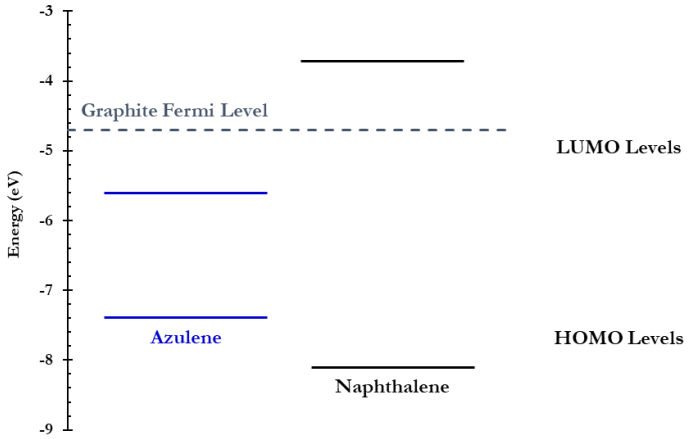

Figure 3.12: Relative relationship between the frontier molecular orbitals of azulene and naphthalene, and graphite's Fermi level. The placement of these energy levels is approximate and based off multiple combinations of experiments.

Azulene's LUMO is closest to, and lower in energy than, graphite's Fermi level. According to the integer charge transfer model[46-48] described in Chapter 1, this is consistent with p-type doping behavior. It is favorable for electrons to transfer from graphite to azulene because azulene's unoccupied orbital is lower in energy than graphite's Fermi level.

Naphthalene, however, does not follow the integer charge transfer model based on Figure 3.12. This energy level diagram suggests that there should be no charge transfer between naphthalene and graphite. There is not enough thermal energy at room temperature for an electron to transfer from graphite's Fermi level to naphthalene's LUMO, or from naphthalene's HOMO to graphite's Fermi level. However, we measure p-type doping behavior when naphthalene is adsorbed to graphite. This discrepancy suggests that charge transfer might not be the primary mechanism for doping in these adsorbed molecules. The pillow-effect is observed in all adsorbed molecules, but this should result in a decrease of the local work function (n-type doping effect) due to minimization of the surface dipole. Naphthalene is a nonpolar molecule, so it is not expected to strongly affect electron distribution in the substrate. Perhaps lattice mismatch or modification of the local electronic structure could be attributed to this discrepancy. If the molecule was not adsorbed in the most energetically favorable orientation on the surface, this could modify the surface dipole unexpectedly. Our straightforward model might not accurately predict the relative energies of the dopant's and substrate's electronic energy levels, if their characteristics are modified upon interacting with each other.

3.4.4 Clusters' Effect on Measured Surface Potential

Up to this point, data analysis focused on single, isolated molecules to quantify their effect on graphite's local surface potential. However, clusters of molecules were much more common on graphite's terraces. Figure 3.13 shows an example of azulene on HOPG, made with vapor deposition, where clusters are predominant.

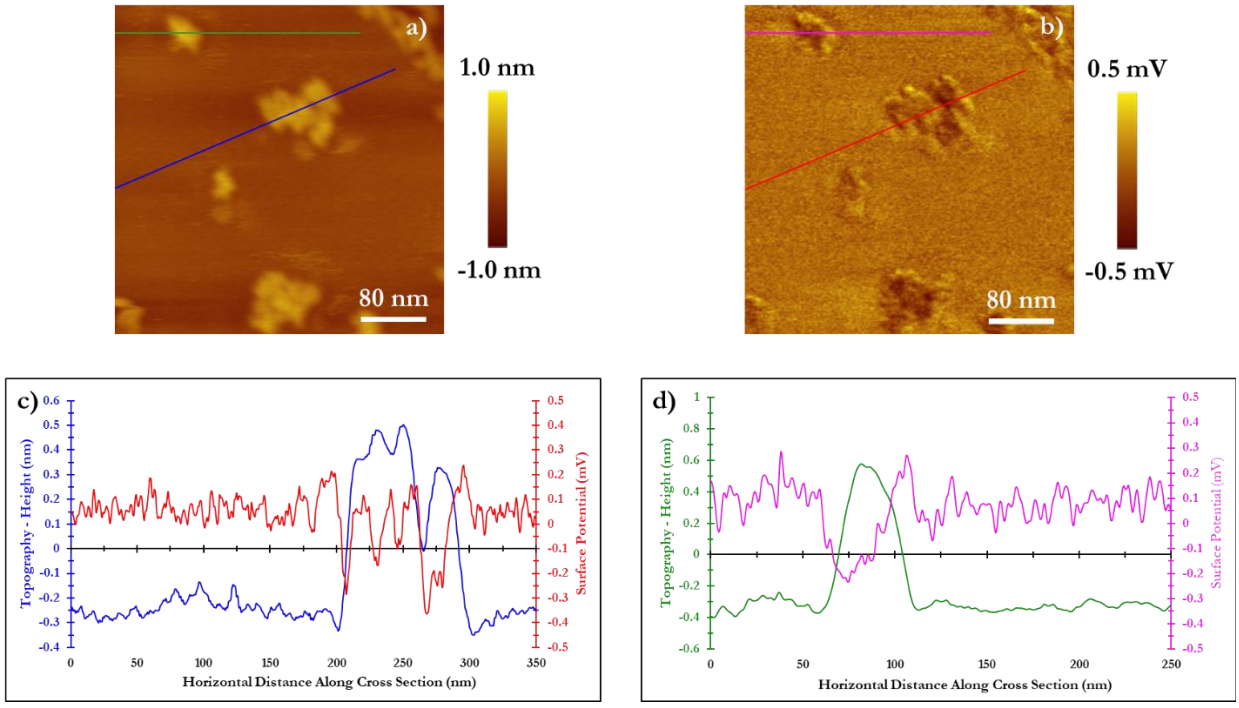

Figure 3.13: Representative topography and surface potential images of vapor-deposited azulene on graphite, where clusters of azulene are predominant on graphite's terraces. (a) 400 nm x 400 nm topography image collected using a 500 nm/s scan rate, and (b) its corresponding surface potential image. (c) Topography and surface potential cross sections through a large cluster, indicated with the red and blue lines in (a) and (b). (d) Topography and surface potential cross sections through a small cluster, indicated with the green and pink lines in (a) and (b).

The size of clusters is not uniform – it varies greatly between samples and imaging location. Figure 3.13(c) shows topography and surface potential cross sections through a large cluster. This cluster is about 175 nm wide and 0.9 nm tall; these dimensions are much larger than that observed of the single molecules reported in Section 3.3.2. The topography of this cluster is not uniform; the height varies. Sometimes, as shown in Figure 3.13(d), individual features cannot be resolved within the cluster. This cluster appears as a single peak that is about 1 nm tall and 25 nm wide. The number of molecules contained within each cluster, and their orientation relative to each other, cannot be determined with NCAFM. The tip is too broad to be able to see fine structure within the clusters.

As was the case with the single molecules, the surface potential where the clusters are adsorbed is negative compared to the clean terrace. The doping effect also is locally confined to where the clusters are adsorbed. The azulene-HOPG CPD of the large cluster in Figure 3.13(c)

varies with the topography; it ranges from -0.15 mV to -0.4 mV. While in Figure 3.13(d), the azulene-HOPG CPD is about -0.5 mV. These changes in surface potential are consistent with the doping effect from the single azulene molecules presented in Table 3.3.

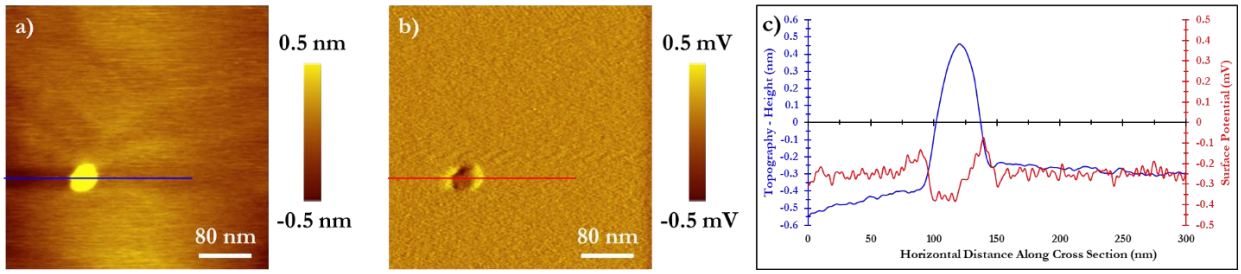

Figure 3.14: An example of a naphthalene cluster on graphite. (a) 400 nm x 400 nm topography image, collected with a 333 nm/s scan rate, and (b) its corresponding surface potential image. (c) Cross sections through the blue line in (a) and red line in (b).

These observations are not unique to azulene. Figure 3.14 shows an image of a naphthalene cluster on HOPG. This cluster appears as a single peak that is about 25 nm wide and 1 nm tall. Again, the doping effect is locally confined to the area with the adsorbed naphthalene cluster. Even though this cluster is about the same size as the azulene cluster from Figure 3.13(d), the molecule-HOPG CPD is much smaller. The naphthalene-HOPG CPD is less than -0.1 mV for this cluster. This is also consistent with the doping effect from the single naphthalene molecules. Based on these cross sections, it appears that the doping effect of clusters does not differ from that of the single molecules.

We can resolve local effects on the surface potential from single molecules and clusters adsorbed on a graphite surface. Both azulene and naphthalene have a p-type doping effect on graphite, with azulene having a larger p-type effect. In both single molecules and clusters, the change in surface potential is locally confined to where dopants are adsorbed. The fact that the clusters exhibit the same p-type effect on graphite's local surface potential as the isolated molecules is surprising. Although we cannot resolve structure within the clusters, it is unlikely that these molecules are π-stacked neatly with each other within the cluster, and relative to the graphite surface.

If orbital overlap between the clusters and substrate is not as favorable as the isolated molecules, this should decrease the probability of electron tunneling between the dopant and substrate. More work is needed to further develop the story of how these azulene-based dopants affect graphite's local work function. This is continued in Chapter 4, where substituted azulenes are adsorbed to graphite and studied with KPFM.

3.5 Conclusions

Graphene is a unique material that has been targeted for use in applications such as photovoltaics, batteries, catalysis, and sensors. Much work has been devoted to modifying graphene's electronic properties through doping in order to tailor it for specific applications. Although graphene doping has been extensively demonstrated, most doping studies are bulk measurements. A more fundamental, local understanding of how doping occurs is necessary to design adsorbants to control the doping effect's direction and magnitude.

Here, we used highly ordered pyrolytic graphite (HOPG) instead of graphene. Graphite and graphene share similar chemical and electronic properties. HOPG is commercially available and can be cleanly regenerated by mechanical cleaving. Graphite samples are also more consistent because properties of atomically thin graphene can be influenced by the supporting substrate or preparation method. Using HOPG allowed us to efficiently optimized deposition conditions and make definitive comparisons between different dopants adsorbed to graphite's terraces.

We proposed azulene-based molecules as a novel dopant for graphite, and ultimately graphene, because it is a planar, conjugated molecule that can π-stack against the graphite surface and it has a tunable frontier molecular orbital gap that can be systematically varied with substitution. We expect that changing the positions of azulene's frontier molecular orbitals relative to graphite's Fermi level will alter its doping effect. The focus of this chapter was to optimize deposition

procedures as well as to observe dopants' baseline behavior on the surface. Azulene, and its nonpolar structural isomer naphthalene, were used as dopants in this chapter. Noncontact atomic force microscopy (NCAFM) was used to visualize the topography and distribution of azulene molecules on graphite. Kelvin probe force microscopy (KPFM) was used, simultaneously with NCAFM, to map local changes in graphite's surface potential where molecules were adsorbed.

Vapor deposition was determined to be better than solvent deposition for coating graphite surfaces in azulene for several reasons. First, solvent allowed azulene molecules to diffuse and primarily adsorb to graphite's step edges. We preferred to see molecules adsorbed to graphite's terraces because we expect that area to most closely mimic graphene's properties. Secondly, it was difficult to control the amount of azulene coverage on the surface. Thirdly, the graphite substrate showed evidence of surface damage after extended exposure to dichloromethane. Finally, solvent contamination was an issue; it would cover the surface and impede our ability to image individual azulene molecules.

Vapor deposition was determined to be the cleaner deposition method and was subsequently used to deposit azulene and naphthalene on graphite. Molecules still preferentially adsorbed to the step edges and clusters were more likely to be observed on terraces, but the increased surface coverage allowed for observation of more isolated terrace molecules. Topography cross-sectional analysis was used to measure the dimensions of single, isolated molecules. The measured lateral dimensions of these molecules were about an order of magnitude larger than their true size due to convolution with the broad AFM tip. Single molecules had heights on the order of the interlayer spacing of graphite, suggesting that these molecules π-stacked flat against the graphite lattice.

The effect of these same molecules on graphite's local work function was also quantified using KPFM cross-sectional analysis. Molecules that were adsorbed on step edges were excluded. External step edges are chemically different from the surrounding graphite and could skew the

relative contact potential differences. Both azulene and naphthalene acted as p-type dopants on graphite, with azulene having a larger p-type effect. The doping effect was confined to the domains of where the molecule was adsorbed. While the integer charge transfer model predicts p-type doping for azulene based on energy level alignment between azulene and graphite, it suggests that there should be no charge transfer between naphthalene and graphite. Clusters of molecules varied in topography, but their effect on the surface potential was consistent with the single molecules. This behavior suggests that charge transfer might not be the predominant mechanism behind doping in these physisorbed molecules.

We have successfully used KPFM to map local changes in surface potential from the effects of single molecules. We can resolve changes in local contact potential differences when different molecules are adsorbed onto the surface. Further work is needed to strengthen our understanding of the mechanisms by which azulene interacts with, and modifies, the graphite surface. This work is expanded upon in Chapter 4, where substituted azulenes are investigated with NCAFM and KPFM.

3.6 References

1. Chung, D. D. L., Review Graphite. *Journal of Materials Science* **2002,** *37* (8), 1475-1489.

2. McCreery, R. L., Advanced Carbon Electrode Materials for Molecular Electrochemistry. *Chemical Reviews* **2008,** *108* (7), 2646-2687.

3. Ohler, M.; Baruchel, J.; Moore, A. W.; Galez, P.; Freund, A., Direct observation of mosaic blocks in highly oriented pyrolytic graphite. *Nuclear Instruments and Methods in Physics Research Section B: Beam Interactions with Materials and Atoms* **1997,** *129* (2), 257-260.

4. K-Tek Nanotechnology. Highly Oriented Pyrolytic Graphite (HOPG) for SPM Applications. https://kteknano.com/wp-content/uploads/2019/02/HOPG-K-TEK-Nanotechnology.pdf (accessed January 25, 2021).

5. SPI Supplies. SPI Supplies HOPG. https://www.2spi.com/category/hopg-spi-supplies/hopg/ (accessed January 27, 2021).

6. K-Tek Nanotechnology. HOPG. https://kteknano.com/product-category/hopg/ (accessed January 27, 2021).

7. Nirmalraj, P. N.; Lutz, T.; Kumar, S.; Duesberg, G. S.; Boland, J. J., Nanoscale Mapping of Electrical Resistivity and Connectivity in Graphene Strips and Networks. *Nano Letters* **2011,** *11* (1), 16-22.

8. Chen, J.-H.; Jang, C.; Xiao, S.; Ishigami, M.; Fuhrer, M. S., Intrinsic and extrinsic performance limits of graphene devices on SiO2. *Nature Nanotechnology* **2008,** *3* (4), 206-209.

9. Allen, M. J.; Tung, V. C.; Kaner, R. B., Honeycomb Carbon: A Review of Graphene. *Chemical Reviews* **2010,** *110* (1), 132-145.

10. Terrones, M.; Botello-Méndez, A. R.; Campos-Delgado, J.; López-Urías, F.; Vega-Cantú, Y. I.; Rodríguez-Macías, F. J.; Elías, A. L.; Muñoz-Sandoval, E.; Cano-Márquez, A. G.; Charlier, J.-C.; Terrones, H., Graphene and graphite nanoribbons: Morphology, properties, synthesis, defects and applications. *Nano Today* **2010,** *5* (4), 351-372.

11. Yang, G.; Li, L.; Lee, W. B.; Ng, M. C., Structure of graphene and its disorders: a review. *Sci Technol Adv Mater* **2018,** *19* (1), 613-648.

12. Lonkar, S. P.; Deshmukh, Y. S.; Abdala, A. A., Recent advances in chemical modifications of graphene. *Nano Research* **2015,** *8* (4), 1039-1074.

13. Partoens, B.; Peeters, F. M., From graphene to graphite: Electronic structure around the K point. *Physical Review B* **2006,** *74* (7), 075404.

14. Shiraishi, M.; Ata, M., Work function of carbon nanotubes. *Carbon* **2001,** *39* (12), 1913-1917.

15. Jain, S. C.; Krishnan, K. S., The thermionic constants of metals and semi-conductors I. Graphite. *Proceedings of the Royal Society of London. Series A. Mathematical and Physical Sciences* **1952,** *213* (1113), 143-157.

16. Hansen, W. N.; Hansen, G. J., Standard reference surfaces for work function measurements in air. *Surface Science* **2001,** *481* (1), 172-184.

17. Ochedowski, O.; Bussmann, B. K.; Schleberger, M., Graphene on Mica - Intercalated Water Trapped for Life. *Scientific Reports* **2014,** *4*, 6003.

18. Gu, G.; Xie, Z., Modulation doping of graphene: An approach toward manufacturable devices. *Applied Physics Letters* **2011,** *98* (8), 083502.

19. Sque, S. J.; Jones, R.; Briddon, P. R., The transfer doping of graphite and graphene. *physica status solidi (a)* **2007,** *204* (9), 3078-3084.

20. Pinto, H.; Markevich, A., Electronic and electrochemical doping of graphene by surface adsorbates. *Beilstein Journal of Nanotechnology* **2014,** *5*, 1842-1848.

21. Panchal, V.; Pearce, R.; Yakimova, R.; Tzalenchuk, A.; Kazakova, O., Standardization of surface potential measurements of graphene domains. *Scientific Reports* **2013,** *3*, 2597.

22. Zhou, S. Y.; Gweon, G. H.; Fedorov, A. V.; First, P. N.; de Heer, W. A.; Lee, D. H.; Guinea, F.; Castro Neto, A. H.; Lanzara, A., Substrate-induced bandgap opening in epitaxial graphene. *Nature Materials* **2007,** *6* (10), 770-775.

23. Giovannetti, G.; Khomyakov, P. A.; Brocks, G.; Karpan, V. M.; van den Brink, J.; Kelly, P. J., Doping Graphene with Metal Contacts. *Physical Review Letters* **2008,** *101* (2), 026803.

24. Novoselov, K. S.; Geim, A. K.; Morozov, S. V.; Jiang, D.; Zhang, Y.; Dubonos, S. V.; Grigorieva, I. V.; Firsov, A. A., Electric Field Effect in Atomically Thin Carbon Films. *Science* **2004,** *306* (5696), 666-669.

25. The Nobel Prize in Physics 2010 Press Release. https://www.nobelprize.org/prizes/physics/2010/press-release/ (accessed November 17, 2020).

26. Rietsch, J.-C.; Brender, P.; Dentzer, J.; Gadiou, R.; Vidal, L.; Vix-Guterl, C., Evidence of water chemisorption during graphite friction under moist conditions. *Carbon* **2013,** *55*, 90-97.

27. Langley, L. A.; Villanueva, D. E.; Fairbrother, D. H., Quantification of Surface Oxides on Carbonaceous Materials. *Chemistry of Materials* **2006,** *18* (1), 169-178.

28. Ray, K. G.; McCreery, R. L., Characterization of the surface carbonyl and hydroxyl coverage on glassy carbon electrodes using Raman spectroscopy. *Journal of Electroanalytical Chemistry* **1999,** *469* (2), 150-158.

29. Fryling, M. A.; Zhao, J.; McCreery, R. L., Resonance Raman Observation of Surface Carbonyl Groups on Carbon Electrodes Following Dinitrophenylhydrazine Derivatization. *Analytical Chemistry* **1995,** *67* (5), 967-975.

30. Chen, Z.; Khajeh, A.; Martini, A.; Kim, S. H., Chemical and physical origins of friction on surfaces with atomic steps. *Science Advances* **2019,** *5* (8), eaaw0513.

31. Chen, Z.; Khajeh, A.; Martini, A.; Kim, S. H., Identifying Physical and Chemical Contributions to Friction: A Comparative Study of Chemically Inert and Active Graphene Step Edges. *ACS Applied Materials & Interfaces* **2020,** *12* (26), 30007-30015.

32. Martinez-Martin, D.; Longuinhos, R.; Izquierdo, J. G.; Marele, A.; Alexandre, S. S.; Jaafar, M.; Gómez-Rodríguez, J. M.; Bañares, L.; Soler, J. M.; Gomez-Herrero, J., Atmospheric contaminants on graphitic surfaces. *Carbon* **2013,** *61*, 33-39.

33. Lee, H.; Lee, H.-B.-R.; Kwon, S.; Salmeron, M.; Park, J. Y., Internal and External Atomic Steps in Graphite Exhibit Dramatically Different Physical and Chemical Properties. *ACS Nano* **2015,** *9* (4), 3814-3819.

34. Lemal, D. M.; Goldman, G. D., Synthesis of azulene, a blue hydrocarbon. *Journal of Chemical Education* **1988,** *65* (10), 923.

35. Liu, R. S. H., Colorful Azulene and Its Equally Colorful Derivatives. *Journal of Chemical Education* **2002,** *79* (2), 183.

36. Amstutz, E. D., Comparison of the Ultraviolet Absorption Spectra of Naphthalene, Phthalazine, and Cinnoline. *The Journal of Organic Chemistry* **1952,** *17* (11), 1508-1510.

37. Shevyakov, S. V.; Li, H.; Muthyala, R.; Asato, A. E.; Croney, J. C.; Jameson, D. M.; Liu, R. S. H., Orbital Control of the Color and Excited State Properties of Formylated and Fluorinated Derivatives of Azulene. *The Journal of Physical Chemistry A* **2003,** *107* (18), 3295-3299.

38. Barybin Group Research Website. https://barybingroup.ku.edu/ (accessed October 18, 2020).

39. RHK Technology. https://www.rhk-tech.com/ (accessed November 19, 2020).

40. Nanoworld NCHPt AFM Tips. https://www.nanoworld.com/pointprobe-tapping-mode-platinum-coated-afm-tip-nchpt (accessed November 19, 2020).

41. Milde, P.; Porthun, S., Kelvin Probe Force Microscopy with the RHK R9. RHK Technology Inc.: https://www.rhk-tech.com/applications/appnotes/, 2016.

42. Boxley, C. J.; White, H. S.; Lister, T. E.; Pinhero, P. J., Electrochemical Deposition and Reoxidation of Au at Highly Oriented Pyrolytic Graphite. Stabilization of Au Nanoparticles on the Upper Plane of Step Edges. *The Journal of Physical Chemistry B* **2003,** *107* (2), 451-458.

43. Taing, J.; Cheng, M. H.; Hemminger, J. C., Photodeposition of Ag or Pt onto TiO2 Nanoparticles Decorated on Step Edges of HOPG. *ACS Nano* **2011,** *5* (8), 6325-6333.

44. Smith, G. J. Nanoscale Manipulation of Surface and Interfaces: Engineering Electrical Properties Through Nanofabrication. Ph.D. Dissertation, University of Kansas, Lawrence, KS, 2012.

45. Lias, S. G., Ionization Energy Evaluation. In *NIST Chemistry Webbook, NIST Standard Reference Database Number 69*, P.J. Linstrom, W.G. Mallard, National Institute of Standards and Technology, Ed. Gaithersburg, MD.

46. Otero, R.; Vázquez de Parga, A. L.; Gallego, J. M., Electronic, structural and chemical effects of charge-transfer at organic/inorganic interfaces. *Surface Science Reports* **2017,** *72* (3), 105-145.

47. Braun, S.; Salaneck, W. R.; Fahlman, M., Energy-Level Alignment at Organic/Metal and Organic/Organic Interfaces. *Advanced Materials* **2009,** *21* (14-15), 1450-1472.

48. Franco-Cañellas, A.; Duhm, S.; Gerlach, A.; Schreiber, F., Binding and electronic level alignment of π-conjugated systems on metals. *Reports on Progress in Physics* **2020,** *83* (6), 066501.

Chapter 4: Altering Graphite's Local Surface Potential Using Azulene-Based Dopants

4.1 Abstract

This work is an extension of the research presented in Chapter 3. Azulene is an interesting, novel dopant for graphene because its frontier molecular orbital gap can be selectively tuned with substitution. In principle, shifts in the dopant's energy levels should affect charge transport when these molecules are adsorbed on graphite. Highly ordered pyrolytic graphite (HOPG) substrates were used instead of graphene because graphite samples provide a more consistent substrate to compare differences in dopants' behavior on the surface. Vapor deposition was used to deposit substituted azulenes on HOPG substrates. Noncontact atomic force microscopy (NCAFM) and Kelvin probe force microscopy (KPFM) were used in tandem to collect topography and surface potential maps of these samples.

Topographical cross-sectional analysis was used to identify single molecules adsorbed to graphite's terraces. As with unsubstituted azulene, the dopant's measured lateral dimensions were an order of magnitude larger than their true values due to the AFM tip's broad radius. We were unable to resolve any changes in length or width with substitution on the azulene framework because these changes are too small to be resolved with this AFM tip. Single molecules had heights consistent with graphite's interlayer spacing, indicating that they π-stack flat against the graphite surface.

While topographical measurements for the substituted azulenes were like that of unsubstituted azulene, the substituted molecules displayed different effects on graphite's local surface potential. The trends in relative contact potential differences (CPD) could not be explained using just the integer charge transfer model. Not only does substitution shift the energy of azulene's frontier molecular orbitals, it also modifies the molecule's overall dipole moment. Published literature suggests that other mechanisms that modify the surface's dipole moment are also

responsible for changing the surface's local work function. Therefore, we suspect that a balance between charge transfer, the pillow effect, and surface dipole modifications from polar adsorbants are responsible for the trend in doping. A multiple linear regression that fit the measured CPDs to these three possible mechanisms showed moderate linear correlation when naphthalene was excluded from the analysis. The analysis suggested that the pillow effect and charge transfer mechanisms contribute more to the local doping effect than surface dipole modifications from the polar adsorbants. However, this analysis method was not enough to fully describe the trend in measured CPDs. Computational modeling of how adsorption orientation, interaction strength, and electronic structure changes when using different substituted azulenes as dopants would add insight to our experimental data. This would allow us to describe more accurately, and ultimately predict, the role these mechanisms play in the local doping effect.

We attempted to image other substituted azulenes, with nonplanar functionalities, on graphite but were unsuccessful because these molecules desorb from the graphite in both ambient and vacuum environments. The bulky substituents inhibit the azulene backbone from π-stacking with the graphite lattice, leading to weaker physisorption. Cooling the samples was unhelpful due to two competing processes. First, loosely bound contamination adsorbs to the cold samples. It also takes time for the sample's temperature to stabilize inside the vacuum chamber, by which time most of the bulky molecules have desorbed. If our method of vapor deposition is to be continued, only planar substituted azulenes should be considered.

4.2 Introduction

4.2.1 Frontier Molecular Orbital Tuning of Substituted Azulenes

We first introduced azulene in Chapter 3 as a potential dopant for graphene because it is a conjugated organic molecule that could π-stack on graphene's surface. Therefore, azulene could

modify graphene's local work function through physisorption, without disrupting graphene's native conductivity. Azulene's unique frontier molecular orbital distribution provides an opportunity for tuning the orbitals' energy relative to the substrate's Fermi level. As we did in Chapter 3, we used highly ordered pyrolytic graphite (HOPG) as a substitute for graphene in these experiments.

Azulene ($C_{10}H_8$) is a fused 5- and 7- membered conjugated ring system that has complimentary frontier molecular orbital (FMO) density[2, 3], as shown in Figure 4.1. Figure 4.1(a) shows the azulene framework labeled with the numbering convention[4], while Figures 4.1(b) and 4.1(c) shows orbital density for azulene's highest occupied molecular orbital (HOMO) and lowest unoccupied molecular orbital (LUMO), respectively. FMO density is situated on alternate carbons, with HOMO density primarily on odd carbons (1, 3, 5, 7) and LUMO density primarily on even carbons (2, 4, 6, 8). Because the FMOs do not occupy the same space on the azulene backbone, they experience less repulsion compared to a molecule like naphthalene[3]. Therefore, azulene's FMO transition energy is relatively low and occurs at ~700 nm in the visible region of the electromagnetic spectrum (azulene is a dark blue compound).[3]

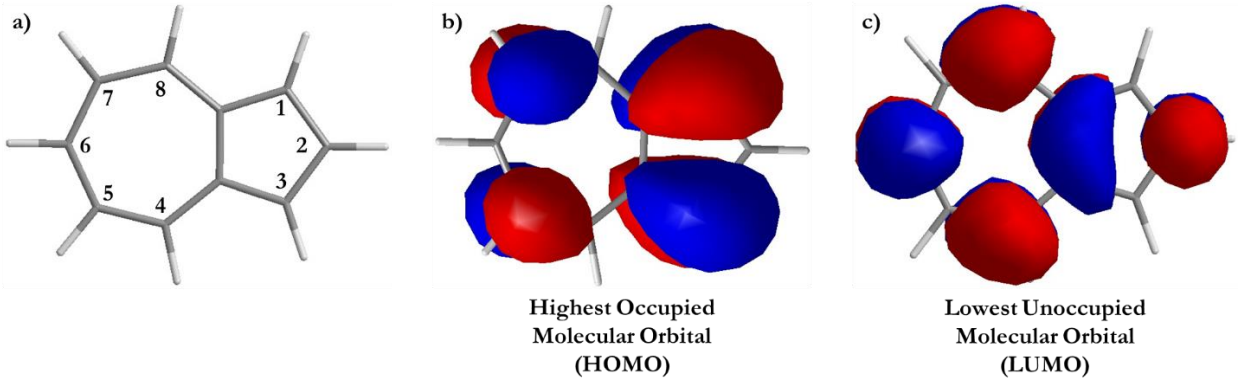

Figure 4.1: Azulene's structure and complimentary frontier molecular orbital density. (a) Azulene backbone with numbering convention. Orbital density for azulene's (b) highest occupied molecular orbital (HOMO) and (c) lowest unoccupied molecular orbital (LUMO).

This complimentary FMO density allows for either the HOMO or LUMO's energy to be independently shifted through substitution. Substituents at odd positions on the azulene backbone

selectively affect the HOMO's energy, while substituents at even positions selectively affect the LUMO's energy.[2, 3] The type of substituent matters, in addition to the substituent's location. Electron donating groups (EDGs) destabilize energy levels, while electron withdrawing groups (EWGs) stabilize energy levels.[2, 3] This phenomenon is shown using UV-Vis spectroscopy.

Figure 4.2 shows the UV-Vis absorption spectra for the following molecules: azulene, 2-iodoazulene, 2-cyanoazulene, 2-chloroazulene, and 1,3-dicyanoazulene. Figure 4.3 shows structures of all molecules relevant to this chapter. A few crystals of each molecule were dissolved in chloroform (Fisher, ACS Grade, used without further purification). The spectra were collected on a Varian Cary100 Bio UV-Visible Spectrophotometer, using a 10 mm quartz cuvette. Although the exact concentration of each solution was unknown, we verified that each solution had an absorbance under 1.0 at $\lambda_{max.}$ The spectra were normalized before plotting.

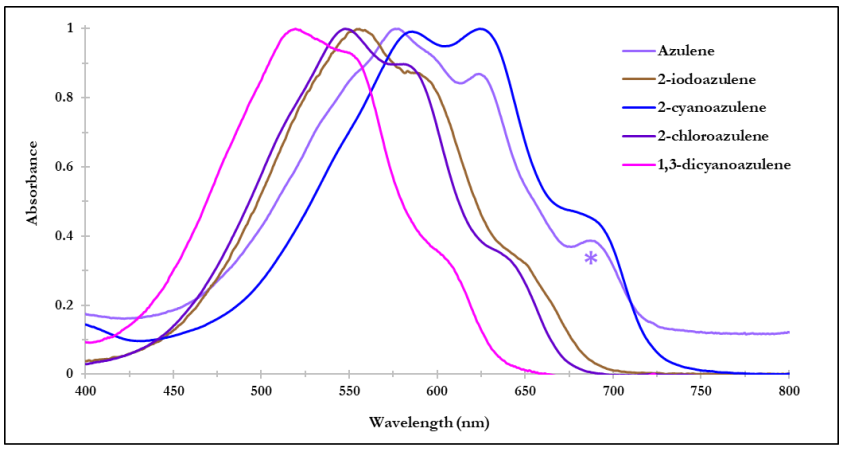

	λ_{FMO} (nm)	ΔE_{FMO} (eV)	Affected Orbital
Azulene	690	1.80	---
2-iodoazulene	651	1.90	LUMO Destabilized
2-chloroazulene	640	1.94	LUMO Destabilized
2-cyanoazulene	695	1.78	LUMO Stabilized
1,3-dicyanoazulene	605	2.05	HOMO Stabilized

Figure 4.2: Normalized absorbance spectra of substituted azulene compounds in chloroform. * Indicates unsubstituted azulene's frontier molecular orbital (FMO) transition. The table lists the wavelength and energy of each compounds FMO transition, as well as what FMO is affected by the substitution. The spectrum for 2-iodoazulene was collected by Xavier Ortiz.

The peak corresponding to azulene's FMO transition occurs at 690 nm in our spectra; this is in agreement with literature values[2, 3]. Putting electron donating substituents at the 2-position (e.g. 2-chloroazulene, 2-iodoazulene) destabilizes (increases) the LUMO's energy, thereby increasing the FMO transitional energy. On the other hand, an electron withdrawing substituent at the 2-position (e.g. 2-cyanoazulene) stabilizes (lowers) the LUMO's energy, thereby decreasing the FMO transitional energy. The FMO transitional energy increases with electron withdrawing substituents at the 1- and 3- positions (1,3-dicyanoazulene) because the HOMO's energy is stabilized. The opposite would be true with electron donating substituents at the 1- and 3-positions (e.g. 1,3-diiodoazulene); the FMO transitional energy would decrease because the HOMO's energy is destabilized. We were unable to collect an absorption spectrum for 1,3-diiodoazulene due to solubility issues. Nonetheless, one can tune azulene's FMO energy gap by controlling the location and type of substituent along the azulene framework. By independently shifting either azulene's HOMO or LUMO one could potentially change and control the doping effect that these physisorbed, substituted azulenes have on graphite's surface.

4.2.2 Objectives

The work in this chapter is an extension of what was discussed in Chapter 3. There, we learned that azulene acts as a p-type dopant on graphite and that the doping effect is locally confined to where the azulene molecule is adsorbed. We hypothesize that this is due to azulene's LUMO being lower in energy than graphite's Fermi level. It would be favorable for electrons to transfer from graphite to azulene, thereby locally increasing graphite's work function. However, this explanation did not hold when naphthalene was adsorbed to the graphite surface. P-type doping behavior was observed even though naphthalene's LUMO is significantly higher than graphite's Fermi level. In this chapter, we focus on studying the impact substituted azulenes have on graphite's local work function.

We imaged a series of substituted azulenes with either electron-donating or electron-withdrawing substituents, strategically placed at locations that modified either the HOMO or LUMO, that were deposited on HOPG via vapor deposition. Do we observe any changes in adsorption behavior, compared to bare azulene, due to the addition of substituents? Does the magnitude of the relative contact potential difference change (CPD) change when different molecules are adsorbed to the surface? If so, do those changes correlate to the energy shift of azulene's HOMO or LUMO? Noncontact atomic force microscopy (NCAFM) was performed in an ultrahigh vacuum (UHV) chamber to map the topography and surface coverage of these substituted azulenes. Isolated molecules adsorbed to graphite's terraces were identified with topographical cross sections. Kelvin Probe Force Microscopy (KPFM) was performed simultaneously with NCAFM to map the relative effects of these isolated molecules on graphite's local surface potential. Cross-sectional analysis was used to quantify the local, relative effect on the surface potential, as well as to determine the extent of the lateral doping effect on the graphite substrate.

4.3 Materials and Methods

4.3.1 Materials

A 7 x 7 mm^2 piece of single-sided highly ordered pyrolytic graphite (HOPG) was used as a substrate throughout all experiments (ZYB Grade, from K-Tek Nanotechnology). The HOPG surface was cleanly cleaved before each experiment using the Scotch tape method[5]. Large, upturned graphite flakes were peeled off the surface with tweezers. Sparsely cleaved substrates were not used in order to minimize unwanted surface contamination from the tape or previous experiments.

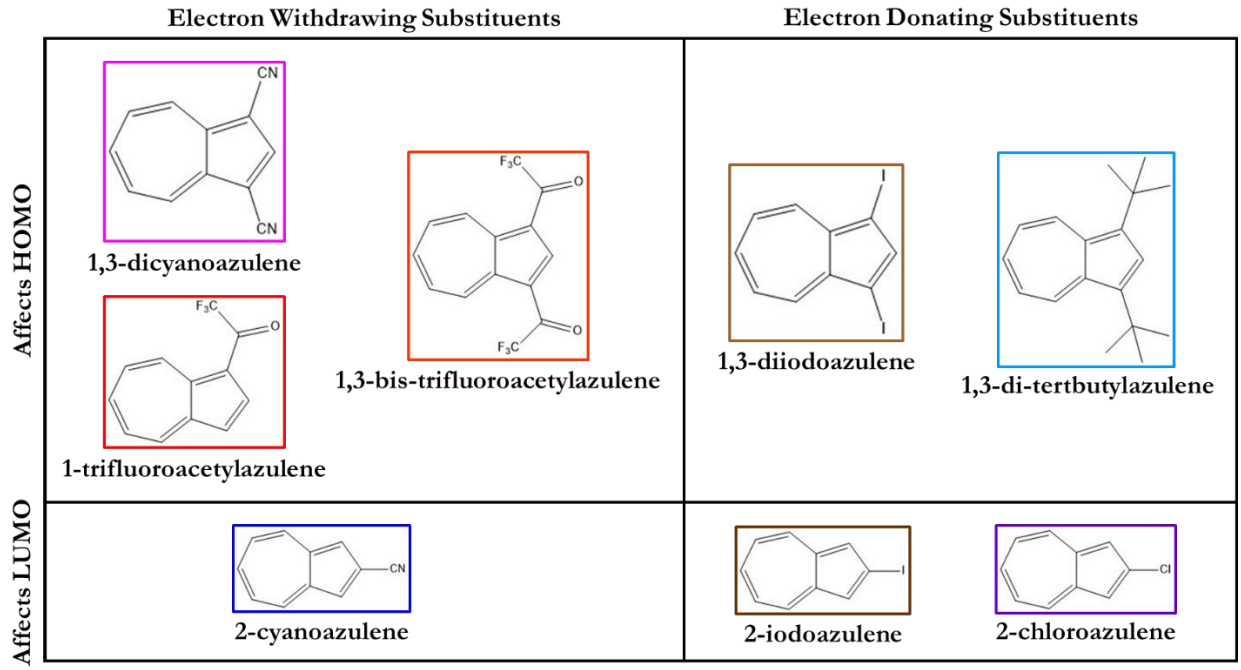

Figure 4.3: Structures of azulene-based derivatives that were studied on graphite. Boxes around structures indicate that molecule's color. Molecules are organized based on the type and location of substituent along the azulene framework.

The following molecules were synthesized and provided by the Barybin research group[6] here at the University of Kansas: 1,3-diiodoazulene, 2-iodoazulene, 1,3-dicyanoazulene, 2-cyanoazulene, 1-trifluoroacetylazulene, 1,3-bis-trifluoroacetylazulene, and 1,3-di-tertbutylazulene. Their structures are shown in Figure 4.3. Molecules are grouped according to the type of substituent: electron withdrawing (EW) or electron donating (ED). Substituents at odd positions (1,3) along the azulene framework mainly affect the energy of the highest occupied molecular orbital (HOMO). On the other hand, substituents at an even position (2) primarily affect the lowest unoccupied molecular orbital's (LUMO) energy. The Barybin group verified the compounds' purity with nuclear magnetic resonance (NMR) analysis.

4.3.2 Vapor Deposition of Azulene Derivates onto Graphite Surface

This is the same procedure that was described in Chapter 3. A clean graphite substrate was placed inside a round bottom flask, along with crystals of the molecule of interest. A house vacuum line pumped on the flask for 5 – 10 minutes. Then, the flask was sealed and the vacuum line was

disconnected. An area of the flask that had crystals was locally heated using a heat gun, causing the molecules to sublime. As molecules sublimed, a colored vapor filled the flask; the color depended on the molecule, as indicated in Figure 4.3. As the vapor cooled, crystals would coat the inside of the flask including the HOPG substrate. The flask cooled to room temperature, and then we gently opened to atmospheric pressure. The sample was transferred into the UHV chamber as soon as possible after preparation.

4.3.3 Noncontact Atomic Force Microscopy (NCAFM) and Kelvin Probe Force Microscopy (KPFM)

This is the same procedure that was described in Chapter 3. A UHV350 AFM/STM with an R9 controller from RHK Technology[1] was used to simultaneously collect NCAFM topography and KPFM surface potential images. The microscope was contained within an ultra-high vacuum (UHV) chamber at a pressure on the order of 10^{-10} torr. NCHPt tips from NanoWorld[7] were used to collect all images. These tips have a 300 kHz resonance frequency and are coated with a conductive PtIr alloy. The same tip was not used to collect all images. Most images were collected at room temperature (~ 22.5°C). The detailed procedure used to cool the sample inside the UHV chamber is described in Section 4.3.5.

NCAFM, operating in frequency modulation mode, was used to collect topography images. The shift in resonance frequency (dF) was used as the feedback loop to track the surface's topography. A dF setpoint of -10.0 Hz was generally used throughout all experiments. Scan rates varied from image to image, but were generally in the range of 0.25 – 1.0 μm/s. While the same NCHPt tip was not used to collect all images, the tips' oscillation amplitude was generally set to 50 mV across all experiments.

KPFM, operating in frequency modulation sideband mode[8], was used to collect surface potential images. The KPFM signal was detected 20.0 kHz away from the tip's natural resonance frequency with an applied bias modulation amplitude of 0.5 V.

Generally, all images for a sample were collected over a 48-hour period after the sample was first transferred into the UHV chamber. Samples were not imaged more than one week past their preparation date. Multiple samples were prepared and imaged for each dopant molecule. At least three locations were imaged on each sample. Results from images that had isolated adsorbants were combined into the collective data presented in the next section. All raw topography and surface potential images were x-slope corrected, background zeroed, and smoothed after collection. Cross-sectional analysis of surface features was not corrected for tip convolution.

4.3.4 Tapping Atomic Force Microscopy (TAFM) in Ambient Conditions

A Digital Instruments Multimode AFM with a Nanoscope IIIa controller was used to collect topography images using tapping AFM in ambient conditions. A Tap300DLC tip from Budget Sensors was used to collect all images. These tips have a 300 kHz resonance frequency and are coated with diamond-like carbon (DLC). Generally, a scan rate of 1.0 Hz and an amplitude setpoint of 1.3 V was used during imaging. The same tip was used to collect all images. An optical camera positioned above the sample stage was used to align the laser, adjust the tip's position, and capture large-scale images of the surface.

4.3.5 Cooling Sample in UHV Chamber

Some samples were cooled in the ultrahigh vacuum (UHV) chamber. Figure 4.4 shows a schematic of the cooling setup. A cylinder of $N_2(g)$ was connected to coiled copper tubing with flexible Tygon tubing. The coiled copper tubing rested inside a Styrofoam bucket and was submerged in liquid nitrogen. The end of the copper tubing was insulated and connected to the inlet line on the UHV chamber. A very gentle flow of $N_2(g)$ through the tubing cooled the chamber. The $N_2(g)$ bled into the ambient environment through the outlet line. The temperature, monitored using a Type K thermocouple, could be controlled by varying the level of liquid nitrogen inside the Styrofoam bucket and flow rate of $N_2(g)$.

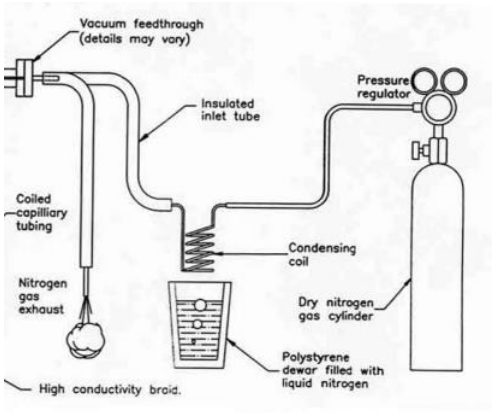

Figure 4.4: Set up used to cool samples in the UHV chamber. This picture was provided by RHK Technology[1].

4.4 Results and Discussion

4.4.1 Substituted Azulenes Show Different Surface Potential Contrast on Graphite

First, we investigated how azulene derivatives with halogen substituents interacted with the graphite surface. Figure 4.5 shows the halogenated azulenes, along with their expected dimensions.

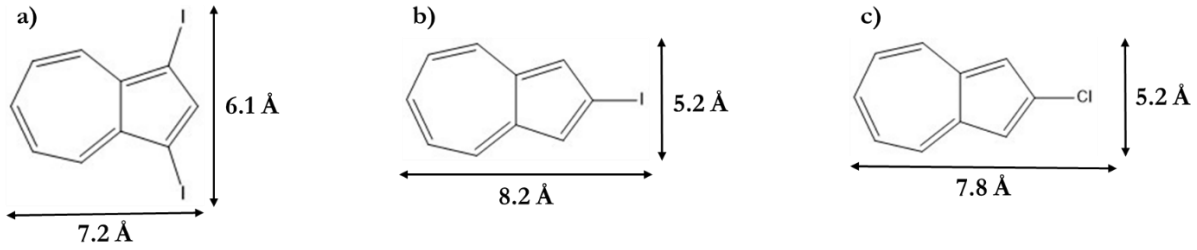

Figure 4.5: Structures and expected lateral dimensions of (a) 1,3-diiodoazulene, (b) 2-iodoazulene, and (c) 2-chloroazulene. The energy of each molecule was minimized with MM2 in Chem3D before calculating the distances.

These molecules were compared against each other because of their similar electron-donating substituents. 1,3-diiodoazulene and 2-iodoazulene differ in the locations of iodine along the azulenic backbone. As discussed in the introduction, substituents at odd positions on azulene selectively impact the HOMO's energy while substituents at even positions selectively impact the LUMO's energy. On the other hand, 2-iodoazulene and 2-chloroazulene have different halogen substituents at the same location on azulene. While both iodine and chlorine are electron-donating halogens, their donating strength differs; we wished to investigate if this impacted their effect on graphite's local surface potential.

Figure 4.6 shows representative topography and surface potential images of 1,3-diiodoazulene, 2-iodoazulene, and 2-chloroazulene on graphite. Like plain azulene (described in Chapter 3), these halogenated molecules tend to adsorb to graphite's step edges rather than the terraces. Clusters are predominantly found on terraces, but isolated particles could still be located. In some cases, loosely bound material could also be found on the graphite surface; an example of this is shown in Figure 4.6(a) with the 1,3-diiodoazulene on graphite topography image. This loosely bound material did not cover the entire surface, and areas with clean, isolated particles could still be found.

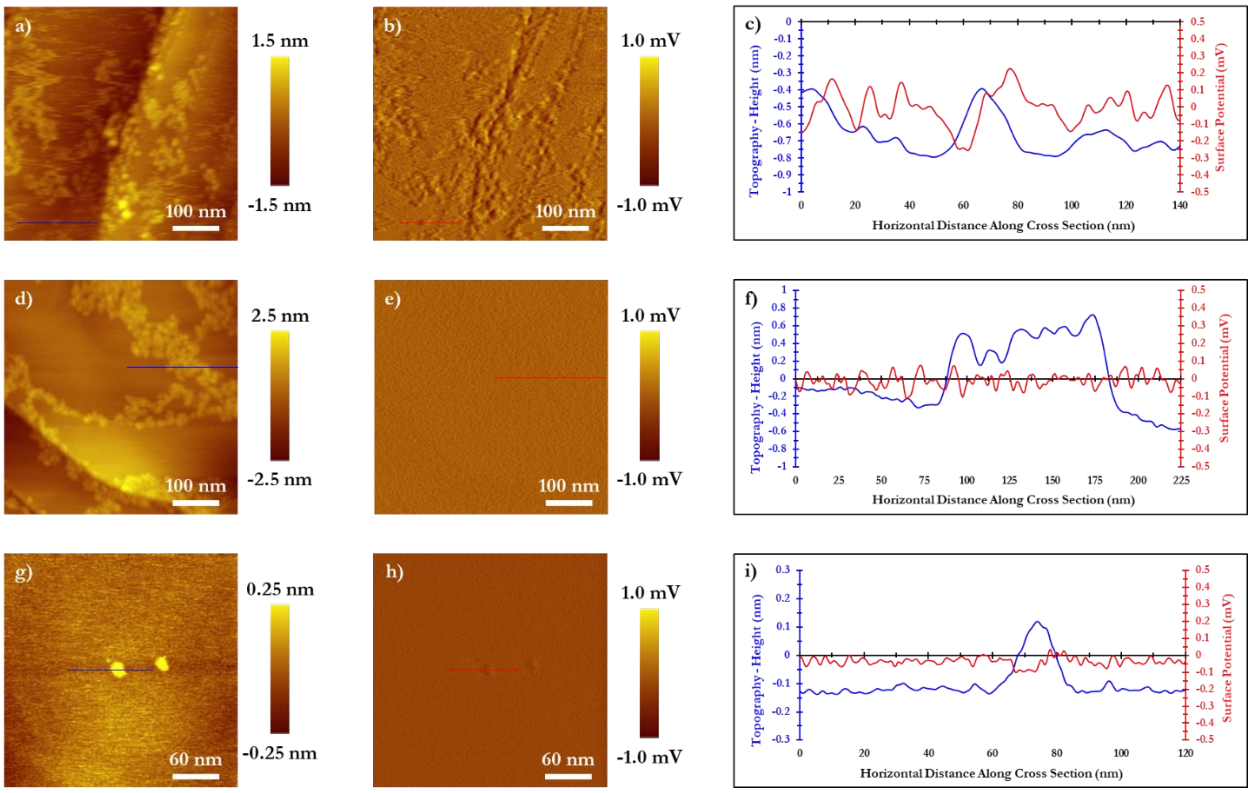

Figure 4.6: Representative topography and surface potential images of halogenated azulene derivatives on graphite. (a) 500 nm x 500 nm topography image of 1,3-diiodoazulene on graphite, taken at a scan rate of 500 nm/s, and (b) its corresponding surface potential image. (c) Cross sections through the blue line in (a) and red line in (b). (d) 500 nm x 500 nm topography image of 2-iodoazulene on graphite, taken at a scan rate of 500 nm/s, and (e) its corresponding surface potential image. (f) Cross sections through the blue line in (d) and red line in (e). (g) 300 nm x 300 nm topography image of 2-chloroazulene on graphite, taken at a scan rate of 200 nm/s, and (h) its corresponding surface potential image. (i) Cross sections through the blue line in (g) and red line in (h).

The corresponding surface potential images for these halogenated azulenes are also shown in Figure 4.6. If any contrast is visible in the surface potential image, it is negative and confined to where molecules are adsorbed. This is consistent with regular azulene, as discussed in Chapter 3. All the surface potential images shown in Figure 4.6 have the same contrast scale. Qualitatively, it appears that 1,3-diiodoazulene has a more negative contrast than 2-chloroazulene, and there is no visible contrast with 2-iodoazulene.

With the halogenated azulenes, we observed that the placement and identity of the substituent on the azulene backbone affected the measured local contact potential difference on graphite. We wanted to do a similar study with electron withdrawing, cyano- substituents. Figure 4.7

shows the structures and dimensions of these cyanated azulenes, along with their expected dimensions.

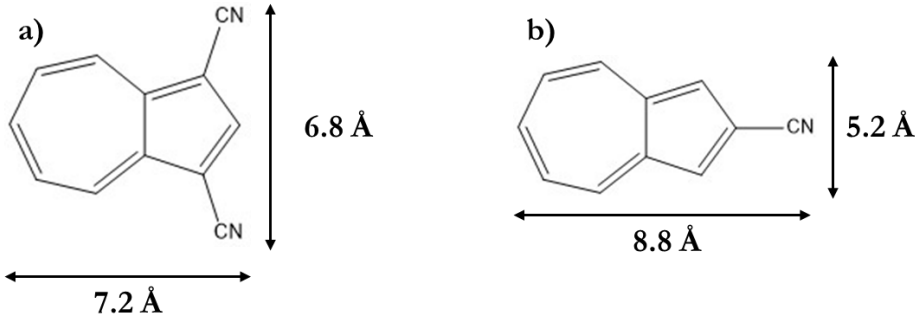

Figure 4.7: Structure and expected lateral dimensions of (a) 1,3-dicyanoazulene and (b) 2-cyanoazulene. The energy of each molecule was minimized with MM2 in Chem3D before calculating the distances.

These cyanated azulenes were compared against each other because the same substituent was located at different positions along the azulene framework, thereby independently modifying either azulene's HOMO or LUMO.

Figure 4.8 shows representative topography and surface potential images of 1,3-dicyanoazulene and 2-cyanoazulene on graphite. Isolated particles and clusters are primarily located on graphite's step edges, as usual. However, it was much easier to find isolated molecules on terraces with these cyanated azulenes. The corresponding surface potential images show negative contrast that is confined to where molecules are adsorbed; this is consistent with behavior of the other azulene derivatives. It appears that 2-cyanoazulene has more of an effect on graphite's local surface potential than 1,3-dicyanoazulene.

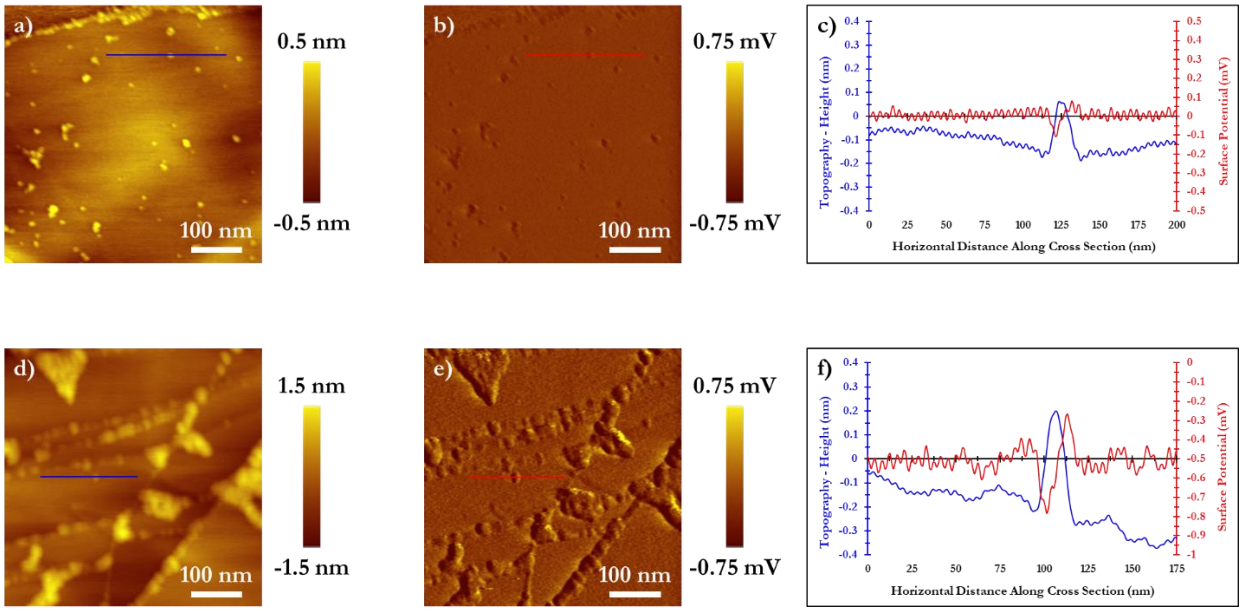

Figure 4.8: Representative topography and surface potential images of cyanated azulenes on graphite. (a) 500 nm x 500 nm topography image of 1,3-dicyanoazulene on graphite, taken at a scan rate of 500 nm/s, and (b) its corresponding surface potential image. (c) Cross sections through the blue line in (a) and red line in (b). (d) 500 nm x 500 nm topography image of 2-cyanoazulene on graphite, taken at a scan rate of 500 nm/s, and (e) its corresponding surface potential image. (f) Cross sections through the blue line in (d) and red line in (e).

The same cross-sectional analysis that was used in Chapter 3 to quantify parameters related to isolated particles on graphite's terraces was used here. Examples of cross sections through the topography and surface potential images are shown in Figures 4.6 and 4.8. Topographical cross sections were used to quantify the length, width, and height of isolated particles adsorbed to graphite's terraces. The length and width were measured using two perpendicular cross sections and quantified as the full width at half maximum (FWHM) of the peaks. The length was automatically designated as the longer measurement. The height was defined as the relative difference between the peak's maximum and the baseline. Surface potential cross sections were used to quantify the relative contact potential difference (CPD) between where molecules were adsorbed and the clean graphite terrace. The width (FWHM) of the surface potential peaks were also measured. These quantities are reported in Table 4.1. Azulene data, first reported in Chapter 3, is also included.

	# Particles	Length (nm)	Width (nm)	Height (nm)	Molecule-HOPG CPD (mV)	CPD Peak Width (nm)
Azulene	40	14.6 ± 1.2	11.3 ± 1.1	0.45 ± 0.06	-0.31 ± 0.06	9.0 ± 1.0
1,3-diiodoazulene	33	13.7 ± 0.9	11.1 ± 0.9	0.45 ± 0.05	-0.25 ± 0.03	9.6 ± 1.3
2-iodoazulene	12	10.8 ± 1.0	7.5 ± 0.8	0.43 ± 0.08	0	---
2-chloroazulene	6	16.4 ± 2.3	12.0 ± 2.2	0.29 ± 0.11	-0.085 ± 0.025	6.1 ± 3.2
1,3-dicyanoazulene	61	10.7 ± 0.5	8.4 ± 0.4	0.21 ± 0.02	-0.11 ± 0.02	7.2 ± 0.5
2-cyanoazulene	57	14.7 ± 1.0	10.7 ± 0.7	0.37 ± 0.04	-0.27 ± 0.03	7.7 ± 0.7

Table 4.1: Summary of cross-sectional analysis of isolated particles on graphite's terraces. Averages are reported with 95% confidence intervals. Azulene data, first reported in Chapter 3, is included here for comparison's sake.

The length of these molecules ranged from 11 – 16 nm, while the width ranged from 7.5 – 12 nm. Within error, these length width and measurements are not distinct. These lateral measurements are about an order of magnitude larger than the expected dimensions from Figures 4.5 and 4.7. As explained in Chapter 3, this is due to the 25 nm NCHPt tip radius[7] that limits the lateral resolution of this technique. We do not observe an increase in length or width with the addition of substituents because the lateral dimension increases are too small to be observed with these broad AFM tips. When comparing the molecules' expected dimensions from Chem3D, the addition of substituents increases length or width by about 2.0 Å (0.2 nm), at most. This is too small to be resolved with these broad AFM tips. Most of these molecules have a height between 0.3 – 0.45 nm, which is consistent with graphite's interlayer spacing of 0.34 nm.[9] It is not surprising to measure heights slightly larger than 0.3 nm, considering the adsorbed molecules might not stack perfectly with the graphite lattice and experience some repulsion. We did measure a relatively small height for 1,3-dicyanoazulene, which suggests that this molecule might have a stronger interaction with the graphite substrate. Based on the topographical measurements, we categorize these particles as single molecules lying flat against the graphite terrace.

Only a few articles have been published where KPFM has been used to map charge distribution of isolated, albeit relatively large, features adsorbed on surfaces. For example, KPFM was used to map surface potentials of isolated bicomponent nanorods (100 nm in length)[10] as well as bulky biomolecules[11]; any surface potential modification was localized to where the features were

adsorbed on the substrate. Even though our work applied KPFM to much smaller organic molecules physisorbed onto a surface, our results are consistent with their observations. The widths of the CPD peaks for these azulenes are the same, or smaller than, their lateral dimensions. Even though substitution changes the dopant's native dipole moment, this did not change the localized, spatial extent of doping. The measurements for length, width, height, and CPD peak width for the substituted molecules are consistent with regular azulene. However, there are measurable differences in the relative contact potential differences.

Figure 4.9 shows the approximate relationship between graphite's Fermi level and the frontier molecular orbitals of these substituted azulenes. This figure is adapted and modified from Greg Smith's dissertation[12], and is an expanded version of Figure 3.12 in Chapter 3. Graphite's work function is estimated to be 4.7 eV based on previous publications.[13-15] Azulene's ionization energy was measured to be 7.4 eV, and is used to estimate the placement of its highest occupied molecular orbital (HOMO).[16] Azulene's frontier molecular orbital (FMO) electronic transitional energy, measured with UV-Vis spectroscopy, is 1.8 eV (700 nm).[3, 17] This data was used to place azulene's lowest unoccupied molecular orbital (LUMO) relative to its HOMO. The energy of the substituted azulene's frontier molecular orbitals was determined using the absorption spectra in Figure 4.2. By measuring the FMO transition energy and knowing which FMO is affected based on the substituent's type and location, the substituted azulene's energy levels could be placed relative to that of regular azulene. The orbitals' energies in Figure 4.9 is a combination of several pieces of data and experiments and is displayed assuming that the molecule and graphite substrate are far apart and not interacting. This approximation is used to infer which direction electrons would transfer between a dopant and the graphite substrate.

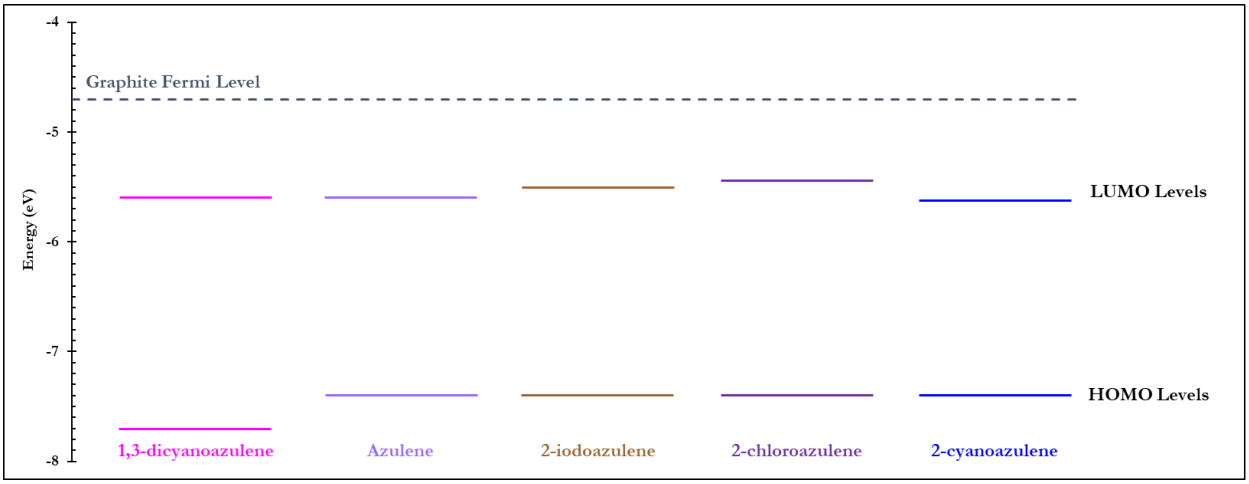

Figure 4.9: Relative relationship between substituted azulene's frontier molecular orbitals and graphite's Fermi level. 1,3-diiodoazulene is not included because we were unable to collect its absorption spectrum due to solubility issues.

The energies of the substituted molecules' FMOs shift by a small amount, between 0.05 - 0.2 eV, compared to plain azulene. This shift should not be enough to drastically change their doping properties, according to the integer charge transfer model for molecules physisorbed to metals[18-20] (this model is described in more detail in Chapter 1). Because these molecules have LUMOs lower in energy than the substrate's Fermi level, they should behave as p-type dopants (electrons could transfer from the substrate to the dopant's unoccupied orbital). Therefore, we would expect to see a negative relative CPD for these molecules adsorbed on graphite. A small change in the LUMO's energy might change the magnitude of the local CPD, but not the direction. On the other hand, we expect a change in the HOMO's energy to not affect the doping magnitude or direction because we believe the LUMO to be the primary orbital involved in charge transfer.

First, we begin with a comparison of molecules with substituents at the 2-position: 2-iodoazulene, 2-chloroazulene, and 2-cyanoazulene. Only the LUMO's energy is affected by substitution in these molecules. 2-cyanoazulene's relative CPD is the same, within error, as that of azulene. As shown in Figure 4.2, 2-cyanoazulene's LUMO is lower in energy than azulene's LUMO by 0.02 eV (a very small amount). Therefore, it is not surprising that their relative CPDs are similar.

On the other hand, 2-chloroazulene and 2-iodoazulene have relative CPDs that are more positive than that of azulene. This shift is consistent with the fact that their LUMO's are higher in energy than unsubstituted azulene's. With this argument, we expected 2-iodoazulene to have more of an effect (i.e. a more negative contrast) on the local CPD than 2-chloroazulene because its LUMO is lower in energy. However, we saw no effect on graphite's local CPD from 2-iodoazulene. It should be noted that 2-chloroazulene's CPD is very small, even smaller than that of naphthalene (shown in Chapter 3), but is not too far removed from 2-iodoazulene's CPD. This discrepancy could be due to the small number of molecules observed for these two compounds. However, it is surprising that magnitudes of these molecules' relative CPDs on graphite are so small (close to, or exactly zero). Based on Figure 4.9, their LUMOs are higher in energy than azulene's LUMO but not shifted so far up as to not favorably interact with graphite's Fermi level. The integer charge transfer model would predict that both these molecules should still behave as p-type dopants. This suggests that some other mechanism might be involved in the relative effects these substituted azulenes have on graphite's local surface potential.

Now, we compare two molecules that have substituents that selectively affect the HOMO's energy: 1,3-diiodoazulene and 1,3-dicyanoazulene. Because we hypothesized that the LUMO is the primary orbital involved in charge transfer, we expected any shifts in the HOMO's energy to not change the relative CPD compared to azulene. This is consistent with 1,3-diiodoazulene's relative CPD; it is the same, within error, to that of azulene. However, we measured a more positive CPD for 1,3-dicyanoazulene. Again, this suggests that considering charge transfer alone is not enough to explain the shifts in contact potential differences.

Up to this point, we have focused on the charge transfer aspect of doping. However, as described in Chapter 1, the work function also depends on the substrate's surface dipole moment[18-20]. The surface dipole can be modified through the pillow-effect, a result of Pauli repulsion between

electrons in the adsorbate and substrate. The pillow-effect always lowers the local work function because the surface dipole decreases. Furthermore, polar adsorbants could modify this surface dipole by influencing the electron distribution around where the molecule is adsorbed. We must also consider that placing substituents on the azulene ring changes the molecule's dipole moment, and this could affect how the molecule interacts with the graphite surface.

Table 4.2 lists the theoretically modeled dipole moments for the azulene derivatives we've adsorbed on graphite to date. The energy of the molecular structures was minimized with Chem3D's default MM2 minimization before the dipole was calculated with the semiempirical MOPAC16 program[21]. A closed-shell calculation with the PM6 basis set was used because it most closely matched azulene's literature[4] dipole moment of 1.0 Debye (D) of the available basis sets. The measured relative contact potential differences for all molecules imaged so far are also included in Table 4.2, for comparison.

	Dipole Moment (D)	**Measured Molecule-HOPG CPD (mV)**
Azulene	1.41	-0.31 ± 0.06
1,3-diiodoazulene	3.50	-0.25 ± 0.03
2-iodoazulene	3.27	0
2-chloroazulene	3.38	-0.085 ± 0.025
1,3-dicyanoazulene	6.39	-0.11 ± 0.02
2-cyanoazulene	6.19	-0.27 ± 0.03

Table 4.2: Theoretical dipole moments for all imaged molecules on graphite to date. Dipole moments were calculated using MOPAC16 with the PM6 basis set. Measured relative contact potential differences, first reported in Table 4.1, are included for comparison's sake. Averages are reported with 95% confidence intervals.

Azulene's native dipole moment points from the 7-membered to the 5-membered ring, in the plane of the molecule.[4] Adding electronegative substituents to the 5-membered ring increases the dipole moment; the cyano- substituent has a particularly strong effect. There is no clear trend in relative CPDs with the adsorbed molecules' dipole moment. The magnitude of the adsorbate's dipole moment does not correlate directly with the magnitude or direction of the relative contact potential difference. But, we expect this to have some role in modifying the local work function based on previous work analyzing adsorbants on metal substrates.[18, 20]

One can begin to elucidate the dipole moment's possible role by comparing azulene, 1,3-dicyanoazulene, and 1,3-diiodoazulene. These molecules all have LUMOs at the same energy, so we hypothesize that the charge transfer contribution to their doping effects should be the same. From the integer charge transfer model, we expected to not observe a change in relative CPD when comparing these molecules. Azulene and 1,3-diiodoazulene have similar relative CPDs within error, and their dipoles are only different by about 2.0 D. 1,3-dicyanoazulene, however, has a less negative contact potential difference and a much larger dipole (by about 5.0 D) than azulene. This suggests that an adsorbate with a larger dipole moment should make the surface potential contrast more positive (decreasing the local work function).

For molecules with substituents at the 2-position, it is more difficult to analyze what effect the adsorbate's dipole moment may have because the LUMO's energy has also changed. The idea that a larger dipole moment would increase the local work function (show a more positive CPD) might also explain why the relative CPD magnitudes for 2-iodoazulene and 2-chloroazulene are so small. However, this idea doesn't quite match with 2-cyanoazulene's measured CPD. This molecule has a much larger dipole moment than 2-chloroazulene or 2-iodoazulene, but it's relative CPD is consistent with what was expected from the charge transfer model. It should be noted that the placement of energy levels in Figure 4.9 are approximations and combine multiple experiments' data. Azulene's ionization energy was from a gas phase experiment reported on the NIST webbook[16], while the FMO energy gap was obtained from solvent-based UV-Vis absorption measurements. It is possible that 2-cyanoazulene's LUMO is stabilized (lowered in energy) more than what we measured in our absorption measurements due to solvent effects. If that is true, then we would expect a larger effect from charge transfer that could be offset by the contribution from the molecule's large dipole moment, resulting in a relative CPD that is close to that of bare azulene.

We fit the experimental results to Equation 1 using multiple linear regression to quantify the contributions of the pillow effect (P), charge transfer (C), and surface dipole modification (S) mechanisms to the relative shift in local surface potential ($\Delta\Phi$). Weighting coefficients (p, c, s) for each mechanism are included.

$$\Delta\Phi = p(P) + c(C) + s(S) \quad (1)$$

We assumed that each molecule's pillow effect contribution is the same because all the molecules have similar sizes. Therefore, the pillow effect's contribution was taken from the intercept of the multiple linear regression in our analysis. For the charge transfer independent variable (C), the molecule's LUMO energy relative to graphite's Fermi level was used in the analysis. For example, we expect azulene's LUMO (-5.6 eV) to be 0.9 eV lower in energy than graphite's Fermi level (-4.7 eV). Each molecule's theoretical dipole moment, listed in Table 4.2, was used for the surface dipole modification independent variable (S). Multiple linear regression was used to find the relative magnitudes of the weighting coefficients in Equation 1. Table 4.3 lists the regression results for analyses including and excluding naphthalene.

When naphthalene is included, there is no linear correlation in the data. The R^2 value is incredibly small, and the errors for the charge transfer and surface dipole coefficients are larger than the coefficients themselves. The data becomes more linear when naphthalene is excluded, although the fit is not perfect. The coefficients for the pillow effect and charge transfer mechanisms are much larger than that for the surface dipole modification. This suggests that the adsorbate's dipole moment has a minor contribution to modifying the local surface potential compared to the pillow effect and charge transfer. This is not unexpected, considering that the adsorbate's dipole moment is oriented

	Including Naphthalene	**Excluding Naphthalene**
p(P) (mV)	-0.18 ± 0.10	1.17 ± 0.48
c ($\frac{mV}{eV}$)	-0.055 ± 0.10	1.68 ± 0.58
s ($\frac{mV}{D}$)	-0.013 ± 0.032	0.027 ± 0.020
R^2	0.065	0.742

Table 4.3: Mechanisms' weighting coefficients obtained from multiple linear regression. Coefficients are reported with standard errors.

perpendicular to the surface's dipole because the azulenes are π-stacked flat against the graphite substrate. Previous studies from literature suggest that the dopant's dipole moment plays a much larger role when it is oriented along the same axis as the surface dipole, as in chemisorbed self-assembled monolayers.[18, 19, 22-24] While the multiple linear regression showed moderate linear correlation between the three possible mechanisms and the doping effect, it did not fully describe the doping trend.

Our work was the first to use KPFM to map local surface potential modifications of small, isolated, physisorbed organic molecules on a substrate. We were able to resolve reproducible changes in the relative surface potential when different molecules were adsorbed on the surface. However, our simple assumptions with the multiple linear regression were not enough to fully describe mechanistic contributions to changing the local work function, especially when including naphthalene. It is possible that the pillow effect is not the same for each of the molecules studied. Perhaps the nature (dipole moment, polarizability) of certain substituents influences the pillow effect more than others. By adding substituents along the azulene framework, we could also be modifying the molecules' interaction strength with the graphite substrate. It would be valuable to investigate how the electronic structure of the dopants and the graphite substrate change when interacting. Our data analysis, so far, has assumed that the bulk graphite's work function has not changed due to the low surface coverage of azulene. Furthermore, our treatment of orbital energies has been limited to when the dopant and substrate are not interacting. While our experimental data suggests that these conjugated molecules π-stack flat against the graphite lattice, we are unable to extract exactly how the dopants are adsorbed relative to the graphite lattice structure. Computational studies would help broaden our understanding of the KPFM experimental data. Modeling how structure, orbital overlap, and electronic characteristics change upon interaction would allow us to more accurately describe the role that these mechanisms play in the local doping effect.

Continuing our KPFM work with additional substituted azulenes would also broaden our picture of the interplay between the pillow effect, charge transfer, and surface dipole modification mechanisms. The next section focuses on the behavior of nonplanar substituted azulenes on graphite.

4.4.2 Behavior of Azulene Derivatives with Bulky Substituents on Graphite

The Barybin group[6] provided us with additional substituted azulenes to expand our library of graphite dopants: 1-trifluoroacetylazulene, 1,3-bis-trifluoroacetylazulene, and 1,3-di-tertbutylazulene. Their structures are shown in Figure 4.3. These molecules have different types of substituents, but the substituents' locations selectively affect the energy of azulene's HOMO. Using these molecules in surface potential experiments would expand our understanding of how the location of a substituent, its type, and its strength affects graphite's local work function.

We used vapor deposition to deposit these molecules on graphite's surface. However, after multiple experiments, we did not see molecules on the surface when we went to image these samples in the UHV chamber. To compensate, we overdosed the graphite with so many molecules so that a visible layer of crystals was present on the surface. Figure 4.10 shows an example of an overdosed azulene sample, where a dark blue layer of macroscopic crystals is seen on the surface. Yet, we were still unable to get reproducible AFM images of these molecules on the surface in vacuum. Even though the graphite surface was initially covered with molecules, upon removal from the UHV chamber the graphite surface looked clean and shiny as if it was just cleaved. It became clear that these molecules were desorbing off the graphite in the low-pressure environment.

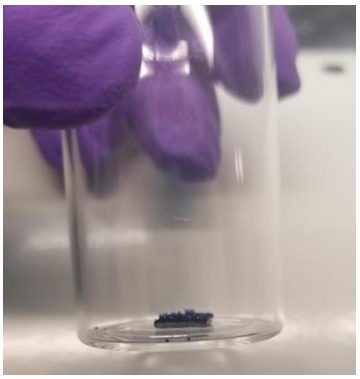

Figure 4.10: An overdosed azulene on graphite sample. A dark blue layer of azulene, with some large crystals, is visible on graphite's dark grey surface.

An optical camera attached to the side of our UHV SPM chamber captured this desorption behavior. Figure 4.11 shows a series of snapshots of an overdosed sample of 1,3-bis-trifluoroacetylazulene on graphite. Figure 4.11(a) shows the surface immediately after it was transferred into the UHV chamber (defined as zero minutes elapsed). Red-orange crystals are clearly visible on the surface. After 40 minutes (Fig. 4.11 (b)), fewer of these crystals are visible. After 4 hours (Figs. 4.11(c) and (d)), no visible orange residue remains on the graphite surface. The surface now looks grey and shiny, which is typical of freshly cleaved graphite surfaces. The 1,3-bis-trifluoroacetylazulene molecules desorbed off the graphite surface in the vacuum environment.

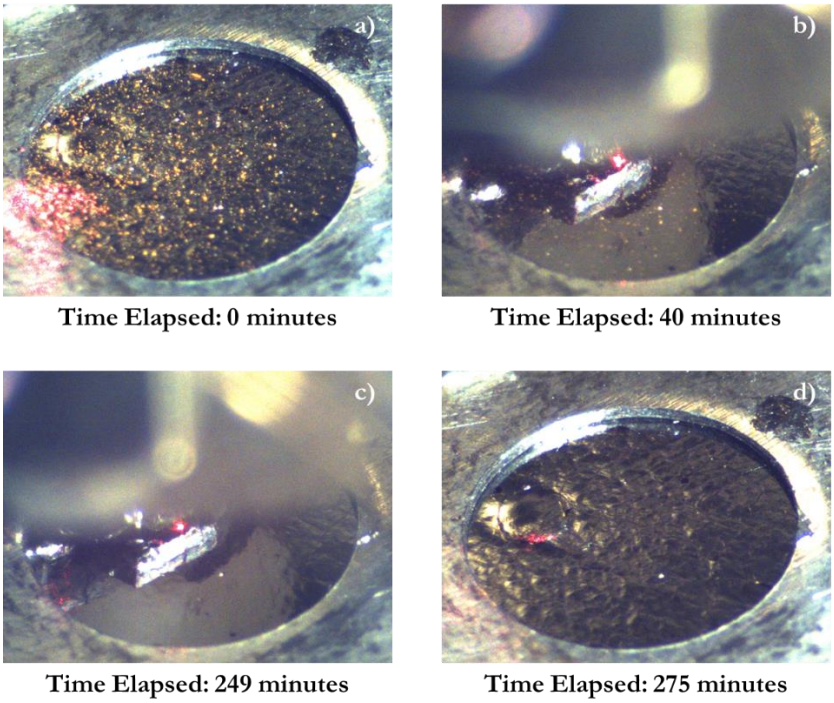

e)

Time Elapsed (minutes)	Pressure (torr)
0	1.1×10^{-9}
44	1.9×10^{-9}
58	2.0×10^{-9}
88	1.9×10^{-9}

Figure 4.11: Desorption behavior of 1,3-bis-trifluoroacetylazulene on graphite in a vacuum environment. Time elapsed indicates how long had passed after sample was transferred into the vacuum chamber. (a) Surface immediately after sample was transferred into vacuum chamber. (b) Surface after 40 minutes in vacuum chamber. SPM scan head with AFM tip had been lowered to the surface. (c) Surface after 249 minutes in vacuum environment. SPM scan head still close to surface. (d) Surface after 275 minutes in vacuum environment. SPM scan head had been retracted away from surface. (e) Pressure in the vacuum chamber, measured with an ion gauge.

The pressure, shown in Figure 4.11(e), increased after the sample was introduced inside the chamber. While it is normal for the pressure to spike as the load-lock gate is opened, the pressure typically decreases immediately after the gate is closed as the ion pump eliminates any residual

material introduced from the sample transfer. With this sample, the pressure increased for about an hour after the transfer gate had been closed. Then, the pressure began to decrease again. The desorbing 1,3-bis-trifluoroacetylazulene molecules were responsible for the pressure spike. Once most of the molecules had desorbed from the graphite surface, the pressure inside the chamber began to decrease again.

We were able to capture NCAFM topography images of this particular 1,3-bis-trifluoroacetylazulene on graphite sample; these images are presented in Figure 4.12. Figure 4.12(a) was captured one hour after the sample was transferred into the vacuum chamber. Clusters of adsorbed material are visible along the step edges and terraces, particularly at the top of the image. Figure 4.12(b) was captured in the same location as Figure 4.12(a), but an additional hour had passed. The clusters visible in the first image have diminished in size or disappeared altogether. Because the tip does not contact the surface during NCAFM imaging, we do not attribute the desorption of molecules to tip disruption. The optical camera images in Figure 4.11 show clear desorption over the entire graphite surface, not just in areas we had imaged with NCAFM.

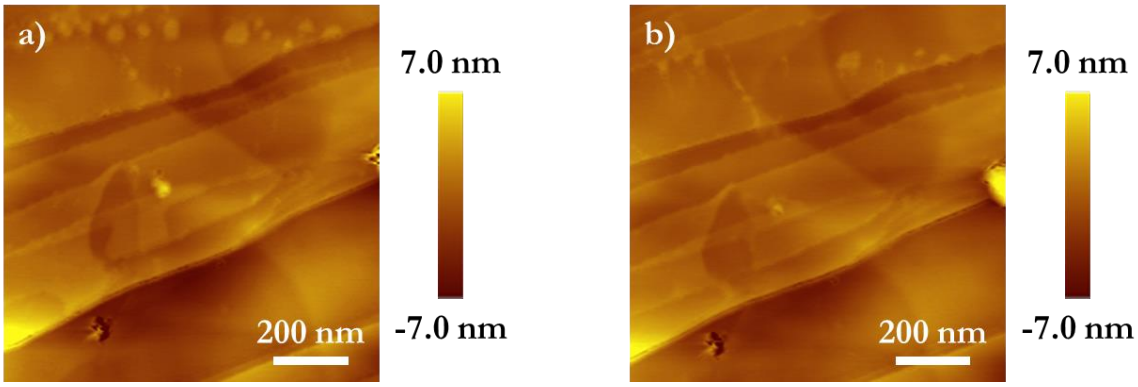

Figure 4.12: 1.0 x 1.0 μm^2 topography images, taken at a scan rate of 1.0 $\mu m/s$, of 1,3-bis-trifluoroacetylazulene on graphite (a) one hour and (b) two hours after the sample had been transferred into the vacuum chamber.

1,3-di-tertbutylazulene, 1,3-bis-trifluoroacetylazulene, and 1-trifluroacetylazulene do not physisorb as well to graphite due to their bulky substituents. The tertbutyl- and trifluroacetyl-substituents are nonplanar, so they inhibit the π-stacking interaction between the azulene backbone

and graphite lattice. Therefore, these nonplanar azulene derivatives do not physisorb as strongly to graphite as their planar counterparts. There is enough thermal energy available at room temperature for these bulky molecules to readily desorb in a low-pressure environment.

We attempted to take tapping atomic force microscopy (TAFM) topography images of another bulky azulene, 1-trifluoroacetylazulene, in ambient conditions. We wanted to see if ambient pressure would slow, or even stop, desorption from the graphite surface. While we were unable to capture clear images of clusters with TAFM, the optical camera above the sample captured desorption behavior (shown in Figure 4.13). Immediately after sample preparation (Fig. 4.13(a)), the graphite surface was covered in splotchy areas of adsorbants. As time passed, these patchy areas grew smaller and disappeared completely after an hour and half. Dark particles, which we assume to be relatively large clusters of physisorbed 1-trifluoroacetylazulene, are left behind and persist on the surface.

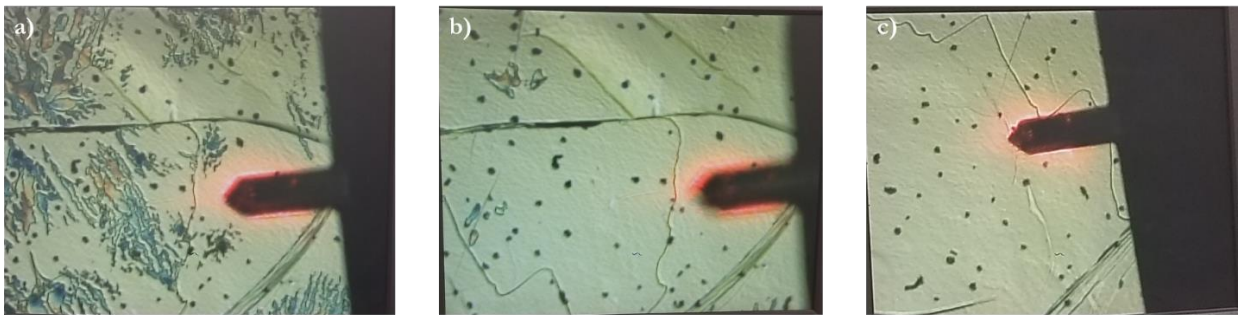

Figure 4.13: Optical camera images of 1-trifluoroacetylazulene on graphite in ambient conditions. The tapping AFM chip and cantilever (illuminated by red laser) are visible on the right of all images. (a) This picture was captured as soon as possible after sample preparation, defined as "zero" elapsed time. The remaining images were captured (b) 24 minutes and (c) 91 minutes after (a).

Even in ambient conditions, the nonplanar substituted azulenes desorb off the surface due to their inhibited π-stacking interactions with the graphite substrate. If future experiments are to be conducted with azulene-based molecules on graphite or graphene, their substituents should be planar to ensure enough molecules stably physisorb to terraces.

4.4.3 Effect of Cooling UHV SPM Sample

At room temperature, nonplanar azulene-based molecules desorb readily off graphite at ambient and UHV pressures. Perhaps cooling the samples would slow the desorption process enough to allow us to image these samples. Cooling samples is a technique routinely used in scanning probe microscopy to achieve atomic resolution[25], or to manipulate molecules on a surface.[26-28] Cooling surfaces reduces thermal motion, making it easier to resolve atoms[29]. Our RHK UHV350 system is equipped with a cryostat that can be cooled to liquid nitrogen temperatures (77.4 K or -195.8 °C, at atmospheric pressure).

We opted to use the cooled $N_2(g)$ method described in Section 4.2.5, after consultation with RHK, because it was easier to implement and would introduce less vibrations into the SPM system than pumping liquid nitrogen through the cryostat. As shown in Figure 4.14, we could control the sample temperature by manipulating the $N_2(g)$ flow rate and volume of liquid nitrogen covering the copper cooling coils. The stage's temperature stabilized at approximately -80 °C with a relatively "fast" $N_2(g)$ flow rate and a large volume of liquid nitrogen covering the copper cooling coils. However, with a "slower" flow rate and smaller volume of liquid nitrogen, the stage's temperature stabilized at a warmer -15 °C. In both cases, it took about two hours for the stage temperature to stabilize.

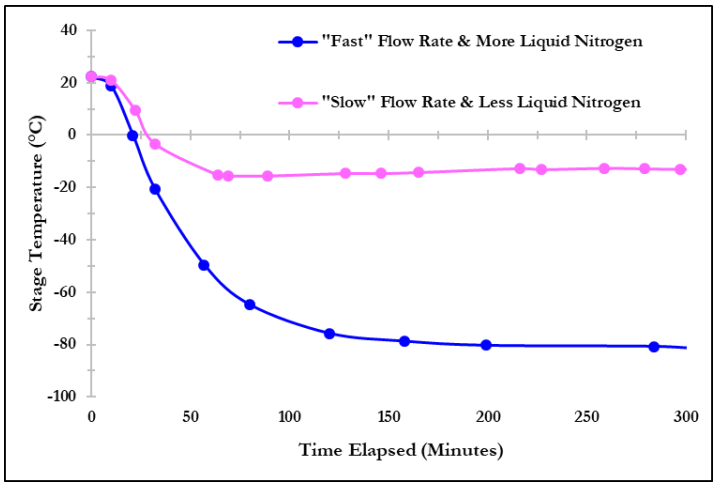

Figure 4.14: Tracking temperature of UHV SPM scan stage during cooling process. "Flow Rate" refers to $N_2(g)$ being released from gas cylinder. "Liquid Nitrogen" refers to the amount of liquid nitrogen covering the copper cooling coils in the styrofoam bucket.

We used plain, cleanly-cleaved HOPG as a test sample to verify that we could operate the microscope at cooler temperatures. As a first pass, we transferred a piece freshly cleaved HOPG

into the UHV chamber while the stage was at room temperature. The HOPG sample rested on the stage as it cooled over the course of two hours and stabilized at -82°C. NCAFM topography images of this cooled HOPG sample are shown in Figure 4.15.

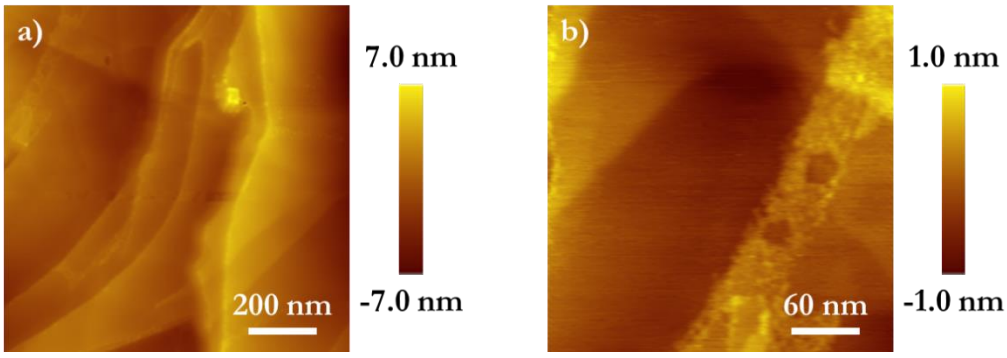

Figure 4.15: NCAFM topography images of HOPG cooled to -82.0 °C. (a) 1.0 μm x 1.0 μm image, taken at a scan rate of 1.0 μm/s. (b) 300 nm x 300 nm image, taken at a scan rate of 0.6 μm/s, within the scan area of (a).

While most of the terraces appear pristine, the step edges appear covered in adsorbed material. This material also clusters on terraces (Figure 4.15 (b)), although it is not widespread enough to cover the entire surface. We assume this is loosely bound material that was introduced as the sample was transferred into the chamber or is material outgassing from the chamber's walls.[30] We suspect that compounds typically found in air (N_2, O_2, H_2O, Ar, CO_2, etc.) are adsorbing to the cooled HOPG sample. We repeated this experiment but waited 2.5 hours before beginning to cool the stage in hopes of allowing the chamber's ion pump to remove any contaminants. However, we still observed material adsorbing to the HOPG surface. This adsorbed contamination could interfere with KPFM measurements, so instead we cooled the sample to a warmer -15 °C; we did not observe any adsorbed contamination on the HOPG surface at this temperature.

With our current method for vapor depositing molecules onto graphite, cooling the samples was unhelpful in slowing the desorption of the bulky substituted azulenes. Two competing processes limit the usefulness of this technique. First, it takes about two hours for the stage's temperature to stabilize which is enough time for most of the bulky molecules to desorb off the graphite surface.

Second, cooling the stage before transferring in the sample introduces contamination that could adsorb to the surface. In this case, contamination adheres to the stage and sample before being eliminated by the ion pump inside the chamber. This is especially problematic if the stage is cooled below -15 °C. Then, in addition to competing with contamination, one still needs to wait for the sample's temperature to stabilize on the cooled stage. If cooling the stage is to be used in the future, a different deposition method needs to be implemented where these samples are not prepared, then introduced to ambient conditions before being transferred into the UHV chamber.

4.5 Conclusions

By placing substituents at strategic locations around azulene's framework, the frontier molecular orbital energy gap can be tuned by independently shifting the energy of either the highest occupied molecular orbital or lowest unoccupied molecular orbital. In principle, this should change the charge transport interaction when these molecules are adsorbed on graphite. Vapor deposition was used to deposit substituted azulenes on graphite. Then, noncontact atomic force microscopy (NCAFM) and Kelvin Probe Force Microscopy (KPFM) were used simultaneously to collect topography and surface potential images of the samples in an ultrahigh vacuum chamber.

Topographical cross sections were used to identify single molecules adsorbed to graphite's terraces. As was observed with azulene (reported in Chapter 3), measured lateral dimensions were an order of magnitude larger than the molecule's true size due to the AFM tip's broad radius. We are unable to see any changes in length or width with substitution because these changes are too small to be resolved with the broad AFM tip. Single molecules had heights consistent with the interlayer spacing of graphite, which suggests that they π-stack flat against the graphite surface. No difference in adsorption behavior was observed with the substituted azulenes compared to unsubstituted azulene.

While topographical measurements for the substituted azulenes were similar to regular azulene, the substituted molecules displayed different relative contact potential differences (CPDs) on graphite. However, the trends in relative CPDs could not be explained using just the integer charge transfer model for physisorbed molecules on metals. Substitution also changes the molecule's dipole moment, as well as the energy of the dopant's frontier molecular orbitals. A polar adsorbent could influence the surface's dipole moment, thereby changing the local doping effect. We hypothesized that a balance between charge transfer, the pillow effect, and the adsorbate's dipole moment is responsible for the shifts in relative CPDs. We carried out a straightforward multiple linear regression to quantify the weighting coefficients for each mechanism. There was no linear correlation when naphthalene was included in the analysis, but a moderate linear correlation ($R^2 = 0.742$) was observed when naphthalene was excluded. The coefficients' magnitude suggest that the pillow effect and charge transfer mechanisms are the main contributors to local surface potential modification, rather than the dopant's native dipole moment. While we can experimentally observe changes in local work functions when different molecules are adsorbed onto a graphite surface, our simple model was not enough to fully explain data trends. Computational studies about adsorption orientation, orbital overlap, and changes in electronic structure upon adsorption would expand our understanding of the experimental trends. This additional information would allow us to more accurately describe each mechanism's contribution to modifying the local work function.

We tried to observe other azulenes, with nonplanar substituents, on graphite, but we were unable to do so because these molecules desorb from the graphite surface in both vacuum and ambient environments. The bulky substituents inhibit the azulene backbone from π-stacking with the graphite lattice, leading to weaker physisorption. Cooling the samples proved to be unhelpful due to two competing factors: loosely bound contamination adsorbs to the sample at temperatures below -15 °C and it takes time for the samples' temperature to stabilize. If our method of vapor

deposition is to be continued, only substituted azulenes with planar substituents should be considered for future experiments.

4.6 References

1. RHK Technology. https://www.rhk-tech.com/ (accessed November 19, 2020).

2. Shevyakov, S. V.; Li, H.; Muthyala, R.; Asato, A. E.; Croney, J. C.; Jameson, D. M.; Liu, R. S. H., Orbital Control of the Color and Excited State Properties of Formylated and Fluorinated Derivatives of Azulene. *The Journal of Physical Chemistry A* **2003,** *107* (18), 3295-3299.

3. Liu, R. S. H., Colorful Azulene and Its Equally Colorful Derivatives. *Journal of Chemical Education* **2002,** *79* (2), 183.

4. Lu, Y.; Lemal, D. M.; Jasinski, J. P., Bond Alternation in Azulenes. *Journal of the American Chemical Society* **2000,** *122* (11), 2440-2445.

5. Novoselov, K. S.; Geim, A. K.; Morozov, S. V.; Jiang, D.; Zhang, Y.; Dubonos, S. V.; Grigorieva, I. V.; Firsov, A. A., Electric Field Effect in Atomically Thin Carbon Films. *Science* **2004,** *306* (5696), 666-669.

6. Barybin Group Research Website. https://barybingroup.ku.edu/ (accessed October 18, 2020).

7. Nanoworld NCHPt AFM Tips. https://www.nanoworld.com/pointprobe-tapping-mode-platinum-coated-afm-tip-nchpt (accessed November 19, 2020).

8. Milde, P.; Porthun, S., Kelvin Probe Force Microscopy with the RHK R9. RHK Technology Inc.: https://www.rhk-tech.com/applications/appnotes/, 2016.

9. Chung, D. D. L., Review Graphite. *Journal of Materials Science* **2002,** *37* (8), 1475-1489.

10. Nanayakkara, S. U.; Cohen, G.; Jiang, C.-S.; Romero, M. J.; Maturova, K.; Al-Jassim, M.; van de Lagemaat, J.; Rosenwaks, Y.; Luther, J. M., Built-in Potential and Charge Distribution within Single Heterostructured Nanorods Measured by Scanning Kelvin Probe Microscopy. *Nano Letters* **2013,** *13* (3), 1278-1284.

11. Leung, C.; Kinns, H.; Hoogenboom, B. W.; Howorka, S.; Mesquida, P., Imaging Surface Charges of Individual Biomolecules. *Nano Letters* **2009,** *9* (7), 2769-2773.

12. Smith, G. J. Nanoscale Manipulation of Surface and Interfaces: Engineering Electrical Properties Through Nanofabrication. Ph.D. Dissertation, University of Kansas, Lawrence, KS, 2012.

13. Shiraishi, M.; Ata, M., Work function of carbon nanotubes. *Carbon* **2001,** *39* (12), 1913-1917.

14. Jain, S. C.; Krishnan, K. S., The thermionic constants of metals and semi-conductors I. Graphite. *Proceedings of the Royal Society of London. Series A. Mathematical and Physical Sciences* **1952,** *213* (1113), 143-157.

15. Hansen, W. N.; Hansen, G. J., Standard reference surfaces for work function measurements in air. *Surface Science* **2001,** *481* (1), 172-184.

16. Lias, S. G., Ionization Energy Evaluation. In *NIST Chemistry Webbook, NIST Standard Reference Database Number 69*, P.J. Linstrom, W.G. Mallard, National Institute of Standards and Technology, Ed. Gaithersburg, MD.

17. Lemal, D. M.; Goldman, G. D., Synthesis of azulene, a blue hydrocarbon. *Journal of Chemical Education* **1988,** *65* (10), 923.

18. Braun, S.; Salaneck, W. R.; Fahlman, M., Energy-Level Alignment at Organic/Metal and Organic/Organic Interfaces. *Advanced Materials* **2009,** *21* (14-15), 1450-1472.

19. Franco-Cañellas, A.; Duhm, S.; Gerlach, A.; Schreiber, F., Binding and electronic level alignment of π-conjugated systems on metals. *Reports on Progress in Physics* **2020,** *83* (6), 066501.

20. Otero, R.; Vázquez de Parga, A. L.; Gallego, J. M., Electronic, structural and chemical effects of charge-transfer at organic/inorganic interfaces. *Surface Science Reports* **2017,** *72* (3), 105-145.

21. MOPAC16. http://openmopac.net/MOPAC2016.html (accessed November 16, 2020).

22. Sauter, E.; Yildirim, C.; Terfort, A.; Zharnikov, M., Adjustment of the Work Function of Pyridine and Pyrimidine Substituted Aromatic Self-Assembled Monolayers by Electron Irradiation. *The Journal of Physical Chemistry C* **2017,** *121* (23), 12834-12841.

23. Asyuda, A.; Gärtner, M.; Wan, X.; Burkhart, I.; Saßmannshausen, T.; Terfort, A.; Zharnikov, M., Self-Assembled Monolayers with Embedded Dipole Moments for Work Function Engineering of Oxide Substrates. *The Journal of Physical Chemistry C* **2020,** *124* (16), 8775-8785.

24. Gärtner, M.; Sauter, E.; Nascimbeni, G.; Wiesner, A.; Kind, M.; Werner, P.; Schuch, C.; Abu-Husein, T.; Asyuda, A.; Bats, J. W.; Bolte, M.; Zojer, E.; Terfort, A.; Zharnikov, M., Self-Assembled Monolayers with Distributed Dipole Moments Originating from Bipyrimidine Units. *The Journal of Physical Chemistry C* **2020,** *124* (1), 504-519.

25. Mysliveček, J.; Stróżecka, A.; Steffl, J.; Sobotík, P.; Ošťádal, I.; Voigtländer, B., Structure of the adatom electron band of the Si(111) - 7 x 7 surface. *Physical Review B* **2006,** *73* (16), 161302.

26. Baumann, S.; Rau, I.; Lutz, C. P.; Heinrich, A. A Boy and His Atom: The World's Smallest Movie. https://www.research.ibm.com/articles/madewithatoms.shtml (accessed November 16, 2020).

27. Eigler, D. M.; Schweizer, E. K., Positioning single atoms with a scanning tunnelling microscope. *Nature* **1990,** *344*, 524+.

28. Crommie, M. F.; Lutz, C. P.; Eigler, D. M., Confinement of Electrons to Quantum Corrals on a Metal Surface. *Science* **1993,** *262* (5131), 218.

29. Bonnell, D. A.; Huey, B. D., Basic Principles of Scanning Probe Microscopy. In *Scanning Probe Microscopy and Spectroscopy: Theory, Techniques, and Applications*, 2nd ed.; Bonnell, D. A., Ed. Wiley-VCH: 2001; pp 7-42.

30. Grinham, R.; Chew, A., A Review of Outgassing and Methods for Its Reduction. *Applied Science and Convergence Technology* **2017,** *26* (5), 95-109.

Chapter 5: Nanolithography on NaCl Resist Layers for Formation of Metal Nanostructures in Harsh Environments

5.1 Abstract

Metallic nanostructures are increasingly useful for plasmonic sensing devices, photodetectors, catalysis, and light-harvesting for energy applications. Organic resist layers, such as self-assembled monolayers (SAMs) or polymers, are commonly used in bottom-up metallic nanostructure fabrication but are not suitable for atomic layer deposition's high temperatures. Furthermore, organic resist layers are difficult to remove from the substrate without exposing the metallic structures to harsh reagents. We aim to create a novel resist layer using sodium chloride (NaCl), and other salt compounds, on Si(111) that can withstand ALD conditions, be patternable using scanning probe lithography, and be removed using a simple solvent wash after metal deposition. Aqueous deposition of NaCl proved to be problematic because NaCl is so soluble in water. Macroscopic coffee-ring features that were too large for AFM imaging and patterning formed locally on the Si(111) surface. Vapor deposition for 30-45 minutes deposited NaCl nanoparticles on the surface in an incomplete layer. Nonetheless, we were able to create recognizable patterns in the samples using scanning probe lithography. We demonstrated that the patterned NaCl-Si(111) samples could be coated in gold using thermal evaporation and withstand that process's vacuum and heat conditions. Any NaCl particles not completely encased in metal could be removed using deionized water, leaving a recognizable imprint in the deposited gold. If a thin, uniform layer of salt could be deposited on a surface it could be used as a viable resist layer for high heat and vacuum metal deposition processes. The work presented in this chapter was ultimately continued by Dr. Sasanka Ulapane, where he used $CaCO_3$ (water insoluble salt) nanoparticles as a patternable resist layer.[1]

5.2 Introduction

There has recently been great emphasis on miniaturizing metallic structures as the demand for smaller electronic devices and the need to conserve expensive metals increases. Metallic nanostructures are useful for plasmonic sensing devices[2-5], surface enhanced Raman spectroscopy (SERS)[6], photodetectors[7], catalysis[8-11], and light-harvesting for energy applications[12-14]. The metallic nanostructure's properties are highly dependent on their chemical identity, size, and shape. Solution-based synthesis of metallic nanoparticles provides well-defined control over the nanostructure's size and shape[15, 16], but lacks the ability to control their placement on a surface. Versatile techniques are required to manufacture small metallic structures, with controlled shape and orientation, on a variety of substrates.

Metal can be deposited on a surface using various techniques such as electrolysis (also known as electroplating)[17], electroless deposition[18, 19], atomic layer deposition (ALD)[20], and thermal evaporation[21]. On a bare substrate, these techniques deposit metal over the entire surface. To create defined metal structures, resist layers can be deposited over the surface and patterned. Where there is resist material, metal is blocked from interacting with the substrate. The resist layer can be removed after metal deposition, leaving the desired metal feature behind on the surface.

Organic materials are commonly used as resist layers in nanofabrication. Some organic molecules can spontaneously form self-assembled monolayers (SAMs) on substrates. The head-group of a molecule chemisorbs to a specific substrate, while intermolecular interactions stabilize the tails, so the molecules stand in an upright orientation on the substrate.[22] This spontaneous process stops once the substrate is covered, therefore SAMs are only one molecule thick.[22] Formation of SAMs requires specific molecule-substrate chemistry. For example, thiol-based molecules specifically bind with gold surfaces[23] and silane-based molecules bind to silicon substrates.[24, 25] Polymer thin films are also used in nanofabrication.[26, 27] Unlike SAMs, organic polymers do not require specific

chemistry to bind to a surface; they can be deposited through solvent dropcasting and subsequent spin-coating.[28]

Some of the resist layer must be removed to expose the underlying substrate for metal deposition. Several techniques have been developed to control the orientation and shape of metal structures on surfaces. Top-down fabrication techniques, such as stencil lithography (also known as shadow mask deposition)[29, 30], microcontact printing[31], and imprint lithography[32, 33] create well-defined metallic structures but are limited to creating features with lateral dimensions of more than a hundred nanometers. Electron-beam lithography[34] can make nanometer-sized features, but requires expensive equipment. Bottom-up fabrication techniques allow for the growth of smaller metal features. Particle lithography[35] methods are an affordable way to pattern large areas of organic resist layers, but the size and shape of the resulting metallic nanostructures are limited by the shape and spacing of the particles. Scanning probe patterning techniques[36], while lacking throughput, allow for precise control over the location and shape of patterns in resist layers.

Extensive work has been done in our research group using atomic force microscopy (AFM) to shave away areas of SAMs[37] and ultimately deposit metal on the exposed substrate using electroless deposition, as shown in Figure 5.1.[38] In this publication, our group used formed well-packed silane SAMs on a silicon substrate.[38] Then, as shown in Figure 5.1(c), scanning probe lithography was used to remove a selective area of the SAM; enough force was applied to the AFM tip to also remove silicon's native oxide layer (SiO_2) and expose the underlying silicon (Si) substrate.[38] Finally, as shown in Figure 5.1(d), electroless deposition was used to spontaneously grow metal (either gold or silver) only in the area with exposed Si.[38] Using scanning probe lithography, in conjunction with a resist layer, allows one to control the placement, size, and shape of metal features grown on the surface.

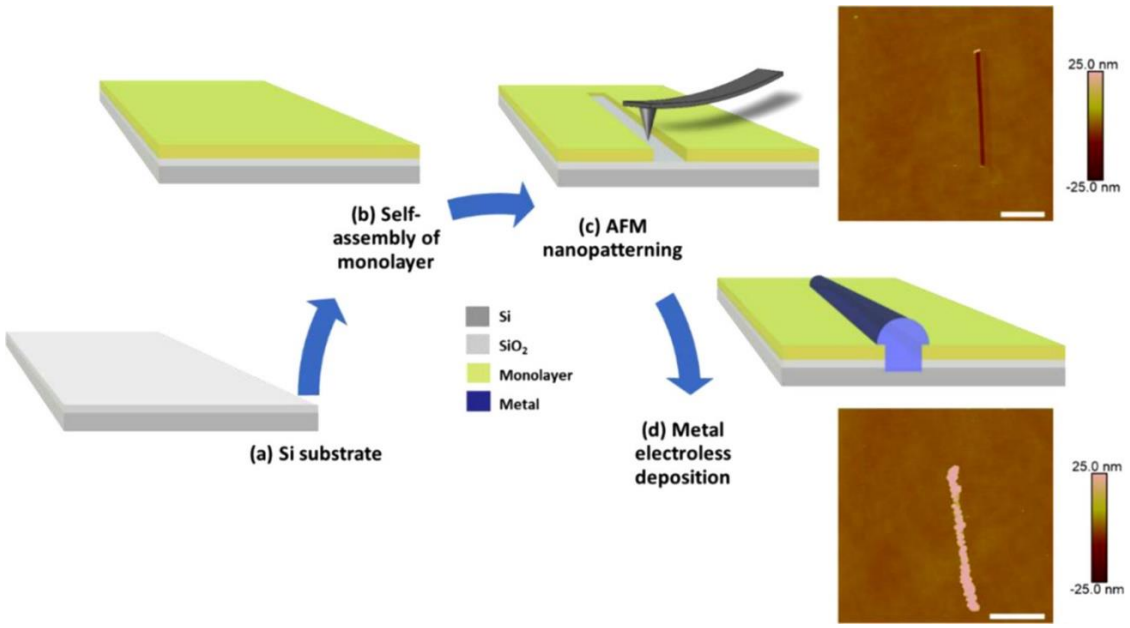

Figure 5.1: Using scanning probe lithography and electroless deposition to grow metallic features with defined shape, size, and orientation on a substrate. (a) Piranha-cleaned silicon (Si) substrate, with native oxide (SiO_2) on surface. (b) Octadecyltrichlorosilane molecules self-assemble into a densely packed monolayer on the SiO_2 surface. (c) Scanning probe lithography is used to remove a selective area of the monolayer and oxide layer, exposing the underlying Si substrate. (d) Electroless deposition is used to spontaneously deposit gold or silver metal on the exposed Si, creating a metal nanowire. No metal is deposited on areas protected by the monolayer. Reprinted with permission from Reference 38. © 2020 American Chemical Society.

While organic-based resist layers have been used as templates for metallic nanostructure growth in solution, they do present some challenges. SAM formation requires specific molecule-substrate chemistry, so SAMs cannot be formed on just any material. It is also difficult to remove any organic material after metal deposition. SAM removal with solution-based methods requires exposure to harsh reagents[39, 40] that can damage the metal nanostructures.[41] Furthermore, organic resist layers are not suitable for every metal deposition method. Atomic layer deposition (ALD) and thermal evaporation requires elevated temperatures and vacuum environments[20] that could cause decomposition of organic molecules.

We are interested in developing a novel resist layer that can be applied to a wide variety of substrates, withstand ALD conditions, and can be removed easily leaving the metal nanostructures intact. Salts are interesting candidates because they are very common and inexpensive. In principle, they can be deposited on any substrate; no specific chemistry is required for salts to adhere on a

surface through physisorption. Salts have very high melting points, so they could withstand the high temperatures in ALD. Many salt compounds are water-soluble; a gentle water soak could remove the salt resist layer without damaging the metal features.

In this chapter, we present a proof of concept experiment using sodium chloride (NaCl) as a potential resist layer on Si(111) substrates. NaCl was used because it is water-soluble and was available in large quantities in our lab. We tested various solvent and vapor deposition methods for depositing NaCl onto Si(111). The surfaces' topographies were mapped using contact atomic force microscopy (AFM). Scanning probe lithography using a stiff AFM tip was attempted on any suitable NaCl-Si(111) samples. Contact AFM was also used to verify that patterns were successfully made on the NaCl-Si(111) samples. Finally, we coated a patterned NaCl-Si(111) sample in gold (Au) using a thermal evaporator. Then, we soaked the Au-NaCl-Si(111) samples in water to test whether we could remove the residual salt from the surface after metal deposition, potentially creating a recognizable metal structure.

5.3 Materials and Methods

5.3.1 Materials

Sodium chloride (NaCl), 30% hydrogen peroxide (H_2O_2), and concentrated sulfuric acid (H_2SO_4) were purchased from Fisher Scientific. Single-sided, polished, boron-doped Si(111) wafers were purchased from Virginia Semiconductor (Fredericksburg, VA). 99.999% gold (Au) shots were purchased from Alpha Aesar.

5.3.2 Piranha-Cleaning Si(111) Substrates

Pieces of Si(111) (about 1 x 1 cm^2) were cut off the main wafer using a diamond scribe. The Si(111) substrates were placed in piranha solution (3:7 mixture of 30% H_2O_2: concentrated H_2SO_4) for about 20 minutes. *Caution: piranha solution is extremely corrosive, and potentially explosive if capped in a*

sealed container. The solution should be handled with caution, using the appropriate personal protective equipment! The piranha solution was made in small quantities, as needed, and neutralized immediately after use. Piranha solution is a common method for cleaning silicon, especially in the semiconductor industry. It is a strong oxidizer that removes any adsorbed organic material and reforms the silicon hydroxide layer on the silicon surface.[40] After piranha cleaning, the silicon surface is hydrophilic.[42] Then the Si(111) substrates were removed from the piranha solution, rinsed profusely with deionized (DI) water, and dried with a gentle flow of $N_2(g)$.

5.3.3 Solvent Deposition of NaCl onto Si(111)

NaCl(aq) solutions in DI water were made at several concentrations: 0.1 M, 0.5 M, 1.0 M, 1.5 M, 2.0 M. A few drops of NaCl(aq) solution were dropcast onto a piranha cleaned Si(111) substrate from a disposable glass pipette. Enough solution was deposited to completely cover the surface without spilling over its edges. We tested three different evaporation techniques:

1. Ambient Evaporation: The samples were left on the benchtop overnight for the water to evaporate ambiently.
2. $N_2(g)$ Drying: The NaCl(aq) solution sat undisturbed for 10 minutes, before a gentle flow of $N_2(g)$ was used to dry the surface.
3. Hot Plate Evaporation: A hot plate was set to a temperature between 50 °C – 80 °C. The hot plate's temperature was monitored with a beaker of water and thermometer. Once the hot plate's temperature stabilized, a piranha-cleaned Si(111) substrate was placed on the hot plate for at least 10 minutes. Then, a few drops of NaCl(aq) were deposited on the hot substrate. The sample was left on the hot plate until the water bubble evaporated.

5.3.4 Vapor Deposition of NaCl onto Si(111)

A 1.0 M NaCl(aq) solution, in a large Erlenmeyer flask, was brought to a rolling boil on a hot plate. An Erlenmeyer flask, rather than a beaker, was used because the relatively small neck focused

the flow of emitting vapor from the boiling solution. Reverse-clamp tweezers, supported with a ring stand and clamp, held a piranha-cleaned Si(111) substrate face down. The sample level with the top of the flask, over the boiling solution (within the emitting vapor cloud). The Si(111) substrate was held over the boiling solution for 30 – 45 minutes. Then, the sample was removed and dried with a gentle stream of $N_2(g)$.

5.3.5 Imaging NaCl – Si(111) Samples with Contact Atomic Force Microscopy

The surface topography of the NaCl – Si(111) samples was mapped using a Digital Instrument Atomic Force Microscope (AFM) with a Nanoscope J Controller, operating in contact mode. A standard silicon nitride tip (NP-S10, k=0.06 N/m) tip from Bruker was used for imaging; the same tip was not used to collect all images. While the scan rate and setpoint varied from image to image, they were generally set between 0.7 – 1.5 Hz and 2.5 – 3.0 V, respectively.

5.3.6 Patterning NaCl-Si(111) Samples with Atomic Force Microscopy

The NaCl - Si(111) samples were patterned with the same Digital Instruments AFM with a Nanoscope J Controller. The AFM still was operated in contact mode, but a Tap300 DLC AFM tip from Budget Sensors was used instead. These Tap300 DLC tips are very stiff (k = 40 N/m) and robust due to their diamond-like carbon (DLC) coating. For patterning, a setpoint of 1.0 V and scan rate between 1.1 – 1.3 Hz was used. The DLC tip was scanned completely over an area at least twice. Later, the same area was imaged in contact mode with the floppier NP-S tip to verify that a pattern was successfully made.

5.3.7 Gold Evaporation onto Patterned NaCl-Si(111) Samples

An Edwards AUTO 306 Vacuum Coater was used to thermally evaporate gold (Au) metal onto the patterned NaCl - Si(111) substrates. The patterned NaCl-Si(111) samples were mounted inside the vacuum chamber, facing down towards a wire basket containing Au shots. The Au was heated once the pressure in the chamber was at or below 5.0×10^{-6} torr. The Au thickness deposited

on the sample's surface was monitored with a quartz crystal microbalance (QCM). 15 nm of Au was deposited on the patterned NaCl – Si(111) substrates, at a rate of 2 – 3 Å/s.

After the gold coating, an optical microscope was used to visually inspect the sample's surfaces; topography images were also captured with contact AFM. Then, the samples were soaked in deionized (DI) $H_2O(l)$ to remove the NaCl.

5.4 Results and Discussion

In this section, we present results in our development of a novel NaCl resist layer on Si(111). First, we optimized deposition conditions by testing solution and vapor deposition methods. Next, we attempted to create patterns on NaCl-Si(111) samples using scanning probe lithography. Finally, we coated the patterned NaCl-Si(111) samples with gold and attempted to remove the NaCl using a water rinse.

5.4.1 Solvent Deposition of NaCl onto Si(111) Results

First, we tried using solvent deposition (also known as dropcasting) to deposit NaCl films onto Si(111). Figure 5.2 shows pictures of how representative dropcasted NaCl-Si(111) samples visually appeared after the water had evaporated. Macroscopic, opaque, white NaCl crystals are adsorbed on the shiny, grey Si(111) substrate. We did vary the concentrations of dropcasted NaCl(aq) solutions, but the amount of salt deposited on the surface did not noticeably change. A summary of solution dropcasting results is listed below.

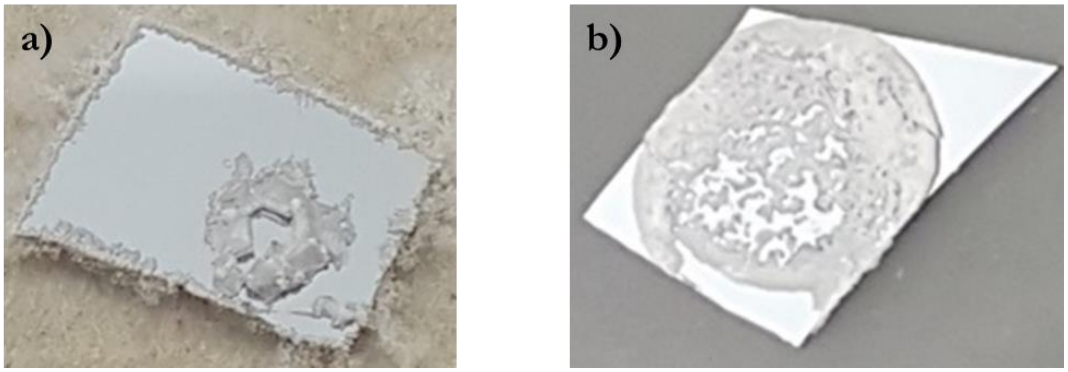

Figure 5.2: Pictures of NaCl on Si(111) deposited via dropcasting. (a) 1.5 M NaCl(aq) dropcasted. Dried using ambient evaporation. (b) 1.0 M NaCl(aq) dropcasted. Dried using hot plate evaporation.

Figure 5.2(a) shows a representative ambient evaporation sample, where a ring of thick, uneven NaCl crystals is visible at the center of the surface. The salt distribution is very uneven and localized. The majority of the Si(111) surface is shiny, indicated that no adsorbed NaCl is present on most of the sample. A little salt is visible around the sample's boundaries because some of the solution seeped over the edges overnight; this was a common occurrence with the ambient evaporation samples. We suspect that air drafts in the fume hood were responsible for disturbing the samples.

No picture was included for the N_2(g) dried samples, because they looked like clean Si(111); no visible salt was deposited using this drying method. Water doesn't evaporate quickly enough for N_2(g) to be an efficient drying method. The gas stream just pushed solution around on the surface until it spilled over the edges.

Figure 5.2(b) shows a representative sample dried using a hot plate. The salt was more evenly distributed across the surface because the water evaporated relatively quickly compared to the other drying methods. The salt was thicker at the edges of the ring and thinner in the middle, while some clean Si(111) areas are visible in the center of the sample. Especially at higher hot plate temperatures (~ 80 °C), water would become trapped under solid salt as NaCl crashed out of solution. When this

trapped water evaporated, it forced some of the solid salt to pop off the surface. This was less of an issue when the hot plate was cooled to 50 °C.

Regardless of drying method, solution deposition is not a viable way to deposit a uniform coating of NaCl onto a substrate. N_2(g) drying did not result in any salt deposition. Ambient and hot plate evaporation resulted in localized, uneven, "coffee-ring" features on the Si(111). Coffee-ring features are deposits that are thicker at the edges, yielding ring-like features on the surface; these are a common problem with dropcasting methods.[43] This effect is thought to be due to an uneven capillary flow that pins colloidal particles towards the edges of the droplets.[44-46]

Salt is very soluble in water: 360 g/L (6.2 M) at 20 °C.[47] With an initial NaCl(aq) concentration around 1.0 M, some of the water can evaporate before NaCl crashes out of solution and deposits on the surface (like leaving a glass of salt water on a windowsill). Dosing the surface with more NaCl(aq) does not smooth the salt distribution; it results in larger, more localized features. Even if the starting concentration of NaCl(aq) was increased to be closer to the solubility limit, too much salt would be on the surface to pattern with AFM. Even at these "low" concentrations the salt features are too large to image with AFM, let alone pattern. For this proof of concept experiment, a method is needed that deposits smaller salt particles on the surface in a thinner, more uniform distribution.

5.4.2 Vapor Deposition of NaCl onto Si(111) & Patterning with Atomic Force Microscopy

Instead of solvent deposition, we opted to try this vapor deposition method in hopes that the vapor from the boiling solution would carry some salt particles out of solution. After using this vapor deposition method, the Si(111) substrates lost their sheen. This indicated that something had adsorbed to the surface, but the features were not visible with the naked eye. Figure 5.3 shows representative AFM topography images of a vapor deposited NaCl – Si(111) sample.

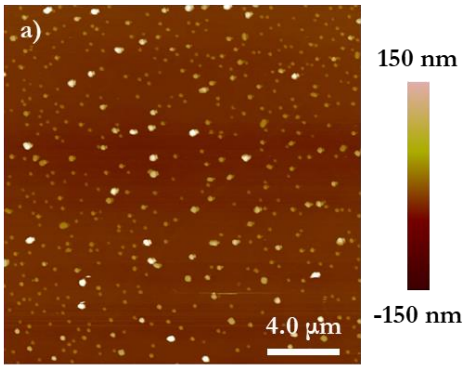

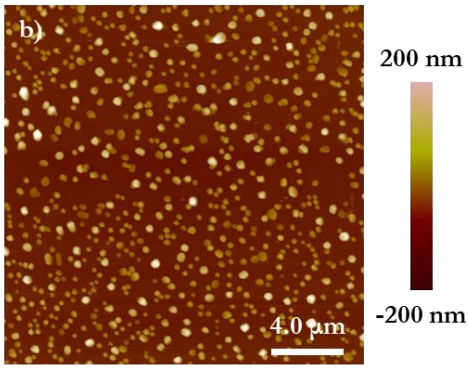

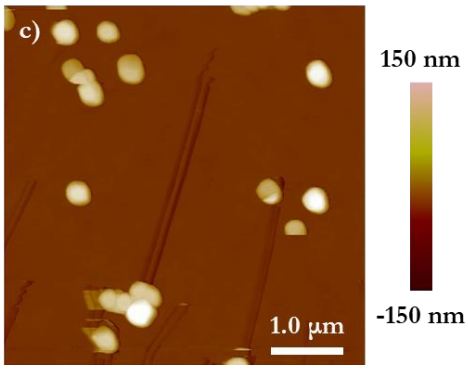

d)	Image (a)	Image (b)	Image (c)
Density (particles/µm²)	0.749	1.395	0.56
Height (nm)	67 ± 33	104 ± 34	106 ± 34
Diameter (nm)	300 ± 83	430 ± 120	350 ± 170

Figure 5.3: AFM topography images of NaCl-Si(111) prepared using 45 minutes of vapor deposition. All images are collected at different locations on the same sample, using a 3.0 V setpoint. (a) and (b) are both 20 x 20 µm² images, taken at a scan rate of 0.74 Hz. (c) is a 5.0 x 5.0 µm² image, taken at a scan rate of 1.17 Hz. (d) Table of particle analysis data for NaCl particles in (a), (b), and (c) obtained from Bruker's Nanoscope Analysis software program (v. 1.4). Averages are reported with their standard deviations.

Unlike the solvent deposition samples, macroscopic salt crystals were not visible on the vapor deposition samples with the naked eye. We were able to successfully images these samples using AFM, which showed NaCl particles distributed over much of the Si(111) surface. We were able to image the same location multiple times, using the NP-S tips in contact mode, without moving the NaCl particles. The built-in particle analysis feature within Bruker's NanoScope Analysis software (version 1.4) was used to analyze the density, height, and diameter of the particles for each AFM image in Figure 5.3; this data is tabulated in Figure 5.3(d). There is a large spread the particle analysis data, but we can characterize these features as NaCl nanoparticles (NPs) due to their dimensions.

The particle density listed in Figure 5.3(d) correlates with what is visually observed in Figure 5.3's AFM images: the NaCl NP coverage varies with scanning location. However, the coverage was on the same order of magnitude; we could find areas with NaCl particles relatively easily. We also conducted vapor deposition trials where we varied the deposition time. Below 30 minutes, not enough NaCl was deposited on the surface; it was difficult to find locations on the surface that had NaCl NPs present. On samples that were prepared using vapor deposition for 45 minutes or longer, we observed some areas with much larger NaCl particles as shown in Figure 5.4. In this case, we saw much larger NaCl particles, yet a smaller particle density, than what was observed in Figure 5.3. The traditional NaCl cubic lattice structure is visible with these particles. Instead of depositing more NaCl NPs on the surface with longer deposition times, we hypothesize that the NaCl aggregated in the presence of the water vapor. The NaCl particles in Figure 5.4 are so large that it would be difficult to manipulate them with a stiff AFM tip.

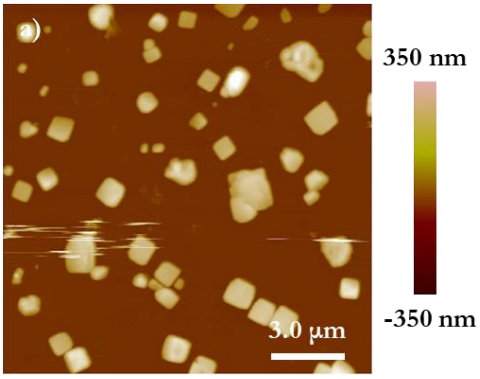

b)

Density (particles/µm²)	0.196
Height (nm)	231 ± 79
Diameter (nm)	850 ± 440

Figure 5.4: NaCl-Si(111) prepared using vapor deposition for 45 minutes. (a) 15 x 15 µm² AFM topography image, taken with a 0.91 Hz scan rate and 3.0 V setpoint. (b) Particle analysis data for (a) obtained from Bruker's Nanoscope Analysis Software (v. 1.4). Averages are reported with their standard deviations.

We decided that 30-45 minutes of vapor deposition provided the ideal NaCl NP size for patterning. Although the Si(111) surface was not completely covered in NaCl, the surface coverage was high enough to test if we were able to pattern. We used a DLC tip, in contact mode, for AFM-based patterning of the NaCl-Si(111) samples. Afterwards we imaged the same location, using a NP-

S tip in contact mode, to verify that the patterning was successful. Figure 5.5 shows AFM images for two square patterns made on different NaCl-Si(111) samples.

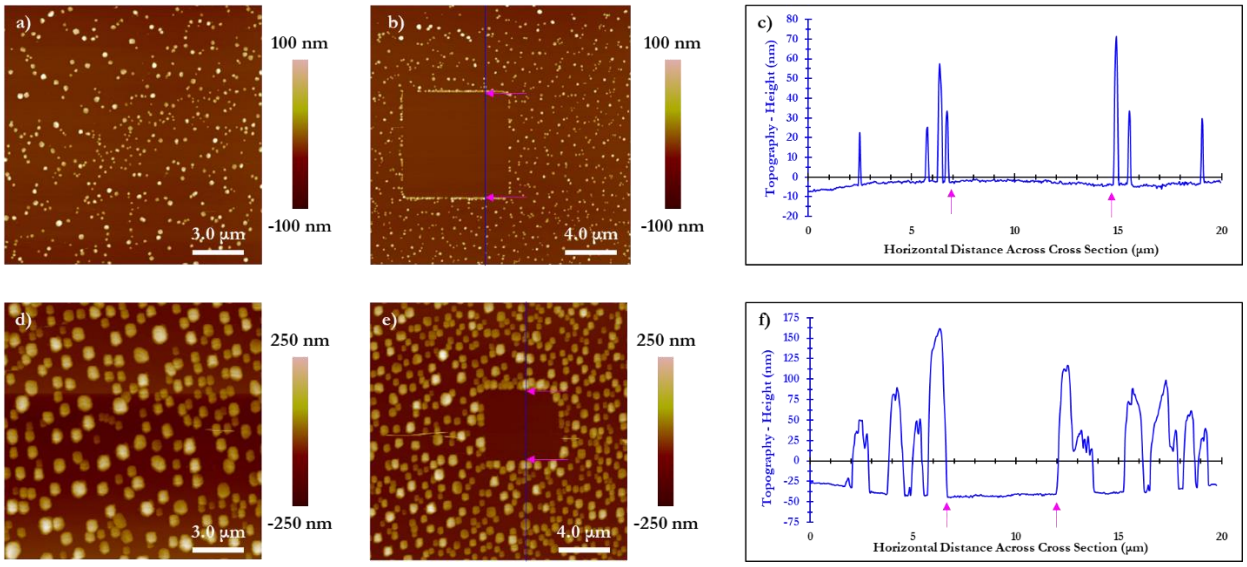

Figure 5.5: Patterning NaCl-Si(111) with AFM. (a) 15 µm x 15 µm topography image, taken with a 0.91 Hz scan rate and 2.5 V setpoint, of a 30 minute vapor deposition sample before patterning. (b) 20 µm x 20 µm topography image, taken with a 1.13 Hz scan rate and 2.5 V setpoint, of an 8 x 8 μm^2 pattern. (c) Cross section through blue line in (b). Pink arrows indicate the pattern's borders in (b) and (c). (d) 15 µm x 15 µm topography image, taken with a 0.87 Hz scan rate and 2.5 V setpoint, of a 45 minute vapor deposition sample before patterning. (e) 20 µm x 20 µm topography image, taken with a 0.85 Hz scan rate and 3.0 V setpoint, of a 5 x 5 μm^2 pattern. (f) Cross section through blue line in (e). Pink arrows indicate the pattern's borders in both (e) and (f).

Figure 5.5(a) shows a 30 minute vapor deposition NaCl-Si(111) sample prior to patterning. Particle analysis calculated the average particle density, height, and diameter to be 1.387 particles/μm^2, 72 ± 16 nm, and 244 ± 56 nm, respectively. As shown in Figure 5.5(b), a DLC tip was used to carve an 8 x 8 μm^2 pattern in the general area that Figure 5.5(a) was captured. The AFM tip moved the NaCl NPs to the edge of the pattern, forming a border, leaving the interior free from particles. The pattern's borders were incomplete, most likely due to the partial NaCl NP surface coverage. Cross sectional analysis, shown in Figure 5.5(c), was used to confirm the pattern's dimensions. The pattern in Figure 5.5(b) was measured to be 7.91 µm x 7.83 µm (horizontal x vertical); this is consistent with the expected dimensions.

Figure 5.5(d) shows a 45 minute vapor deposition NaCl-Si(111) sample prior to patterning. Particle analysis calculated the average particle density, height, and diameter to be 0.68 particles/μm^2, 164 ± 39 nm, and 563 ± 196 nm, respectively. The NaCl NPs in Figure 5.5(d) are significantly larger than those in Figure 5.5(a). Nonetheless, the DLC tip was able to completely clear away a 5 µm x 5 µm pattern in the general vicinity that Figure 5.5(c) was captured. This pattern's borders are still incomplete, some of the edges and corners are less defined. As these larger particles piled up at the edge of the pattern, they became more difficult to manipulate with the tip. The dimensions of this pattern were measured with cross-sectional analysis to be 5.5 µm x 5.2 µm (horizontal x vertical). This is consistent with the expected dimensions, although slightly less accurate than the pattern in Figure 5.5(b).

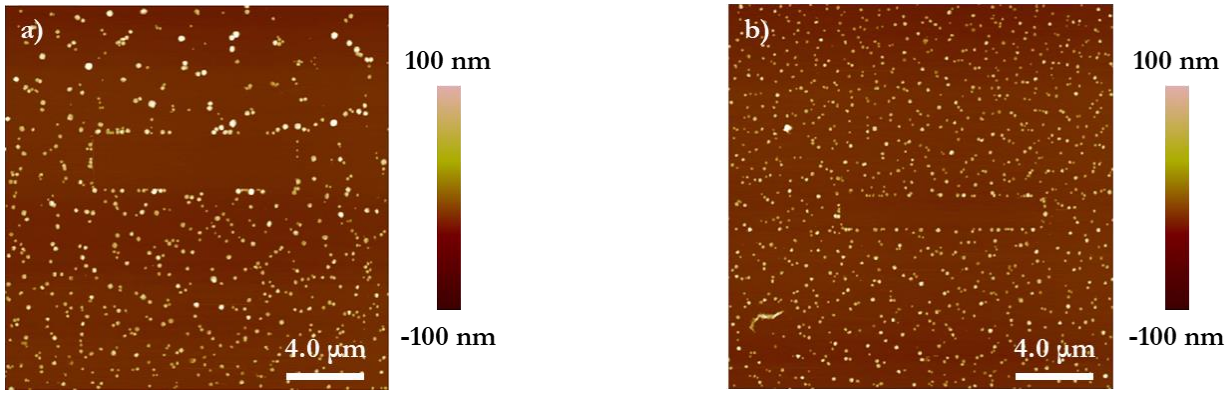

Figure 5.6: Rectangular patterns on NaCl-Si(111). Both AFM topography images are 20 µm x 20 µm and were taken with a 1.13 Hz scan rate and 2.5 V setpoint. (a) 10 µm x 2.5 µm (4:1 aspect ratio) and (b) 10 µm x 1.25 µm (8:1 aspect ratio) patterns.

Square patterns have a 1:1 (length: width) aspect ratio. By changing the aspect ratio during patterning, we could change the shape patterned onto the NaCl-Si(111) samples. Figure 5.6 shows AFM topography images of two rectangular patterns that were made on the same sample shown in Figure 5.5(a). By keeping a constant scan size and varying the aspect ratio on the AFM controller, the vertical scan distance can be manipulated. In Figure 5.6(a), a 10 µm scan size with a 4:1 aspect ratio was used to pattern a 10 µm x 2.5 µm (measured to be 10.4 µm x 2.6 µm) pattern onto the

NaCl-Si(111). In Figure 5.6(b), a 10 μm scan size with a 8:1 aspect ratio was used to pattern a 10 μm x 1.5 μm (measured to be 10.3 μm x 1.4 μm) feature onto the surface. Although the same surface as Figure 5.5(a) was patterned here, the rectangular pattern's borders are less defined than the square pattern in Figure 5.5(b). In the rectangular features, the tip was patterning a smaller area and therefore moving less NaCl particles. Because the moved NaCl NPs form the pattern's borders, the borders are more incomplete if a smaller area is patterned.

We've demonstrated that it is possible to pattern NaCl nanoparticles on a Si(111) surface using scanning probe lithography. Even though the NaCl surface coverage was incomplete, distinguishable patterns could be made so long as scan sizes of several μm^2 are used. We can control pattern's dimensions and shapes by manipulating the AFM's scanning parameters.

5.4.3 Coating NaCl-Si(111) Samples with Gold

Now that distinguishable patterns could be made on NaCl-Si(111), the next step in this proof of concept procedure was to coat the patterned samples in gold metal. Creating metal nanostructures with controlled sizing and surface placement, and high aspect ratios has applications for plasmonic devices.[2] Plasmons are quantized oscillations of free electrons in metals that are resonant with visible to near IR light.[6, 48] Metallic nanostructures with sharp features (high aspect ratios) show localized enhancement of electric fields due to plasmonic effects, which can enhance the detection in Surface Enhanced Raman Spectroscopy (SERS).[6] The plasmon resonance can be tuned by manipulating the metal's shape and aspect ratio.[48, 49] Therefore, plasmonic features can act as sensors because their plasmonic resonance shifts when material adsorbs to the feature. In this work, a patterned NaCl-Si(111) sample was coated in 15 nm of gold using a vacuum evaporator. Figure 5.7 shows AFM images of the sample before and after being coated with gold.

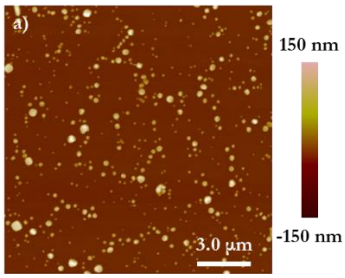

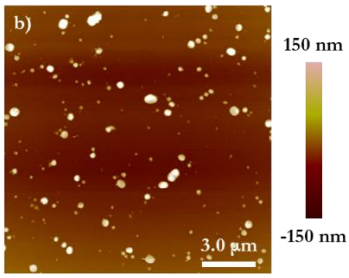

c)	Image (a)	Image (b)
Density (particles/µm²)	1.453	0.413
Height (nm)	74 ± 24	132 ± 42
Diameter (nm)	265 ± 104	316 ± 125

Figure 5.7: AFM topography images of 30 minute vapor deposition NaCl-Si(111) samples (a) before and (b) after being coated with 15 nm of gold in a vacuum evaporator. Both images are 15 µm x 15 µm and were taken with a 1.1 Hz scan rate and 2.5 V setpoint. (c) Particle analysis obtained from Bruker's Nanoscope Analysis (v. 1.4) program for (a) and (b). Averages are reported with their standard deviations.

Figure 5.7(a) shows the topography image of a 30 minute vapor deposition NaCl-Si(111) before being coated with gold. The particle density, height, and diameter are consistent with previous samples that were able to be patterned. Figure 5.7(b) shows the topography image of this sample after it had been coated with 15 nm of gold. The surface topography in Figure 5.7(b) looks so similar to that of 5.7(a) because the entire sample has been coated in the same amount of gold. The height and diameter of the particles in Figure 5.7(b) are larger than in 5.7(a). However, they increased more than expected for a 15 nm coating. Because these images were collected in different locations, the differences in dimensions and particle density could be attributed to the inherent variability in these vapor deposition samples.

However, we had visual confirmation that the sample was coated in gold. A metallic gold shine was visible on the surface with the naked eye. Under an optical microscope, the same metallic gold shine was visible over areas that gold had covered bare Si(111). An opaque, white haze was seen where gold had deposited over NaCl. Large NaCl particles were still visible under the AFM optical microscope. This indicated that the NaCl-Si(111) sample could withstand the vacuum and warm conditions required for vapor deposition of metals.

After verifying that the patterned NaCl-Si(111) substrate was coated in gold, the next step was to soak the sample in water to attempt to remove the salt. Figure 5.8 shows AFM topography images of a pattern before and after being soaked in water.

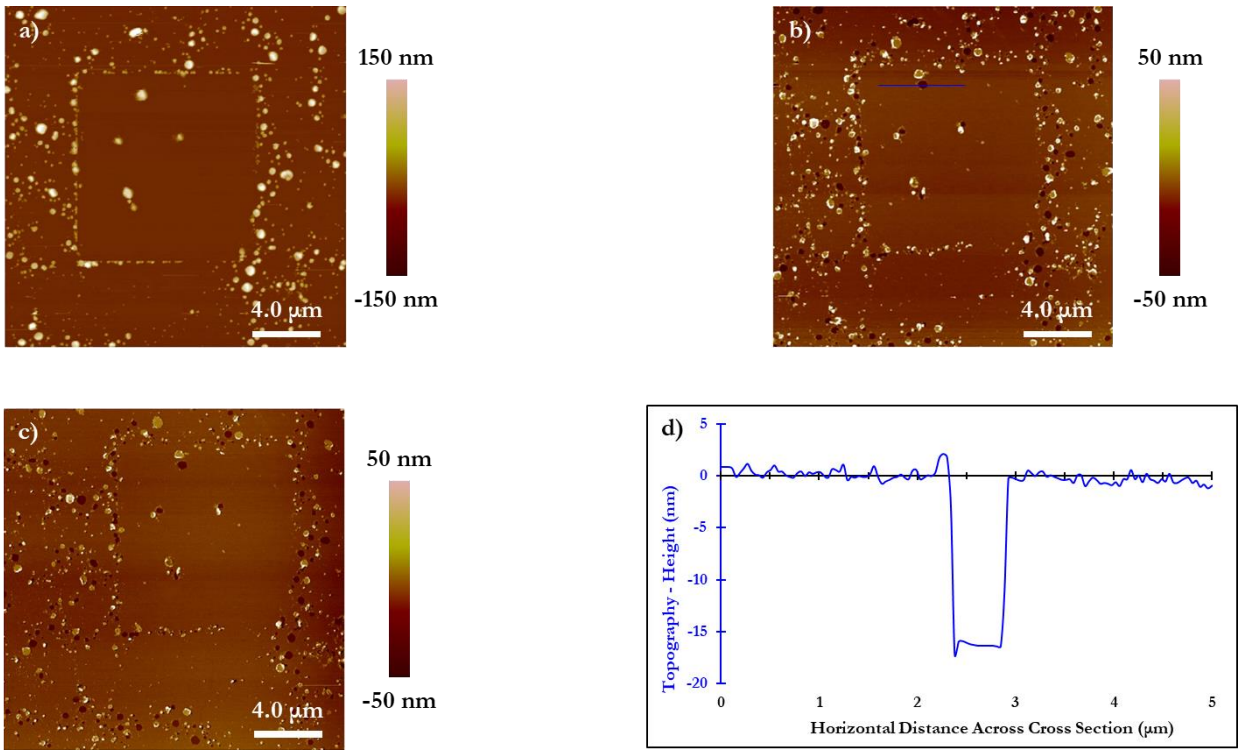

Figure 5.8: Coating patterned NaCl-Si(111) sample in gold and subsequently soaking sample in water. All AFM topography images are 20 µm x 20 µm and were collected with a 1.3 Hz scan rate and 2.5 V setpoint. (a) 10 µm x 10 µm pattern before gold coating (b) Same pattern after coating with 15 nm of gold and soaking in DI water for 20 minutes. (c) Same as (b), but an additional 5 minutes of being sonicated in DI water. (d) Cross section through the blue line in (b).

Figure 5.8(a) shows a 10 µm x 10 µm pattern NaCl-Si(111) pattern after being coated in gold; this pattern was measured to be 10.2 µm x 10.7 µm with cross-sectional analysis. Some NaCl particles were too large to be moved by the DLC tip, but most of the pattern is clean. The pattern's borders are incomplete; this is consistent with previously patterned samples. However, the pattern is distinguishable from the rest of the sample.

After coating the patterned sample with 15 nm of gold, it was soaked in DI water for 20 minutes. Afterwards, a metallic gold shine was still visible on the surface with the naked eye. The white, opaque features disappeared and not many large NaCl particles were visible under an optical microscope. Soaking in water was enough to remove the macroscopic NaCl features from the surface. Figure 5.8(b) shows an AFM image of the pattern after the gold-coating and water soak. While some raised features are still visible, some of the salt particles were removed leaving behind

holes on the surface. A cross section through one of these holes (Figure 5.8(d)) shows its depth to be about 15 nm (consistent with our expected gold thickness). The NaCl NPs dissolved when exposed to water; any gold deposited over these features was free to diffuse away in the solvent. The raised features in Figure 5.8(b) indicate that not all the NaCl dissolved when exposed to water. Even after sonicating the sample in water for an additional 5 minutes (Figure 5.8(c)), no additional salt appears to have dissolved. We suspect that gold completely encased some of the smaller NaCl features, thereby blocking water's access and preventing them from dissolving.

Even though these NaCl-Si(111) samples are not suitable as true resist layers, we did demonstrate that small salt particles could be manipulated with an AFM tip to create a recognizable pattern. So long as the NaCl particles were not completely encased by gold, they could be dissolved with water leaving an imprint of the pattern in the deposited gold. It has been shown that uniform NaCl thin films could be deposited on silicon substrates using thermal evaporation.[50] Further experiments on such a sample would include testing if a uniform layer of NaCl was patternable with AFM, and if the complete resist layer could be removed with water after metal deposition. The work presented here led Dr. Sasanka Ulapane to use insoluble $CaCO_3$ nanoparticles as a patternable resist layer for metallic nanostructure growth.[1]

5.5 Conclusions

A thin layer of salt could act a versatile, robust resist layer that could withstand deposition conditions unsuitable for other commonly used organic resist materials. In principle, salts can be deposited on any substrate because they don't require any substrate-specific chemistry to adhere to the surface through physisorption. Salts can withstand high temperatures that would decompose organic SAM or polymer resists. Many salts are also water-soluble, and therefore could be removed from a surface through a gentle water rinse without damaging the desired metal features. This work

aimed to demonstrate that it was feasible to deposit sodium chloride (NaCl) on a Si(111) substrate, pattern it with scanning probe lithography, coat the sample in gold, and remove the NaCl resist layer with water.

NaCl is so soluble in water that solution deposition proved to be an unusable deposition method. NaCl does not crash out of solution until enough water evaporates and the solubility limit is reached. A macroscopic, uneven, coffee ring structure forms locally on the surface leaving the remainder of the Si(111) substrate clean. The large salt crystals were too large to be imaged, let alone patterned with AFM.

Vapor deposition for 30-45 minutes proved to be a method that deposited NaCl nanoparticles (NPs) over wide areas of the surface that could be imaged with AFM. However, the NaCl NPs did not cover the entire surface. NaCl NPs aggregated in the humid environment with longer deposition times instead of forming a thicker, more uniform coating over the Si(111) substrate. Nevertheless, the partial surface coverage was enough to test if NaCl NPs could be manipulated with scanning probe lithography.

We demonstrated that NaCl NPs could be manipulated with a stiff DLC tip. So long as the NaCl NP surface coverage was high enough, patterns could be created on the surface. They were distinguishable from the background topography, even though their borders were incomplete. The pattern's size and shape could be controlled by the AFM scanning parameters.

Patterned NaCl-Si(111) samples were able to withstand conditions required for thermal evaporation of metals. After coating a patterned NaCl-Si(111) sample in 15 nm thick gold metal, we soaked the samples in deionized water. We confirmed that the larger and macroscopic NaCl particles dissolved in the water, leaving behind an imprint of the pattern in gold. Because NaCl did not cover the entire surface, some of the smaller NaCl particles were fully encased in gold and did not dissolve in water.

These vapor-deposited NaCl-Si(111) samples could never function as a true resist layer because of their incomplete NaCl surface coverage. Nevertheless, this work provided a blueprint for future experiments. If a thin, uniform layer of salt was deposited on a substrate, the salt layer could be patternable with AFM, serve as a true resist layer, and be easily removed with a solvent rinse without disturbing the desired metal features.

Dr. Sasanka Ulapane, a former member of the Berrie group, extended this idea.[1] Instead of using a soluble salt in water, he created a suspension of insoluble calcium carbonate ($CaCO_3$) nanoparticles in water and dropcasted it over various substrates (Si, glass, mica). Because the $CaCO_3$ NPs were insoluble, they deposited in a uniform, 3 μm thick layer on the surface. The weakly interacting nanoparticles were patternable with atomic force microscopy, even when they covered the entire surface. The entire surface of the samples was coated with 30 nm – 50 nm of gold. Water could not be used to remove the $CaCO_3$ resist layer, as $CaCO_3$ is insoluble in water. Instead, he soaked the samples in subsequent solutions of ethylenediaminetetraacetic acid (EDTA) and hydrochloric acid (HCl). EDTA is known to chelate Ca^{2+} ions and metal carbonates tend to react with acids. This lifted the nanoparticle mask and extraneous gold, while leaving the gold patterns undisturbed. More details about Dr. Ulapane's work are written in his doctoral dissertation.[1] We demonstrated that it is possible to use salt compounds as versatile resists that can withstand thermal evaporation conditions, be patterned using scanning probe lithography, and easily removed using solution processing. Increasing the versatility of fabrication methods for small metal features is important for bringing viable, manufacturable nanodevices to market.

5.6 References

1. Ulapane, S. B. Harnessing the Control of Metallic Nanostructures on Interfaces Towards Biosensing, Plasmonics and More. Ph.D. Dissertation, University of Kansas, Lawrence, KS, 2019.

2. Päivänranta, B.; Merbold, H.; Giannini, R.; Büchi, L.; Gorelick, S.; David, C.; Löffler, J. F.; Feurer, T.; Ekinci, Y., High Aspect Ratio Plasmonic Nanostructures for Sensing Applications. *ACS Nano* **2011,** *5* (8), 6374-6382.

3. Chong, X.; Zhang, Y.; Li, E.; Kim, K.-J.; Ohodnicki, P. R.; Chang, C.-h.; Wang, A. X., Surface-Enhanced Infrared Absorption: Pushing the Frontier for On-Chip Gas Sensing. *ACS Sensors* **2018,** *3* (1), 230-238.

4. Deng, W.; Goldys, E. M., Plasmonic Approach to Enhanced Fluorescence for Applications in Biotechnology and the Life Sciences. *Langmuir* **2012,** *28* (27), 10152-10163.

5. Anker, J. N.; Hall, W. P.; Lyandres, O.; Shah, N. C.; Zhao, J.; Van Duyne, R. P., Biosensing with plasmonic nanosensors. *Nature Materials* **2008,** *7* (6), 442-453.

6. Khlebtsov, B. N.; Khanadeev, V. A.; Burov, A. M.; Le Ru, E. C.; Khlebtsov, N. G., Reexamination of Surface-Enhanced Raman Scattering from Gold Nanorods as a Function of Aspect Ratio and Shape. *The Journal of Physical Chemistry C* **2020,** *124* (19), 10647-10658.

7. Alamri, M.; Liu, B.; Sadeghi, S. M.; Ewing, D.; Wilson, A.; Doolin, J. L.; Berrie, C. L.; Wu, J., Graphene/WS2 Nanodisk Van der Waals Heterostructures on Plasmonic Ag Nanoparticle-Embedded Silica Metafilms for High-Performance Photodetectors. *ACS Applied Nano Materials* **2020**.

8. Christopher, P.; Xin, H.; Marimuthu, A.; Linic, S., Singular characteristics and unique chemical bond activation mechanisms of photocatalytic reactions on plasmonic nanostructures. *Nature Materials* **2012,** *11* (12), 1044-1050.

9. Cao, Y.; Yang, Y.; Shan, Y.; Huang, Z., One-Pot and Facile Fabrication of Hierarchical Branched Pt–Cu Nanoparticles as Excellent Electrocatalysts for Direct Methanol Fuel Cells. *ACS Applied Materials & Interfaces* **2016,** *8* (9), 5998-6003.

10. Bai, F.; Sun, Z.; Wu, H.; Haddad, R. E.; Xiao, X.; Fan, H., Templated Photocatalytic Synthesis of Well-Defined Platinum Hollow Nanostructures with Enhanced Catalytic Performance for Methanol Oxidation. *Nano Letters* **2011,** *11* (9), 3759-3762.

11. Hong, C.; Jin, X.; Totleben, J.; Lohrman, J.; Harak, E.; Subramaniam, B.; Chaudhari, R. V.; Ren, S., Graphene oxide stabilized Cu2O for shape selective nanocatalysis. *Journal of Materials Chemistry A* **2014,** *2* (20), 7147-7151.

12. Hildebrandt, N.; Spillmann, C. M.; Algar, W. R.; Pons, T.; Stewart, M. H.; Oh, E.; Susumu, K.; Díaz, S. A.; Delehanty, J. B.; Medintz, I. L., Energy Transfer with

Semiconductor Quantum Dot Bioconjugates: A Versatile Platform for Biosensing, Energy Harvesting, and Other Developing Applications. *Chemical Reviews* **2017,** *117* (2), 536-711.

13. Robel, I.; Subramanian, V.; Kuno, M.; Kamat, P. V., Quantum Dot Solar Cells. Harvesting Light Energy with CdSe Nanocrystals Molecularly Linked to Mesoscopic TiO2 Films. *Journal of the American Chemical Society* **2006,** *128* (7), 2385-2393.

14. Scott, R.; Kirkeminde, A.; Gong, M.; Totleben, J.; Ren, S.; Tuinenga, C.; Lewis, C.; Luo, H.; Higgins, D.; Chikan, V., (Invited) Impact of Indiumand Gallium Doping on the Photovoltaic Performance of CdSe Quantum Dot Hybrid Solar Cells. *ECS Transactions* **2015,** *66* (15), 1-8.

15. Requejo, K. I.; Liopo, A. V.; Derry, P. J.; Zubarev, E. R., Accelerating Gold Nanorod Synthesis with Nanomolar Concentrations of Poly(vinylpyrrolidone). *Langmuir* **2017,** *33* (44), 12681-12688.

16. Roh, J.; Yi, J.; Kim, Y., Rapid, Reversible Preparation of Size-Controllable Silver Nanoplates by Chemical Redox. *Langmuir* **2010,** *26* (14), 11621-11623.

17. Boulanger, C., Thermoelectric Material Electroplating: a Historical Review. *Journal of Electronic Materials* **2010,** *39* (9), 1818-1827.

18. Sullivan, A. M.; Kohl, P. A., The Autocatalytic Deposition of Gold in Nonalkaline, Gold Thiosulfate Electroless Bath. *Journal of The Electrochemical Society* **1995,** *142* (7), 2250-2255.

19. Osaka, T.; Okinaka, Y.; Sasano, J.; Kato, M., Development of new electrolytic and electroless gold plating processes for electronics applications. *Sci Technol Adv Mater* **2006,** *7* (5), 425-437.

20. Hämäläinen, J.; Ritala, M.; Leskelä, M., Atomic Layer Deposition of Noble Metals and Their Oxides. *Chemistry of Materials* **2014,** *26* (1), 786-801.

21. Ludwig, C.; Wochele, J.; Jörimann, U., Measuring Evaporation Rates of Metal Compounds from Solid Samples. *Analytical Chemistry* **2007,** *79* (7), 2992-2996.

22. Schwartz, D. K., Mechanisms and Kinetics of Self-Assembled Monolayer Formation. *Annual Review of Physical Chemistry* **2001,** *52* (1), 107-137.

23. Vericat, C.; Vela, M. E.; Benitez, G. A.; Gago, J. A. M.; Torrelles, X.; Salvarezza, R. C., Surface characterization of sulfur and alkanethiol self-assembled monolayers on Au(111). *Journal of Physics: Condensed Matter* **2006,** *18* (48), R867-R900.

24. Tripp, C. P.; Hair, M. L., An infrared study of the reaction of octadecyltrichlorosilane with silica. *Langmuir* **1992,** *8* (4), 1120-1126.

25. Fadeev, A. Y.; McCarthy, T. J., Trialkylsilane Monolayers Covalently Attached to Silicon Surfaces: Wettability Studies Indicating that Molecular Topography Contributes to Contact Angle Hysteresis. *Langmuir* **1999,** *15* (11), 3759-3766.

26. Aizawa, M.; Buriak, J. M., Block Copolymer Templated Chemistry for the Formation of Metallic Nanoparticle Arrays on Semiconductor Surfaces. *Chemistry of Materials* **2007,** *19* (21), 5090-5101.

27. Aizawa, M.; Buriak, J. M., Block Copolymer-Templated Chemistry on Si, Ge, InP, and GaAs Surfaces. *Journal of the American Chemical Society* **2005,** *127* (25), 8932-8933.

28. Na, J. Y.; Kang, B.; Sin, D. H.; Cho, K.; Park, Y. D., Understanding Solidification of Polythiophene Thin Films during Spin-Coating: Effects of Spin-Coating Time and Processing Additives. *Scientific Reports* **2015,** *5* (1), 13288.

29. Apanius, M.; Kaul, P. B.; Abramson, A. R., Silicon shadow mask fabrication for patterned metal deposition with microscale dimensions using a novel corner compensation scheme. *Sensors and Actuators A: Physical* **2007,** *140* (2), 168-175.

30. Vazquez-Mena, O.; Sannomiya, T.; Villanueva, L. G.; Voros, J.; Brugger, J., Metallic Nanodot Arrays by Stencil Lithography for Plasmonic Biosensing Applications. *ACS Nano* **2011,** *5* (2), 844-853.

31. Wendeln, C.; Ravoo, B. J., Surface Patterning by Microcontact Chemistry. *Langmuir* **2012,** *28* (13), 5527-5538.

32. Lou, Q.; Shipp, D. A., Imprint Lithography with Degradable Elastomeric Polyanhydrides. *ACS Applied Materials & Interfaces* **2012,** *4* (9), 4457-4460.

33. Liu, J.; Xu, G.; Rochford, C.; Lu, R.; Wu, J.; Edwards, C. M.; Berrie, C. L.; Chen, Z.; Maroni, V. A., Doped Graphene Nanohole Arrays for Flexible Transparent Conductors. *Applied Physics Letters* **2011,** *99*.

34. Chen, Y., Nanofabrication by electron beam lithography and its applications: A review. *Microelectronic Engineering* **2015,** *135*, 57-72.

35. Ulapane, S. B.; Kamathewatta, N. J. B.; Borkowski, A. K.; Steuart, S. J.; Berrie, C. L., Periodic Silver and Gold Nanodot Array Fabrication on Nanosphere Lithography-Based Patterns Using Electroless Deposition. *The Journal of Physical Chemistry C* **2020**.

36. Liu, G.-Y.; Xu, S.; Qian, Y., Nanofabrication of Self-Assembled Monolayers Using Scanning Probe Lithography. *Accounts of Chemical Research* **2000,** *33* (7), 457-466.

37. Headrick, J. E.; Armstrong, M.; Cratty, J.; Hammond, S.; Sheriff, B. A.; Berrie, C. L., Nanoscale Patterning of Alkyl Monolayers on Silicon Using the Atomic Force Microscope. *Langmuir* **2005,** *21* (9), 4117-4122.

38. Edwards, C. M.; Ulapane, S. B.; Kamathewatta, N. J. B.; Ashberry, H. M.; Berrie, C. L., Fabrication and Growth Control of Metal Nanostructures through Exploration of Atomic Force Microscopy-Based Patterning and Electroless Deposition Conditions. *The Journal of Physical Chemistry C* **2020,** *124* (46), 25588-25601.

39. Yuan, M.; Zhan, S.; Zhou, X.; Liu, Y.; Feng, L.; Lin, Y.; Zhang, Z.; Hu, J., A Method for Removing Self-Assembled Monolayers on Gold. *Langmuir* **2008,** *24* (16), 8707-8710.

40. Frantz, P.; Granick, S., Surface preparation of silicon for polymer adsorption studies. *Langmuir* **1992,** *8* (4), 1176-1182.

41. Guo, L.-H.; Facci, J. S.; McLendon, G.; Mosher, R., Effect of Gold Topography and Surface Pretreatment on the Self-Assembly of Alkanethiol Monolayers. *Langmuir* **1994,** *10* (12), 4588-4593.

42. Lee, A. W. H.; Gates, B. D., Covalent Surface Modification of Silicon Oxides with Alcohols in Polar Aprotic Solvents. *Langmuir* **2017,** *33* (35), 8707-8715.

43. Deegan, R. D.; Bakajin, O.; Dupont, T. F.; Huber, G.; Nagel, S. R.; Witten, T. A., Contact line deposits in an evaporating drop. *Physical Review E* **2000,** *62* (1), 756-765.

44. Crivoi, A.; Duan, F., Elimination of the Coffee-Ring Effect by Promoting Particle Adsorption and Long-Range Interaction. *Langmuir* **2013,** *29* (39), 12067-12074.

45. Sun, J.; Bao, B.; He, M.; Zhou, H.; Song, Y., Recent Advances in Controlling the Depositing Morphologies of Inkjet Droplets. *ACS Applied Materials & Interfaces* **2015,** *7* (51), 28086-28099.

46. Al-Milaji, K. N.; Zhao, H., New Perspective of Mitigating the Coffee-Ring Effect: Interfacial Assembly. *The Journal of Physical Chemistry C* **2019,** *123* (19), 12029-12041.

47. Fisher Scientific Sodium Chloride Material Safety Data Sheet. https://fscimage.fishersci.com/msds/21105.htm (accessed November 16, 2020).

48. El-Sayed, M. A., Some Interesting Properties of Metals Confined in Time and Nanometer Space of Different Shapes. *Accounts of Chemical Research* **2001,** *34* (4), 257-264.

49. Khan, A. U.; Zhao, S.; Liu, G., Key Parameter Controlling the Sensitivity of Plasmonic Metal Nanoparticles: Aspect Ratio. *The Journal of Physical Chemistry C* **2016,** *120* (34), 19353-19364.

50. Lee, D. K.; Kim, S.; Oh, S.; Choi, J.-Y.; Lee, J.-L.; Yu, H. K., Water-Soluble Epitaxial NaCl Thin Film for Fabrication of Flexible Devices. *Scientific Reports* **2017,** *7* (1), 8716.

Chapter 6: Conclusions and Future Directions

6.1 Overview

The research presented in this dissertation is focused on understanding and manipulating nanoscale properties at interfaces. The nanoscience field has matured from its original focus of synthesizing and measuring properties of novel, isolated nanomaterials to one that is incorporating nanostructures into useful devices for energy and sensing applications. The nanomaterials' behavior can be altered when in contact, or combined, with other materials. Locally probing and controlling nanoscale interactions is essential for bringing practical nanomaterial devices to market. This dissertation's work is centered on two materials of interest for nanoscale applications: graphene and metal nanostructures.

Graphene is a material that, while interesting for a wide variety of uses, must be modified to work for any niche application. Pure graphene is a "zero bandgap semiconductor", but its unique electronic band structure means it can be doped to induce either metallic or semiconductor behavior. Graphene doping has been extensively demonstrated, but most studies are bulk measurements and lack local information about how dopants modify the work function. We proposed using tunable, azulene-based molecules as physisorbed dopants for graphene. In our work, we used highly ordered pyrolytic graphite (HOPG) substrates as a model for graphene. Graphene and graphite share similar properties, but graphite substrates are more consistent and reproducible. Using HOPG substrates allowed for reliable comparisons of dopants' behaviors across multiple samples. In Chapters 3 and 4, we used noncontact atomic force microscopy (NCAFM) and Kelvin probe force microscopy (KPFM) to correlate local changes in graphite's work function with the topography of adsorbed dopants.

Plasmonic sensors require metallic nanostructures with well-defined shapes, placement, and orientation on an interface. Bottom-up fabrication methods for metallic nanostructures use organic

resist layers that are limited for use on certain substrates. Self-assembled monolayers (SAMs) require a specific substrate on which to chemisorb. SAMs, and organic polymers, require harsh reagents to remove them from a surface; such reagents can damage the desired metal structures. Furthermore, organic resist layers cannot withstand the high temperatures required for atomic layer deposition (ALD) metal growth. In Chapter 5, we developed a novel salt-based resist layer for metal nanostructure growth that is more versatile than organic resist layers. Conclusions and a brief discussion of possible future directions are the focus of the remainder of this chapter.

6.2 Altering Graphite's Local Surface Potential with Azulene-Based Dopants

Graphene has been the focus of dedicated research towards tailoring its unique electronic properties for use in applications such as photovoltaics, batteries, catalysis, and sensors. Although doping of graphene is extensively demonstrated, most doping investigations rely on bulk measurements. A more local understanding of how dopants interact with the surface and modify its local surface potential is key to designing adsorbants that can control the doping effect's direction and magnitude.

In the work presented in Chapters 3 and 4, we proposed using azulene-based molecules as novel dopants for graphene. Azulene is a planar, conjugated ring system that can π-stack with the graphene lattice without lowering its native conductivity. Most importantly, azulene has a complimentary frontier molecular orbital (FMO) density that allows the energy of the highest occupied molecular orbital (HOMO) or lowest unoccupied molecular orbital (LUMO) to be selectively tuned via substitution.[1, 2] By tuning the interaction between the dopant's frontier molecular orbitals and the substrate's Fermi level, we expected to see a change in the local doping effect. Most literature exploring how to tune a surface's local work function use chemisorbed dopants. But, azulene's unique FMO distribution presents a systematic way to modify a surface's

local work function through physisorption. In all work presented here, HOPG was used as a substrate instead of graphene. HOPG and graphene have similar chemical and electronic properties, but graphite samples are more reproducible. Graphene, being only a single layer thick, is easily modified by its supporting substrate.[3] Graphite substrates are commercially available, and their surface can be cleanly regenerated using mechanical cleaving. Using graphite substrates allowed for dependable data comparisons between multiple molecules and samples.

Samples were imaged using scanning probe microscopy in an ultrahigh vacuum chamber. Noncontact atomic force microscopy (NCAFM) and Kelvin probe force microscopy (KPFM) were operated simultaneously to obtain maps of local topography and surface potential of these azulene-based molecules on graphite. Topographical maps were used to study the orientation of isolated, adsorbed molecules on the graphite surface. KPFM maps surface potential, which is directly related to a sample's local work function. KPFM is not a commonly used scanning probe technique, but there are examples in literature where it has been used to study relatively large features of densely packed self-assembled monolayers (SAMs)[4-9], large biomolecules[10], or metal nanoparticles[11, 12]. Here, we used KPFM to map local surface potential modifications of small, isolated, physisorbed molecules. The surface potential images were used to correlate local contrast with topographical features in order to quantify the doping effect's lateral distribution on the surface. By comparing measured relative contact potential differences (CPD) for different substituted azulenes on HOPG, we also aimed to explore the different potential mechanisms responsible for the doping effect of these physisorbed molecules.

Using NCAFM and KPFM to map the topography and surface potential of samples, we aimed to answer several questions about isolated azulene-based molecules adsorbed on graphite. What is the best method to deposit azulene-based molecules onto the surface? How do the molecules orient themselves on the surface? Do azulenes induce a change in the local surface

potential of graphite? If so, how far does this doping effect extend laterally on the surface? Does the magnitude or direction of the local surface potential modification change when different substituted azulenes are adsorbed on graphite? Do these changes correlate to shifts in the energy of the azulene's frontier molecular orbitals?

To begin, we optimized deposition procedures using unsubstituted azulene. Solvent deposition was problematic for several reasons. First, solvent allowed molecules to diffuse across the surface and preferentially adsorb to graphite's step edges. We preferred to have molecules adsorb to graphite's terraces because the step edges are oxidized and chemically distinct from the terraces. Comparing data for molecules on the terraces would be more consistent and a closer model to the dopant's interaction with graphene. Second, it was difficult to control the amount of azulene deposited on the surface. Third, solvent contamination and damage to the substrate were also persistent issues. Vapor deposition was determined to be the cleanest, most reliable method for depositing azulene molecules on graphite. This technique was subsequently used to deposit other substituted azulenes on graphite.

Topography cross-sectional analysis was used to identify single molecules adsorbed to graphite's terraces. Single molecules had heights consistent with the interlayer spacing of graphite, suggesting that they adsorb flat to the graphite lattice through π-stacking interactions. In all cases, the measured lateral dimensions were larger than the molecule's true size by an order of magnitude due to convolution from the broad AFM tip. For this reason, we were unable to quantify any changes in the dopant's lateral dimensions with substitution on the azulene framework because the changes were too small to resolve.

While topographical measurements for the substituted azulenes were consistent, we were able to resolve differences in the local contact potential difference (CPD) when different molecules were adsorbed to the graphite. Therefore, changing the azulene-based molecule adsorbed on the

surface changed the effect on graphite's local work function. In all cases, the local graphite doping effect was confined to the domains of where the molecule was adsorbed; this did not change when substituents were added to the azulene backbone. However, the trends in CPDs could not be explained with the integer charge transfer model alone. All the molecules studied were predicted to act as p-type dopants on graphite, based on the relative energies of the azulenes' frontier molecular orbitals and graphite's Fermi level. The added substituents did not shift azulene's FMOs enough to change that prediction. Substitution on the azulene framework also changed the molecule's dipole moment in addition to its frontier molecular orbital energy gap. Any modifications to the surface dipole moment through the substrate's interaction with the dopant, be it due to the pillow effect or polar adsorbants, would change the local work function. A simple multiple linear regression showed moderate linear correlation between the measured CPDs and three doping mechanisms when naphthalene was excluded from the analysis. The energy level alignment between the dopant and substrate clearly plays a role in the observed local doping behavior, but it is not the only contribution. Our simple model was not enough to fully describe the trends in measured CPDs..

To add to our knowledge of the interplay between the pillow effect, charge transfer, and surface dipole modification mechanisms, we attempted to study additional substituted azulenes on graphite. These particular molecules were nonplanar, and we were unable to image them on the surface. Bulky substituents inhibit the azulene backbone from π-stacking with the graphite lattice, leading to weaker physisorption. These nonplanar molecules desorbed off the graphite in both vacuum and ambient environments, so we were unable to image them on the surface. Cooling the sample proved problematic due to loosely bound contamination and the amount of time it took for the sample's temperature to stabilize. Potential future work to expand our knowledge about the mechanistic contributions to the local doping effect is discussed later in this section.

This work was able to locally map how a small, isolated, physisorbed molecule affects a surface's local work function. We observed that the dopant's effect is very localized to where the dopant is adsorbed, and this was not affected by substituting the parent molecule. Distinct differences in local contrast are observed for different molecules, which suggests that there is a critical relationship between the molecular structure and the doping effect. However, this relationship is not straightforward. Additional research could expand our understanding of how the balance between the pillow effect, charge transfer, and surface dipole modification dictates changes in the local work function.

Additional planar, substituted azulenes should be investigated to expand our library of azulene-based dopants. 2,6-dicyanoazulene would be particularly interesting to image on the graphite surface. The placement of the cyano-functionalities cancels out their individual dipole moments; 2,6-dicyanoazulene should have the same dipole moment as unsubstituted azulene. While that molecule's overall dipole moment doesn't change, the energy of azulene's LUMO is selectively modified. It would be interesting to see if that molecule has a large effect on graphite's local work function.

Scanning tunneling microscopy (STM) methods could be used on these conductive samples to corroborate our KPFM measurements. In $\frac{dI}{dV}$ spectroscopy, plotting the change in current with applied voltage as a function of the applied voltage, is directly related to the local density of states.[13] Therefore, one could extract spatial information about how the substrate's Dirac point shifts based on where the tip is located.[14, 15] With $\frac{dI}{dz}$ spectroscopy, the change in current with respect to tip-sample distance is directly related to the tip-sample barrier height.[13] This barrier height is thought to be linked to the sample's local work function.[16, 17] STM tips, especially those produced from electrochemical etching, are sharper than the metal-coated probes used for KPFM in this work.[18]

Using STM would potentially have a resolution advantage over AFM-based techniques. Because STM is a scanning probe technique, these local spectroscopic measurements could be compared with the shifts in local work function obtained from KPFM.

Other techniques could provide structural information about how these dopants adhere to graphite. Because graphene and graphite are Raman active, tip enhanced Raman spectroscopy (TERS) could provide additional, local, characterization of doping.[19, 20] The ratio of peak intensities (I_D/I_G) of graphene's D peak (1350 cm^{-1}) and its G peak (1580 cm^{-1}) is used to characterize defects on the surface; and differences in dopant-induced modification on the graphene surface would cause (I_D/I_G) to change.

Multiple linear regression was used to show the correlation between the measured CPDs and contributions from the pillow effect, charge transfer, and surface dipole modification mechanisms. This regression did show moderate linear correlation between the local doping effect and these mechanisms, but the correlation could be improved. Previous studies have used these three ideas to describe the contributions to changes in the work function, but our results suggest that this is not sufficient. Computational studies could add insight to our experimental data to completely describe the doping process. For example, density functional theory (DFT) calculations have shown how graphite's bandgap changes based on the structure and orientation of molecules adsorbed to its surface.[21, 22] Modeling how adsorption orientation, interaction strength, and electronic structure changes when using different substituted azulenes as dopants would allow us to more accurately describe, and ultimately predict, the role that these mechanisms play in the local doping effect.

Most importantly, these azulene-based dopants should be deposited onto graphene. Debate in the literature continues about graphene's true work function, but it generally thought to be lower than graphite's by about 0.3 eV.[23] It would be interesting to observe if the Fermi level shift between graphite and graphene impacts the local contact potential differences of the adsorbed azulene

derivatives. Evidence exists that graphene's supporting substrate also modifies its work function[3]; that contribution cannot be ignored when mapping relative effects of adsorbed dopants on the local work function.

6.3 Nanolithography on NaCl Resist Layers for Formation of Metal Nanostructures

Fabricating high aspect ratio metallic nanostructures directly on a surface has applications for plasmonic sensing devices, catalysis, and photovoltaics. Organic resist layers, such as self-assembled monolayers (SAMs) and polymers, have been patterned using lithographic techniques. Then, metal nanostructures are grown on the exposed substrate using solvent-based reactions such as electroless deposition. However, organic resist layers are not suitable for every metal deposition technique. Organic resists would decompose in the high temperature and low-pressure environment required for atomic layer deposition (ALD). In addition, removing organic resists requires exposing the metal nanostructures to harsh, potentially damaging reagents. SAMs can only chemisorb to certain substrates, which limits their widespread use. We aimed to create a novel resist layer using sodium chloride (NaCl) on Si(111) that would be a more versatile protective coating for high temperature, bottom-up metal nanostructure fabrication. In principle, this salt resist layer could withstand ALD conditions, be patternable using scanning probe lithography, and be removed using a simple solvent wash after metal deposition.

Because NaCl is so soluble in water, solvent deposition of salt onto the Si(111) substrate proved impractical. NaCl formed macroscopic coffee-ring features locally on the surface that were too large to pattern or image with atomic force microscopy (AFM). Vapor deposition, from a boiling salt solution, deposited NaCl nanoparticles onto the Si(111) surface. Although the NaCl coverage on the substrate was incomplete, we were able to create recognizable patterns on the samples using AFM. The pattern's shape and dimensions can be controlled by modifying the AFM scanning

parameters. We demonstrated that the patterned NaCl-Si(111) samples could be coated in gold via thermal evaporation and survive that method's vacuum and heat conditions. Any NaCl nanoparticles not totally encased with gold were able to be removed by soaking the sample in deionized water. A recognizable imprint was left behind in the deposited gold metal.

This work was continued by Dr. Sasanka Ulapane, a graduate of our research group.[24] He created a suspension of insoluble calcium carbonate ($CaCO_3$) nanoparticles in water. Because of the nanoparticle's insolubility, they were able to be dropcasted in a uniform layer onto a wide variety of substrates. The weakly interacting nanoparticles were patternable using scanning probe lithography. The patterned samples also withstood a gold coating via thermal evaporation. A water rinse would not remove the $CaCO_3$ resist layer due to insolubility. Instead, solutions of ethylenediaminetetraacetic acid (EDTA) and hydrochloric acid (HCl) were used to remove the nanoparticle mask without damaging the gold structures.

If a uniform layer of NaCl on a surface could be achieved, that would greatly improve its viability as a true resist layer. It has been shown that uniform NaCl layers can be deposited on silicon using thermal evaporation.[25] Continuing work should be done to see if NaCl could be deposited on other substrates in this manner. Scanning probe lithography would have to be optimized on a sample with a continuous NaCl film, due to the relatively strong interactions between compacted salt crystals. The NaCl crystals within the continuous film need to be small enough to be manipulated by an AFM tip for patterning. Not only are smaller particles easier to manipulate with an AFM probe, as demonstrated with Dr. Sasanka Ulapane's calcium carbonate films, they result in more defined patterns.[24] Then, we would have to test if a continuous NaCl film could be removed with a water soak after being coated in gold. Further characterization on the resulting metal structures would verify their conductivity using a four-point probe method.[26, 27]

6.4 Final Statement

The work in this dissertation focuses on understanding, and manipulating, local modifications at interfaces. Chapter 3 and 4 used scanning probe microscopy to study the organization of physisorbed dopants on a substrate on the molecular level. This work used Kelvin probe force microscopy to successfully map local surface potential of isolated, small, physisorbed organic molecules, a system not yet studied with this technique. The knowledge obtained about the dopant's adsorption behavior on the surface, from both topography and surface potential images, illustrates the critical relationship between a dopant's structure and its local effect on the substrate. Our work aimed to weight the previously studied doping mechanisms for physisorbed molecules and found that a straightforward linear fit was not enough to fully describe the molecules' effects on the local work function. This research advanced the techniques required to locally probe isolated, physisorbed molecules' behavior on surfaces. And, it also provided important information to consider for designing adsorbants that can systematically tune a substrate's work function through physisorption. The knowledge obtained in our idealized, ultrahigh vacuum environment can be extended to ambient conditions. This work is important as two-dimensional materials[28] such as graphene[29], molybdenum disulfide (MoS_2)[30], and tungsten disulfide (WS_2)[29] are incorporated into functional devices.

Chapter 5 focused on developing a novel salt-based resist layer for bottom-up metal structure growth. The work expands the versatility of metal nanostructure fabrication. Salt-based resist layers can be deposited on, and physisorb to, any desired substrate. They can withstand high-temperature conditions required for thermal evaporation and atomic layer deposition (ALD) techniques. And, salt resist layers are relatively easy to remove from the surface without damaging the desired metal features. This research makes it easier to grow metallic features with controlled

orientation, placement, and size on a variety of substrates, which is crucial for plasmonic sensor development.

Nanoscience, as a broad field, has matured from focusing on the properties of isolated nanomaterials to incorporating nanostructures together to create useful devices. Locally probing and controlling interactions at the nanoscale is crucial to understanding how heterostructures behave and is necessary so nanodevices can be rapidly engineered. We hope that our work proves useful for incorporating nanomaterials into viable, practical, and manufacturable devices.

6.5 References

1. Shevyakov, S. V.; Li, H.; Muthyala, R.; Asato, A. E.; Croney, J. C.; Jameson, D. M.; Liu, R. S. H., Orbital Control of the Color and Excited State Properties of Formylated and Fluorinated Derivatives of Azulene. *The Journal of Physical Chemistry A* **2003,** *107* (18), 3295-3299.

2. Liu, R. S. H., Colorful Azulene and Its Equally Colorful Derivatives. *Journal of Chemical Education* **2002,** *79* (2), 183.

3. Zhou, S. Y.; Gweon, G. H.; Fedorov, A. V.; First, P. N.; de Heer, W. A.; Lee, D. H.; Guinea, F.; Castro Neto, A. H.; Lanzara, A., Substrate-induced bandgap opening in epitaxial graphene. *Nature Materials* **2007,** *6* (10), 770-775.

4. Sauter, E.; Yildirim, C.; Terfort, A.; Zharnikov, M., Adjustment of the Work Function of Pyridine and Pyrimidine Substituted Aromatic Self-Assembled Monolayers by Electron Irradiation. *The Journal of Physical Chemistry C* **2017,** *121* (23), 12834-12841.

5. Asyuda, A.; Gärtner, M.; Wan, X.; Burkhart, I.; Saßmannshausen, T.; Terfort, A.; Zharnikov, M., Self-Assembled Monolayers with Embedded Dipole Moments for Work Function Engineering of Oxide Substrates. *The Journal of Physical Chemistry C* **2020,** *124* (16), 8775-8785.

6. Gärtner, M.; Sauter, E.; Nascimbeni, G.; Wiesner, A.; Kind, M.; Werner, P.; Schuch, C.; Abu-Husein, T.; Asyuda, A.; Bats, J. W.; Bolte, M.; Zojer, E.; Terfort, A.; Zharnikov, M., Self-Assembled Monolayers with Distributed Dipole Moments Originating from Bipyrimidine Units. *The Journal of Physical Chemistry C* **2020,** *124* (1), 504-519.

7. Zerweck, U.; Loppacher, C.; Otto, T.; Grafström, S.; Eng, L. M., Kelvin probe force microscopy of C60 on metal substrates: towards molecular resolution. *Nanotechnology* **2007,** *18* (8), 084006.

8. Campiglio, P.; Campione, M.; Sassella, A., Kelvin Probe Force Microscopy Characterization of Self-Assembled Monolayers on Metals Deposited with Dip-Pen Nanolithography. *The Journal of Physical Chemistry C* **2009,** *113* (19), 8329-8335.

9. Biere, N.; Koch, S.; Stohmann, P.; Walhorn, V.; Gölzhäuser, A.; Anselmetti, D., Resolving the 3D Orientation of Terphenylthiol Molecules on Noble Metals with Kelvin Probe Force Microscopy. *The Journal of Physical Chemistry C* **2019,** *123* (32), 19659-19667.

10. Leung, C.; Kinns, H.; Hoogenboom, B. W.; Howorka, S.; Mesquida, P., Imaging Surface Charges of Individual Biomolecules. *Nano Letters* **2009,** *9* (7), 2769-2773.

11. Nanayakkara, S. U.; Cohen, G.; Jiang, C.-S.; Romero, M. J.; Maturova, K.; Al-Jassim, M.; van de Lagemaat, J.; Rosenwaks, Y.; Luther, J. M., Built-in Potential and Charge Distribution within Single Heterostructured Nanorods Measured by Scanning Kelvin Probe Microscopy. *Nano Letters* **2013,** *13* (3), 1278-1284.

12. Palacios-Lidón, E.; Henry, C. R.; Barth, C., Kelvin Probe Force Microscopy in Surface Chemistry: Reactivity of Pd Nanoparticles on Highly Oriented Pirolytic Graphite. *ACS Catalysis* **2014,** *4* (6), 1838-1844.

13. Moore, A. M.; Weiss, P. S., Functional and Spectroscopic Measurements with Scanning Tunneling Microscopy. *Annual Review of Analytical Chemistry* **2008,** *1* (1), 857-882.

14. Li, G.; Luican, A.; Andrei, E. Y., Scanning Tunneling Spectroscopy of Graphene on Graphite. *Physical Review Letters* **2009,** *102* (17), 176804.

15. Ma, C.; Liao, Q.; Sun, H.; Lei, S.; Zheng, Y.; Yin, R.; Zhao, A.; Li, Q.; Wang, B., Tuning the Doping Types in Graphene Sheets by N Monoelement. *Nano Letters* **2018,** *18* (1), 386-394.

16. Stiévenard, D.; Grandidier, B.; Nys, J. P.; Broise, X. d. l.; Delerue, C.; Lannoo, M., Influence of barrier height on scanning tunneling spectroscopy experimental and theoretical aspects. *Applied Physics Letters* **1998,** *72* (5), 569-571.

17. Sasaki, M.; Yamada, Y.; Ogiwara, Y.; Yagyu, S.; Yamamoto, S., Moir'e contrast in the local tunneling barrier height images of monolayer graphite on Pt(111). *Physical Review B* **2000,** *61* (23), 15653-15656.

18. Chaika, A. N.; Orlova, N. N.; Semenov, V. N.; Postnova, E. Y.; Krasnikov, S. A.; Lazarev, M. G.; Chekmazov, S. V.; Aristov, V. Y.; Glebovsky, V. G.; Bozhko, S. I.; Shvets, I. V., Fabrication of [001]-oriented tungsten tips for high resolution scanning tunneling microscopy. *Scientific Reports* **2014,** *4* (1), 3742.

19. Bhattarai, A.; Krayev, A.; Temiryazev, A.; Evplov, D.; Crampton, K. T.; Hess, W. P.; El-Khoury, P. Z., Tip-Enhanced Raman Scattering from Nanopatterned Graphene and Graphene Oxide. *Nano Letters* **2018,** *18* (6), 4029-4033.

20. Pashaee, F.; Sharifi, F.; Fanchini, G.; Lagugné-Labarthet, F., Tip-enhanced Raman spectroscopy of graphene-like and graphitic platelets on ultraflat gold nanoplates. *Physical Chemistry Chemical Physics* **2015,** *17* (33), 21315-21322.

21. Kozlov, S. M.; Viñes, F.; Görling, A., Bandgap Engineering of Graphene by Physisorbed Adsorbates. *Advanced Materials* **2011,** *23* (22-23), 2638-2643.

22. Chakarova-Käck, S. D.; Schröder, E.; Lundqvist, B. I.; Langreth, D. C., Application of van der Waals Density Functional to an Extended System: Adsorption of Benzene and Naphthalene on Graphite. *Physical Review Letters* **2006,** *96* (14), 146107.

23. Czerw, R.; Foley, B.; Tekleab, D.; Rubio, A.; Ajayan, P. M.; Carroll, D. L., Substrate-interface interactions between carbon nanotubes and the supporting substrate. *Physical Review B* **2002,** *66* (3), 033408.

24. Ulapane, S. B. Harnessing the Control of Metallic Nanostructures on Interfaces Towards Biosensing, Plasmonics and More. Ph.D. Dissertation, University of Kansas, Lawrence, KS, 2019.

25. Lee, D. K.; Kim, S.; Oh, S.; Choi, J.-Y.; Lee, J.-L.; Yu, H. K., Water-Soluble Epitaxial NaCl Thin Film for Fabrication of Flexible Devices. *Scientific Reports* **2017,** *7* (1), 8716.

26. Srinivasan, V. S.; Lamb, W. J., Sheet resistivity measurements of chemically modified electrodes by four-point probe method. *Analytical Chemistry* **1977,** *49* (11), 1639-1640.

27. Ma, R.; Huan, Q.; Wu, L.; Yan, J.; Guo, W.; Zhang, Y.-Y.; Wang, S.; Bao, L.; Liu, Y.; Du, S.; Pantelides, S. T.; Gao, H.-J., Direct Four-Probe Measurement of Grain-Boundary Resistivity and Mobility in Millimeter-Sized Graphene. *Nano Letters* **2017,** *17* (9), 5291-5296.

28. Rao, C. N. R.; Gopalakrishnan, K.; Maitra, U., Comparative Study of Potential Applications of Graphene, MoS2, and Other Two-Dimensional Materials in Energy Devices, Sensors, and Related Areas. *ACS Applied Materials & Interfaces* **2015,** *7* (15), 7809-7832.

29. Alamri, M.; Liu, B.; Sadeghi, S. M.; Ewing, D.; Wilson, A.; Doolin, J. L.; Berrie, C. L.; Wu, J., Graphene/WS2 Nanodisk Van der Waals Heterostructures on Plasmonic Ag Nanoparticle-Embedded Silica Metafilms for High-Performance Photodetectors. *ACS Applied Nano Materials* **2020,** *3* (8), 7858-7868.

30. Singh, E.; Kim, K. S.; Yeom, G. Y.; Nalwa, H. S., Atomically Thin-Layered Molybdenum Disulfide (MoS2) for Bulk-Heterojunction Solar Cells. *ACS Applied Materials & Interfaces* **2017,** *9* (4), 3223-3245.